N71-36593

CASE FILE COPY

NASA CR-72976

V/ETD 54009-F

EXPERIMENTAL VERIFICATION OF THE DESIGN OF AN AXIAL INJECTION CROSSED-FIELD AMPLIFIER

by
H. L. McDowell

Prepared for
NATIONAL AERONAUTICS AND SPACE ADMINISTRATION

Contract NAS 3-11528

Technical Management
NASA Lewis Research Center
Cleveland, Ohio
Special Projects Office
Peter Ramins

Varian/Eastern Tube Division
Salem Road
Beverly, Massachusetts 01915

NOTICE

Requests for copies of this report should be referred to:

National Aeronautics and Space Administration
Scientific and Technical Information Facility
P.O. Box 33
College Park, Maryland 20740

FINAL REPORT

EXPERIMENTAL VERIFICATION OF THE DESIGN OF AN AXIAL INJECTION CROSSED-FIELD AMPLIFIER

by

H. L. McDowell

Prepared for

NATIONAL AERONAUTICS AND SPACE ADMINISTRATION

15 June 1970

Contract NAS 3-11528

Technical Management
NASA Lewis Research Center
Cleveland, Ohio
Special Projects Office
Peter Ramins

Varian/Eastern Tube Division
Salem Road
Beverly, Massachusetts 01915

FOREWORD

The research described herein, which was conducted by Varian/Eastern Tube Division, was performed under NASA Contract NAS-3-11528. The work was done under the management of Peter Ramins, NASA-Lewis Research Center, Cleveland, Ohio.

ABSTRACT

The design of an S-band axial injection crossed-field amplifier capable of 5 kw CW and 20 db of gain is described. The RF dynamic range of the CFA is enhanced by proper design of a reflector electrode at the sides of the interaction space. An experimental vehicle built to verify the design was not successful because of aberrations in the beam optics at the circumferential end of the gun. Design studies show that this is a correctable defect.

TABLE OF CONTENTS

List of Figures

List of Figures
(continued)

List of Figures
(continued)

List of Figures
(continued)

1.0 SUMMARY

This report describes the effort conducted on the third of three NASA supported programs on axial injection crossed-field amplifiers for a satellite-borne transmitter. The objective of these programs has been to design and then experimentally verify the design of a high efficiency amplifier capable of transmitting either AM or FM signals. Originally, this included effort on designs for both the UHF and S-band frequency ranges. For the present program the effort has been on the S-band design. The objectives for this design are 5 kw peak in the AM mode or 5 kw CW in an FM mode with an efficiency of over 50% and a gain of 20db. The objectives are listed in greater detail in Table I.

The first of the three programs was an analytical study conducted for the NASA Lewis Research Center under contract NAS3-11516 (Ref. 1). The designs resulting from this study were for a completely new type of crossed-field amplifier using axial injection of the beam from one side of the interaction space and collection of the beam on the opposite side of the interaction space using a multiple potential collector. Recirculation of the beam from output to input was permitted but the beam was debunched to avoid RF feedback so that the amplifier was non-regenerative. The analytical design appeared to be very promising with predicted efficiencies of about 80%, but there was little experimental data to support it.

This analytical study was followed by an experimental study conducted for NASA Electronics Research Center, Cambridge, under contract NAS12-653 (Ref. 2). The experimental effort on this program was conducted in the VHF frequency range because of the availability of hardware from a Navy sponsored program. Rather than confirm the analytical design, the experimental work showed that there was a basic problem with one of the major assumptions underlying the beam optics portion of the design. The existence of this problem was

TABLE I

LONG TERM OBJECTIVES FOR S-BAND CFA

Frequency	2.0 GHz
Peak Synchronizing Power (TV signal)	5.0 kw
Peak Picture Power	2.3 kw
Average Picture Power	1.75-2.0 kw
Minimum Picture Power	0.9 kw
Sound Power	0.5 kw
FM Saturated Power	5.0 kw
Modulation	AM vestigial side-band or FM
Dynamic Range for AM	20 db min.
Deviation of Small Signal Gain From Linearity, 3 db below saturation	0.5 db max.
S/N ratio over AM bandwidth	42 db min. 55 db obj.
Phase Linearity	
AM -deviation from linear phase vs frequency over band	1.2°
FM- $\frac{\partial^2 \phi}{\partial \omega^2}$	$0.05° /(\text{MHz})^2$ max. $0.015° /(\text{MHz})^2$ obj.
Bandwidth (3db)	
AM	6 MHz
FM	30 MHz
Gain	20 db
Input and Output VSWR	1.05 max. (50ohm)
Efficiency	
AM	>50%
FM	>60%

verified also on two military programs, contract F30602-68-C-0030 for the Rome Air Development Center (Ref. 3) and contract N00024-68-C-1069 for the Navy Electronics Command (Ref. 4). Further insight into this problem was obtained early in the present program. The nature of the problem was a fundamental limit on how low we could make the axial drift velocity of the beam. This limit is imposed by a difference in axial velocity which must exist between bottom and top of the beam in smooth flow. The existence of this limitation was not known prior to the experimental effort. As a consequence of this lower limit in axial velocity we were forced to use an axial velocity higher than that used in our original analytical designs. As a result, individual electrons spent too short a time in the interaction space and the amount of energy exchange with the RF wave was not adequate to yield high efficiency operation, even with the use of ten to fifteen collector elements. High efficiency operation suitable for use in an amplifier operating at saturation was obtained by trapping the beam in the interaction space by a suitable bias applied to the side collector. Experimentally, this yielded 75% efficiency. However, the device could not be operated in the linear regime of the saturation characteristic without generation of substantial broad band noise. In this regard the device had characteristics similar to an emitting sole CFA.

The original plan for the present program called for beam optics and analytical studies to further refine the designs developed under NAS3-11516. Analytical studies were conducted early in the program and they confirmed what we were finding in the experimental work - the basic design was not attractive for other than a saturated amplifier because of the beam optics problem. At this point effort on the program was suspended until May, 1970. During the period of suspension, the basic design of our axial injection CFA's was modified on the military VHF and S-band programs (Ref. 5, 6) and analytical studies of the modified approach were conducted under contract F30602-69-C-0205 for the Rome Air Development Center (Ref. 7). A modified VHF tube was successfully tested on the Navy program in December 1969 and preliminary results on an S-band tube were obtained early in 1970 under contract F30602-69-C-0239 for the Rome Air Development Center (Ref. 6). Based on these results, effort on the present program was resumed, employing the modified axial injection concept. The revised work statement called for construction of a modified version of the RADC S-band tube which would have characteristics more nearly optimized for a satellite application. This tube would be designed and constructed for full average power output with forced liquid cooling but would be tested only at low duty cycles. This approach would insure that all design restrictions imposed by the average power requirement were fully taken into account in the program.

In the period of May-July 1970, during which we were finalizing the design of the tube, we conducted studies to determine why the gain of the military version of the S-band tube was less than predicted by our large signal computer simulations. An understanding of this discrepancy was believed to be important if we were to obtain a valid comparison between the performance of the NASA tube and the large signal computations. These studies led to findings which have turned out to be the most important contribution of this study. These findings showed that the gain was lowered because the electron trajectories were being shifted with respect to the RF wave when they were reflected from the sides of the interaction space. Because trajectories near the top and bottom of the beam undergo a different number of reflections, this "reflection phase shift" causes a debunching of the beam. Once the existence of this phenomenon had been uncovered we realized that it might be possible to use it to improve the linearity of the RF dynamic range characteristic (RF output as a function of RF input). Calculations, as well as experiments, on the RADC tubes had demonstrated that the space charge contributions to the gain (diocotron effect) would give a highly non-linear dynamic range characteristic by substantially increasing the small signal gain over the large signal gain. Our original plans on this program were to linearize the characteristic by using a prebunching collector. This technique is discussed later in this report and was successfully demonstrated on the Navy program. A design for the reflector which would linearize the dynamic range without using a prebunching collector was worked out using computer simulation techniques once we had realized the implications of the reflector phase shift phenomenon. This design was incorporated both into the NASA test vehicle built on this program and into the final tube built on the RADC program. A substantial improvement in linearity of the RADC tube was obtained.

In November of 1970 we first brought the NASA experimental vehicle to test. Measurement of the distribution of current to the delay line and the various collector elements showed very poor beam focusing. The tube was rebuilt with some corrections to the gun element spacings and gun support structure which was thought to be interfering with the beam optics. Computer simulations were used to analyze these corrections. When the rebuilt tube was tested it was found that the problem remained. Further analysis led us to the conclusion that the problem was in aberrations at the circumferential end of the gun on the output side. A design incorporating modifications to this region was then brought to test but it failed because of problems associated with dc arcing in the gun support elements. This problem was subsequently resolved in bell jar tests of the gun structure. The program had been under Varian company support in its final stages including all of the hot tests and rebuilds of the tubes. Since the repairs required by the arcing problem would necessitate all new gun parts and would be relatively expensive, and since we were at this time well beyond the original contract term, it was decided to terminate the effort at this point.

Although the design was not successfully tested, we believe that using the knowledge obtained on this program and using the successful results from the military version of the tube, we can foresee that development of an S-band CFA for AM service at an efficiency in excess of 50% is quite feasible.

2.0 INTRODUCTION

This program was undertaken to validate the analytical design techniques for axial injection crossed-field amplifiers. Originally this was to be done by comparing the results obtained on an experimental vehicle built on contract NAS12-653 and operated in the lower portion of the UHF frequency range with the results of calculations done as part of this program. Subsequently, gun studies were to be conducted to develop gun designs for 800 and 2000 MHz operation. Part way through the program the emphasis was changed to S-band and the beam optics and analytical studies combined in a single test vehicle.

The first task undertaken on this program was to be an evaluation of our large signal computer design techniques through computation of the performance of a UHF experimental vehicle under evaluation on contract NAS12-653. The results obtained on this experimental program indicated that the axial velocity of the beam was higher than we had anticipated. Studies conducted under contract F30602-69-C-0205 for the Rome Air Development Center indicated that there was a fundamental reason why this was so. Using the higher axial velocities, large signal computations of the performance of the tube were conducted and it was found that the efficiencies were significantly reduced as compared with those predicted using a lower axial velocity. The experimental tube showed even lower efficiency because of secondary emission generation problems in the collector region. The result of these studies was the conclusion that a fundamental change in the beam optics design was required. This study took place in the period of May-August of 1969. Section 3.0 of this report is a report on this portion of the program.

Effort on the program was suspended during the period from September 1969 to April 1970. In May 1970 effort was resumed, using a substantially different beam optics system. Section 4.0 of this report is a qualitative description of the new type of amplifier which differs significantly from the original design described in NAS3-11516.

The work statement for the effort was revised at the time the effort was resumed to call for construction of a low duty cycle CFA capable of meeting the goals of Table I. Computer simulations of the design were to be made and the results compared with the experimental results on the tube to validate the design techniques. Based on these results we planned to demonstrate, using analytical techniques, that further improvements in efficiency could be made. The experimental vehicle was to be of a design basically capable of high average power so that we would be sure to take into account limitations imposed by the ultimate average power requirement. This vehicle was to be a modification of one being developed for the Rome Air Development Center under contract F30602-69-C-0239. The major changes planned as compared to the RADC tube were a change in the type of delay line to raise the impedance and, thus, improve the efficiency and a complete redesign of the gun to improve the beam optics and lower the current density. These design studies are discussed in Section 5 of this report.

Section 6 of the report discusses the experimental program and section 7 gives our conclusions concerning the feasibility of this type of device.

3.0 STUDIES OF THE REENTRANT TUBE DESIGN

This portion of the effort was undertaken to provide a more detailed understanding of the tube being tested under contract NAS12-653 and to verify our analytical technqiues by comparing the calculated results with the experimental results. The type of design under evaluation under NAS12-653 was a reentrant design, as sketched in Figures 1-3. Current is injected from one side of the interaction space and allowed to drift axially to collectors on the opposite side. At the same time the electrons circulate circumferentially with a velocity equal to the circuit phase velocity. The circumferential velocity is intended to be several times the axial velocity so that the electrons remain in the interaction space for a substantial length of time. The particular vehicle under evaluation on NAS12-653 operated at 300 MHz and about 1 to 2 kw peak output. For further details on the concept and the experimental vehicle the reader is referred to the final reports on NAS3-11516 and NAS12-653 (Refs. 1, 2).

3.1 Types of Studies Conducted

The computer analyses carried out on the design of the experimental UHF amplifier fall into the following three categories:

A. The axial injection electron trajectory tracing routine was used to examine the magnetron injection gun design and trace the electrons from the gun through the transition region and into the interaction space of the amplifier. The distribution of axial velocities within the electron beam was examined and the degree to which control of these velocities could be obtained by variation in sole potential was determined. The results of these analyses were used to carry out the next portion of the analytical study.

B. The large signal computer program for axial injection crossed-field amplifiers was used to calculate the expected response of the UHF amplifier. The velocity distributions obtained from the

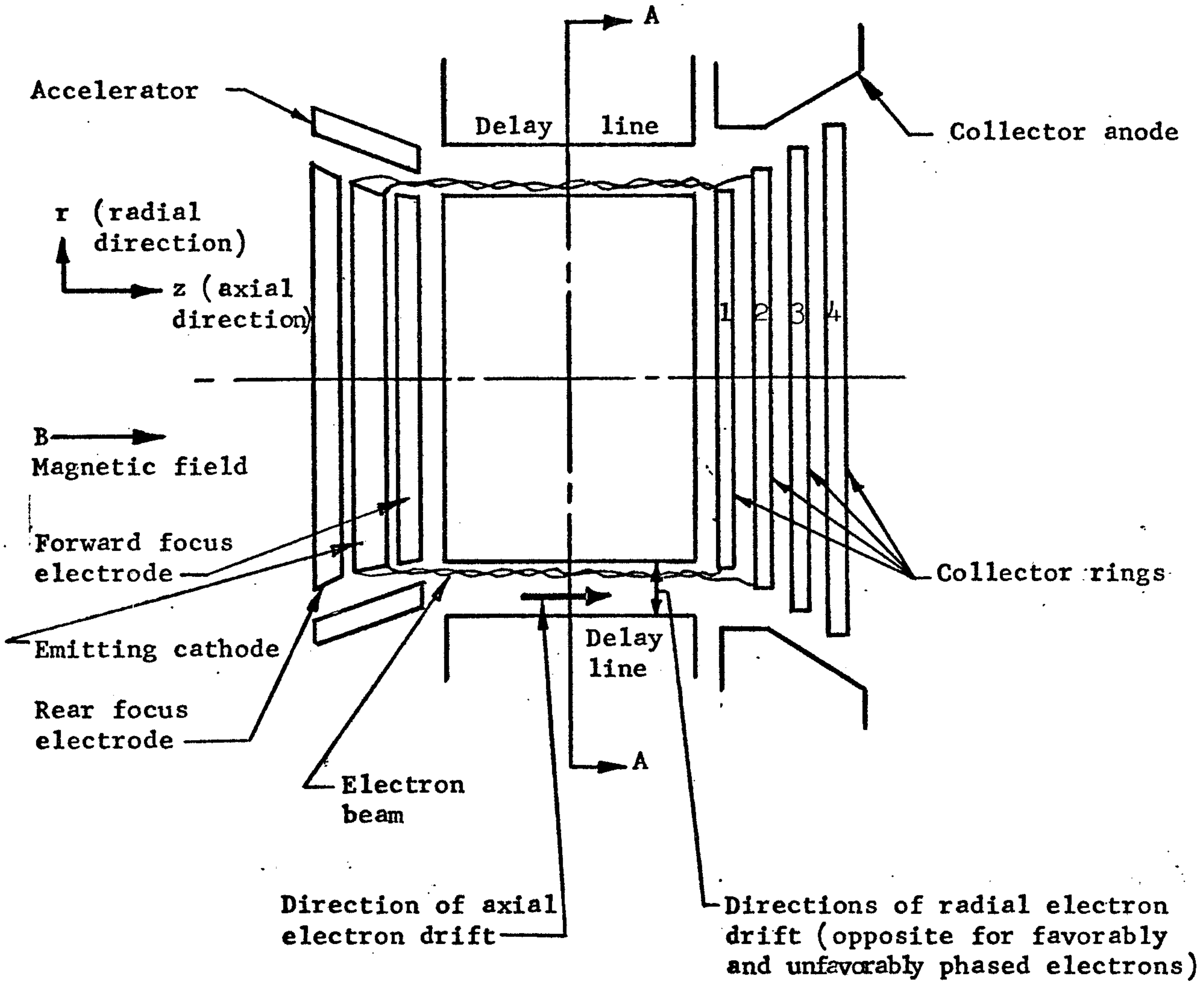

FIGURE 1 SKETCH OF AN AXIAL INJECTION CFA

Electron beam in interaction space circulates in the circumferential direction (perpendicular to paper) with a velocity greater than the axial (z direction) drift velocity. Trajectories are shown for a condition of low RF input drive

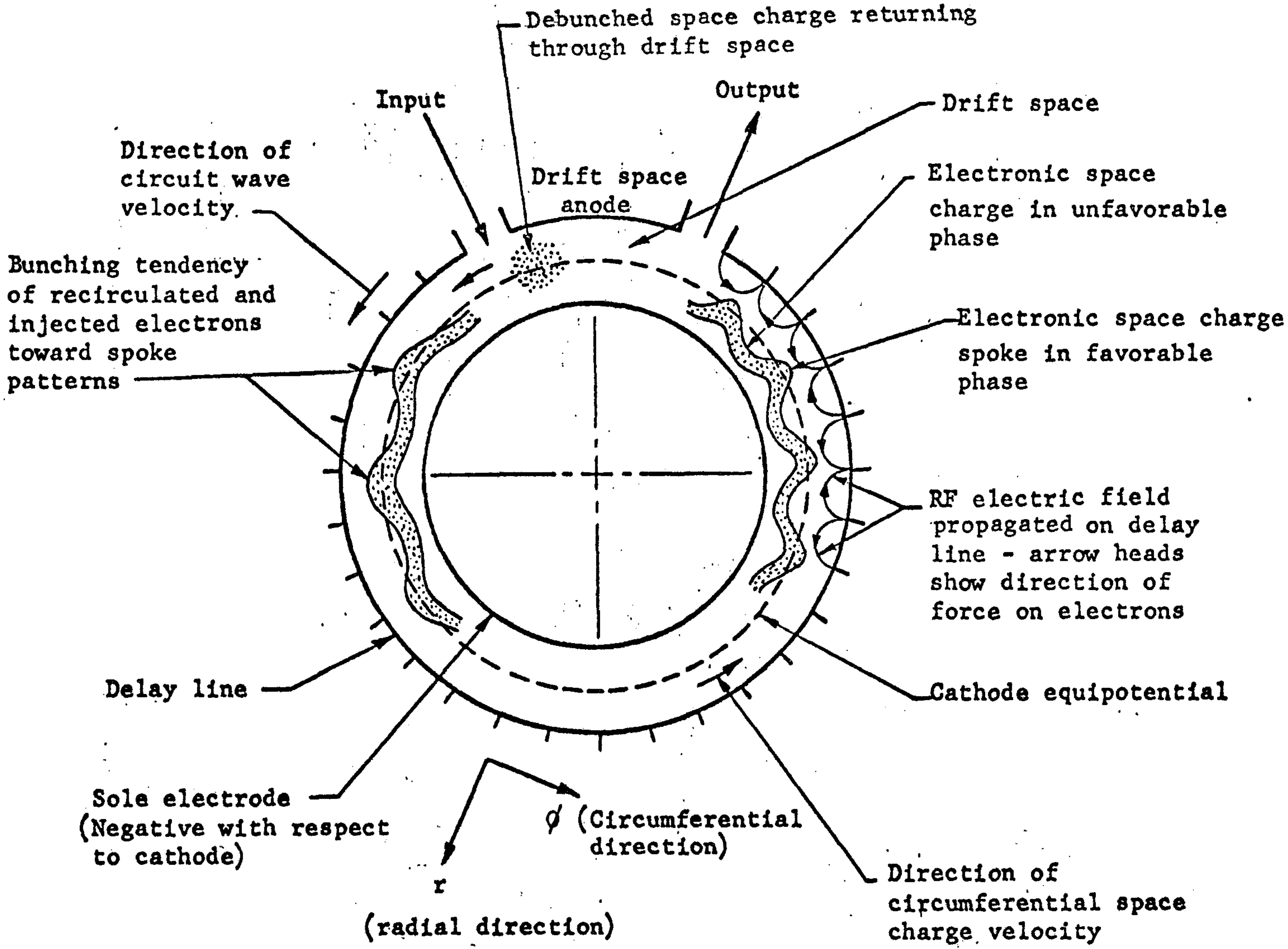

FIGURE 2 CROSS-SECTION THROUGH A-A IN FIGURE 1 SHOWING A SKETCH OF THE SPACE CHARGE DISTRIBUTION

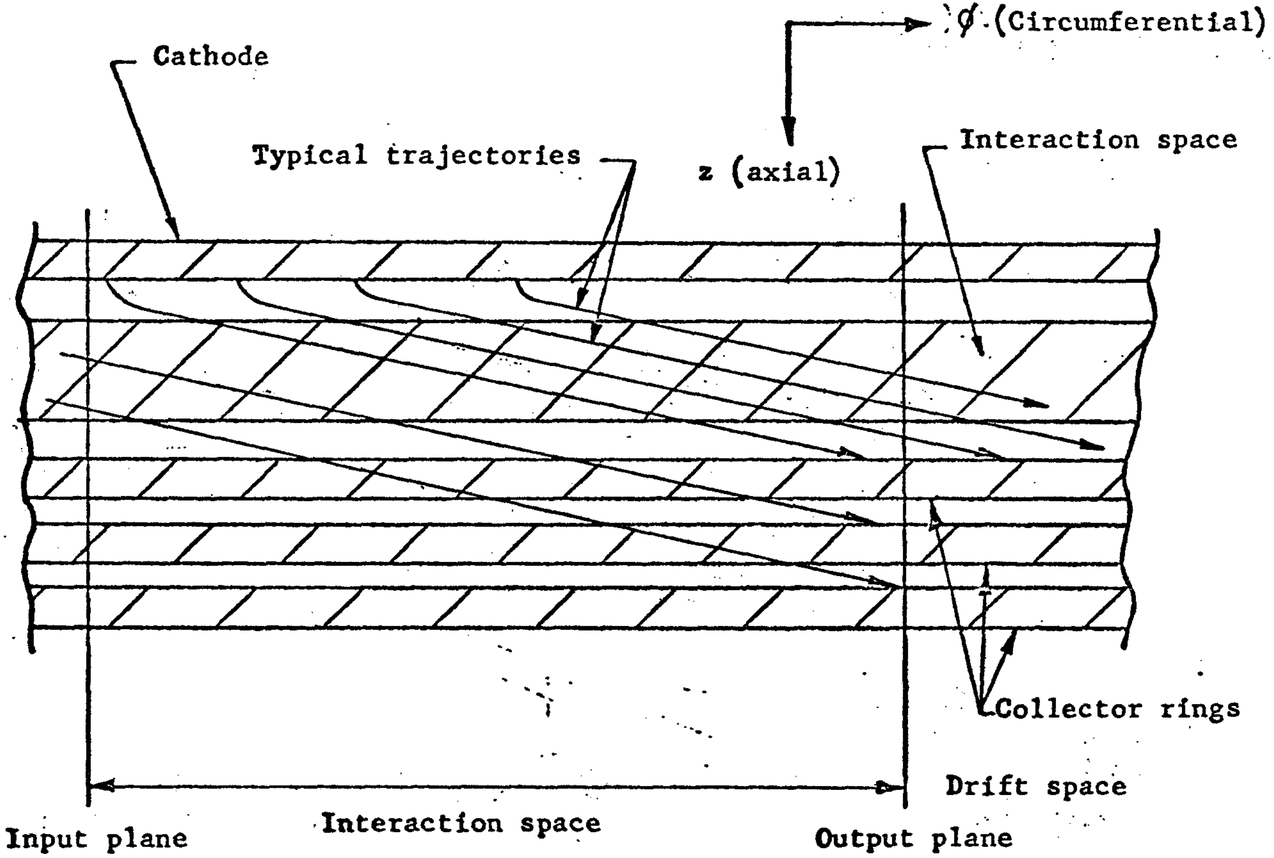

FIGURE 3 SKETCH OF THE INTERACTION SPACE WHICH HAS BEEN DEVELOPED (UNWRAPPED) IN THE ϕ-z PLANE.

We are looking from the delay line toward the sole.

trajectory tracing analysis were used as input conditions for these studies. Values for the transit times of three classes of electrons within the beam were used to carry out large signal calculations. The different transit time values corresponded to different radial positions in the beam. These calculations were carried out first without space charge and then with the addition of space charge forces. Efficiencies were calculated based on the actual current distribution obtained from the computor calculation and the specific collector design used on this tube with the associated collector potentials.

C. The electron trajectory tracing routine was then applied to examine distribution and flow of electrons in the collector region. Trajectories of primary beam electrons and possible secondary emission electrons were both analyzed. These analyses were carried out in an attempt to understand some of the phenomena that had been observed in the collector region performance.

The experimental results obtained from the UHF amplifier were compared with the applicable portions of the analyses that had been carried out.

3.2 Trajectory Analysis in Electron Gun and Interaction Region

The magnetron injection gun and transition region into the interaction space are shown schematically in Figure 4. The electron beam is generated in the magnetron injection gun and enters the interaction space, settling down to a steady state trajectory such that the average circumferential velocity in the "theta" direction is set equal to the phase velocity of the anode circuit. The circumferential velocity is determined by the ratio of electric to magnetic field in the interaction space. Two factors are of direct concern in the launching of this beam. One is to minimize the amount of cycloiding of the beam about its mean radial position. This cycloiding represents a component of kinetic energy, part of which may be lost in dissipation upon collection by the anode delay line or the

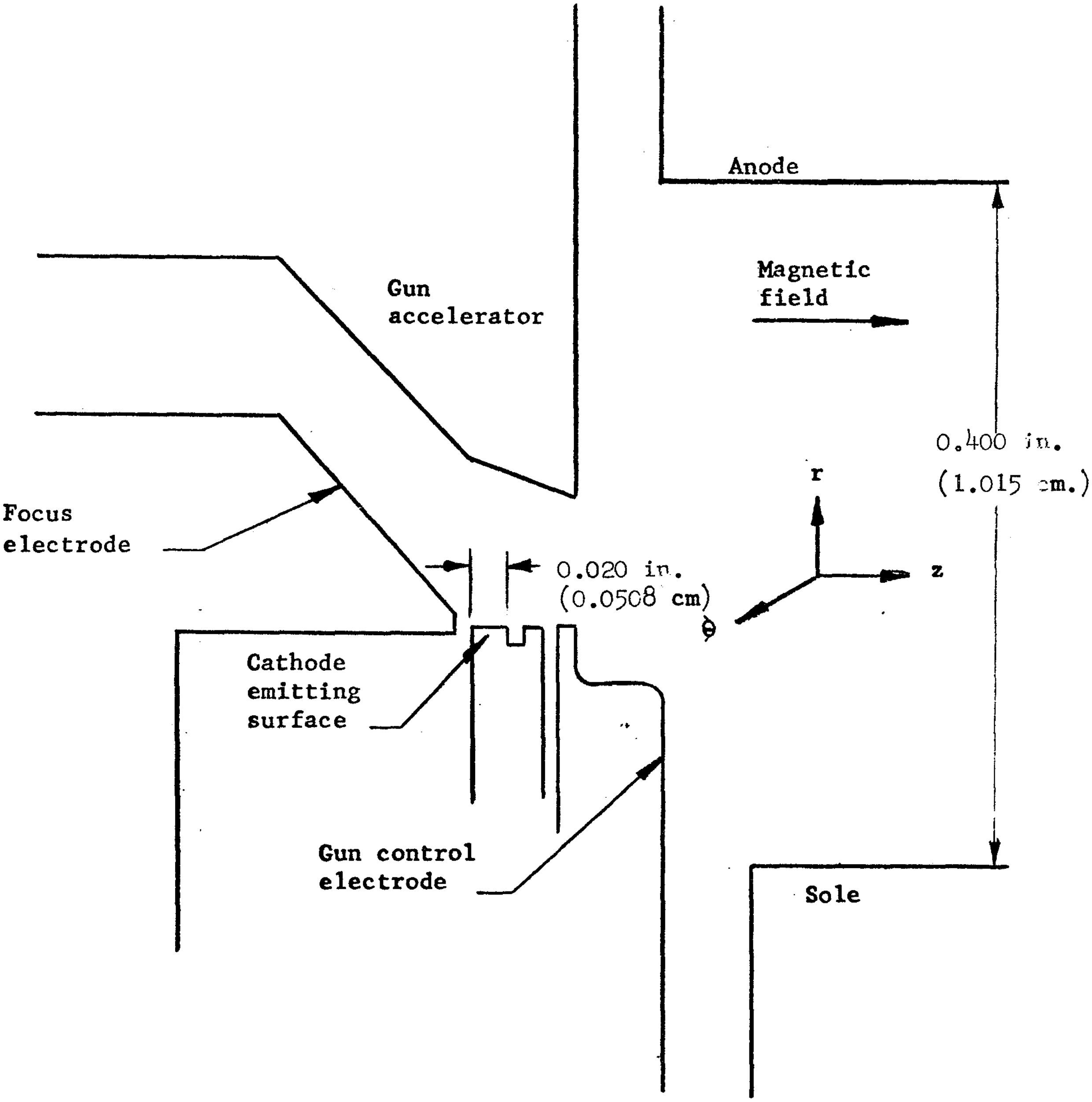

FIGURE 4 MAGNETRON INJECTION GUN AND TRANSITION REGION TO INTERACTION SPACE

collector structure.

The other item of interest is the difference in axial velocity between the outermost edge of the beam and the inner edge of the beam. This velocity differential sets the minimum value at which the outer or upper edge of the beam may travel. When the upper edge velocity is equal to this differential, the lower edge velocity must be zero and the beam is at the point of being stopped and reflected back into the gun region. As will be shown, the differential in axial velocity is set by factors which involve the thickness of the beam, the current, and the magnetic field. However, it is possible to vary the mean value of the beam axial velocity by the adjustment of electrode voltage parameters. In particular, the trajectory tracing program was used to establish the degree of control which the sole bias voltage can exercise over the mean axial velocity of the electron beam. In addition, the degree of cycloiding to be expected under these launching conditions was also evaluated.

The ratio of circumferential velocity to axial velocity of the electron stream determines the ratio of circulating to axial current for a given tube geometry. Thus, this ratio is a prime factor in determining the small signal gain of the amplifier for a given cathode current input. This ratio of velocities also sets the length of circumferential path that is traversed during one axial transit through the tube. The large signal computer program has shown that if the circumferential path traveled by the electrons is excessively short, the efficiency can be significantly affected.

The relationship between circulating and axial current is given by equation 1.

$$I_c/I_a = (h/\pi d)(v_e/v_a) \tag{1}$$

These quantities are defined in Figure 5, which shows that with no reflection of the beam from the end space, the ratio of circulating to axial current is equal to the number of revolutions one electron

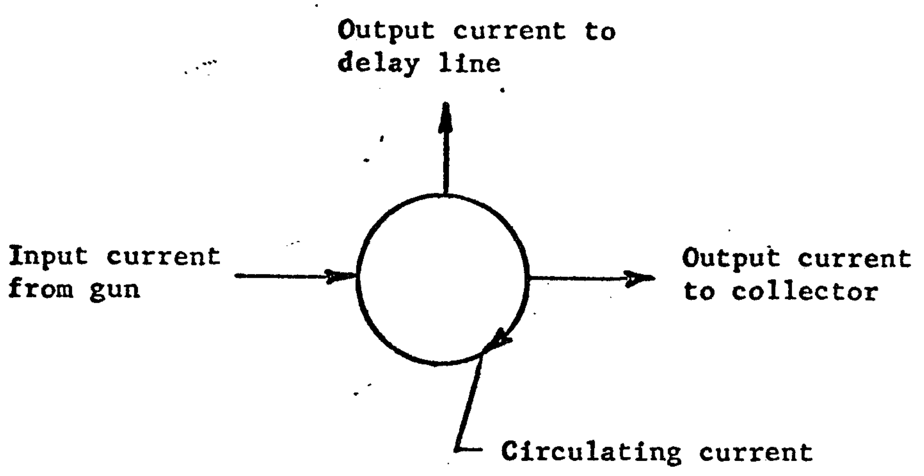

a. A symbolic representation of input, output and circulating currents

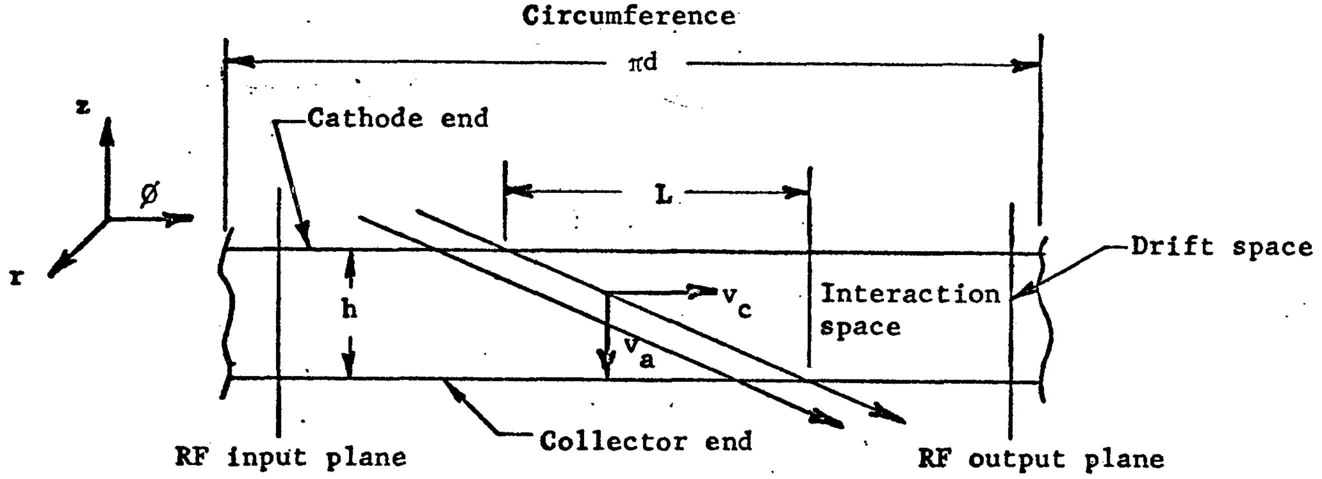

b. Unwrapped view looking down from anode toward unwrapped interaction space

Each electron has circumferential and axial drift velocities, v_c and v_a respectively. Let ρ_o be the space charge density in the beam under low level conditions when the beam is uniform throughout the interaction space and let t be the beam thickness in the radial direction (out of the paper). The circumferential current is then $\rho_o thv_c$ and the axial current is $\rho_o t\pi d v_a$ where D is the beam diameter on injection. The ratio of these currents $I_c/I_a = (h/\pi d)(v_c/v_a)$. However h/v_a is the transit time t for an electron through the interaction space and $v_c t = L$ is the circumferential distance an electron travels while in the interaction space. Thus $I_c/I_a = L/\pi d$ or the ratio of circumferential to axial current is equal to the fraction of the full circumference that a trajectory covers in its traverse across the interaction space.

FIGURE 5 INPUT, OUTPUT, AND CIRCULATING CURRENTS makes during a single axial transit through the tube.

The design of the gun starts by using the Kino analysis (Ref. 8) to establish the conditions in the beam at the exit from the gun region. At this point there is a slip in circumferential velocity between the inner and outer edge of the beam, as well as in axial velocity. These differential quantities are functions of the magnetic field, the cathode tilt angle, the current density and the length of the cathode. In the gun design for the amplifier under discussion here the circumferential velocity at the exit from the gun region is considerably less than the synchronous velocity of 290 electron volts in the interaction region. There is a region of post acceleration in which the radial electric field is increased in going from the gun region to the interaction region. It can be shown that this introduces an additional slip in axial velocity between the inner and outer edge of the beam. The axial velocity slip between the two edges of the electron beam in the interaction space may be computed as the sum of two differentials. The first is that established at the exit plane of the gun by the Kino relations, to which should be added the additional differential slip introduced by the post acceleration in the transition region, i.e.- the increase in radial electric field to the synchronous value for the proper circumferential velocity.

This calculation may be condensed to a more compact and general form, making use of some relations which can be derived for an axial injection beam having Brillouin flow characteristics in the circumferential direction. (For details see section 5.) A result of this analysis shows that the final differential in axial velocity between the two edges of the beam can be given in electron volts as follows:

$$\Delta V_z = E_o t_k \qquad (2)$$

Here, ΔV_z = the differential in axial velocity in electron volts, E_o

is the radial electric field intensity at the center of the beam, and t_k is the vertical rise of the cathode. That is t_k is the cathode length multiplied by the sine of the cathode tilt angle. Thus, it appears that although the absolute value of axial velocities depends on the details of the gun and transition region, the differential in axial velocity across the beam thickness is determined primarily by the end conditions that exist in the interaction region.

In the following discussions, the circumferential velocity corresponds to the synchronous voltage of the delay line, which is 290 electron volts. The magnetic field in these beam analyses is taken to be 900 gauss. If the center of the beam is taken as synchronous with the delay line, this results in a value of electric field in the middle of the beam of 23.1 volts per mil (9.1 kv/cm). Since the cathode length is 0.020" (0.0508 cm) and the cathode tilt angle is 4°, the cathode vertical rise is 1.4 mils (0.00356 cm). This value, multiplied by 23.1 volts per mil (9.1 kv/cm), gives an expected differential betweem the upper and lower edges of the beam of 32.3 electron volts. It will be seen shortly that this is very close to the value achieved by taking the Kino conditions at the output of the gun and following the beam into the interaction region with the trajectory tracing program on the digital computer. In the latter case, a differential of about 40 electron volts was seen to exist and this value was held consistently over a series of runs where the absolute value of the axial velocity of the bottom edge of the beam was varied by a factor of 10 from about 9 electron volts to 93 electron volts.

A series of trajectory tracing runs were made in the area whose geometry is indicated in Figure 4. This shows the magnetron injection gun, the transistion region, and part of the interaction space. These electrodes all possess circular symmetry and the axis of symmetry is below the bottom of the sketch. In the series of electron trajectory runs to be described here, an outer and inner edge electron of the beam were traced from a point two cathode lengths past the emitting surface of the gun. The input conditions for the start of the trajectory are the parameters from the Kino gun analysis. The trajectory tracing routine is a three dimensional analysis and there are three input conditions for each electron, three coordinate positions, and three components of velocity. The circumferential direction is perpendicular to the plane of the sketch of Figure 4. In the discussion that follows, all electrode voltages are given with respect to the cathode, which is taken as zero potential. Velocity components are expressed in equivalent electron-volts of energy. The theoretical considerations which establish a minimum differential in axial velocity between the outer edge and inner egde of the electron beam in the interaction space have been given. Therefore, for a specific gun geometry, interaction space configuration, and set of operating parameters, the optimum adjustment would be to have the axial velocity at the bottom edge of the beam approximately equal to zero electron volts. The axial velocity of the top edge would then be equal to the differential between the velocity at the top and the bottom edges. This is an over-simplification so that a pratical objective in the series of runs to be described was an axial electron velocity for the bottom edge of 10 electron volts. This operating situation was searched out by varying the sole potential in small increments while the other parameters remain fixed. The sole bias was varied in steps of 50 volts by an iterative routine within the program. During all of these runs the following parameters were held constant.

Cathode current	1.8 amps
Cathode current density	0.558 amps/cm^2
Magnetic field	900 gauss (.09 w/m^2)
Cathode tilt angle	4°
Cathode axial length	0.020" (0.0508 cm)

Cathode circumferential length	25"
Trajectory starting point	0.020" (0.0508 cm) past start of the emitting surface.
Circumferential velocity at starting point	
Top	125 electron volts
Bottom	78 electron volts
Axial velocity at starting point	
Top	34 electron volts
Bottom	20 electron volts
Circuit synchronous voltage	289 volts
Anode potential	5800 volts
Approximate sole potential	-3400 volts
Gun accelerator potential	1250 volts
Electron gun focus element potential	zero volts
Sole Anode spacing	0.4" (1.02 cm)
Active circuit length	22.4" (56.8 cm)

A summation of the results of this run is given in Table II. In this table, the label "**FRACLN**" means the circumferential distance traveled by a particular electron during one axial transit while traveling circumferentially at synchronous velocity. (This particular label corresponds to the label used in the large signal computer runs to represent the same quantity.) The quantity **FRACLN** is computed from the specific axial velocity with which each electron enters the interaction space. The values given are steady state values, arrived at after the electrons are settled down to a circumferential velocity corresponding to the synchronous velocity in the interaction space.

It is seen from this table that the conditions searched

TABLE II

SUMMARY OF RESULTS OF ELECTRON-LAUNCH TRAJECTORY COMPUTER RUNS

	Axial Energy		FRACLN						Cycloid Excursion	
	Top Electron	Bottom Electron	Top Electron		Bottom Electron		Average		Top Electron	Bottom Electron
Sole Bias volts	electron volts		ins.	cms.	ins.	cms.	ins.	cms	electron volts	
-4000	Beam reflected back into gun region		0	0	0	0	0	0		
-3700	Beam reflected into gun region		0	0	0	0	0	0		
-3650	Beam reflected into gun region		0	0	0	0	0	0		
-3550	Beam reflected into gun region		0	0	0	0	0	0		
-3450	0.0364	Electron reflected into gun region	175	444.5	0	0	0	0		
-3400	20.4	"	7.4	18.8	0	0	0	0		
-3350	51.5	9.9	4.6	11.7	10.55	26.8	7.56	19.2	±47.2	±61.4
-3300	75.2	34.3	3.8	9.7	5.64	14.3	4.72	12.0	±46.4	±62.0
-3250	104.4	64.6	3.2	8.1	4.08	10.4	3.60	9.14	±48.2	±63.5
-3200	132.6	93.0	2.8	7.2	3.41	8.66	3.13	7.95	±47.6	±64.8

for occurred at a sole bias of -3350 volts, which corresponds to a bottom edge axial velocity of about 10 electron volts with the top edge electron velocity corresponding to 51.5 electron volts. Larger sole biases caused either partial or total reflection of the electron beam. Lower values of sole bias admitted the entire beam but with increasing values of axial velocity. It should be noted that as these values of bias were reduced, the absolute values of axial velocity kept increasing. However, the differential between top and bottom edge electrons stays constant at about 40 electron volts. This is a fairly good correlation with the estimate of about 32 electron volts arrived at by alternate considerations already described. The last column in the table gives the extent of cycloiding that occurs in the interaction space. The excursion from the beam radial position is given in equivalent electron volts. On the average, this value ran about 50 electron volts, which is a reasonably small fraction of the total synchronous voltage of 289 volts.

The electron trajectories for the case of -3350 volts of sole bias are plotted in Figure 6 and illustrate the low cycloid amplitude. The results of these trajectory runs helped to define the values of axial velocity that might realistically be established in the beam. Precise values of electrode potentials will, of course, vary as adjustments to the operating parameters of the tube are made. On this basis the distribution of velocities obtained with a bias of -3350 volts was used to prepare a set of runs with the large signal program involving three classes of electrons--those having the shortest value of FRACLN (4.98), those having the longest value of FRACLN (11.36) and a third class having an average value of 8.14. These values would correspond respectively to an outer edge electron, an inner edge electron and an electron situated midway between these two in the beam thickness.

Thus, this aspect of the analytical program served to

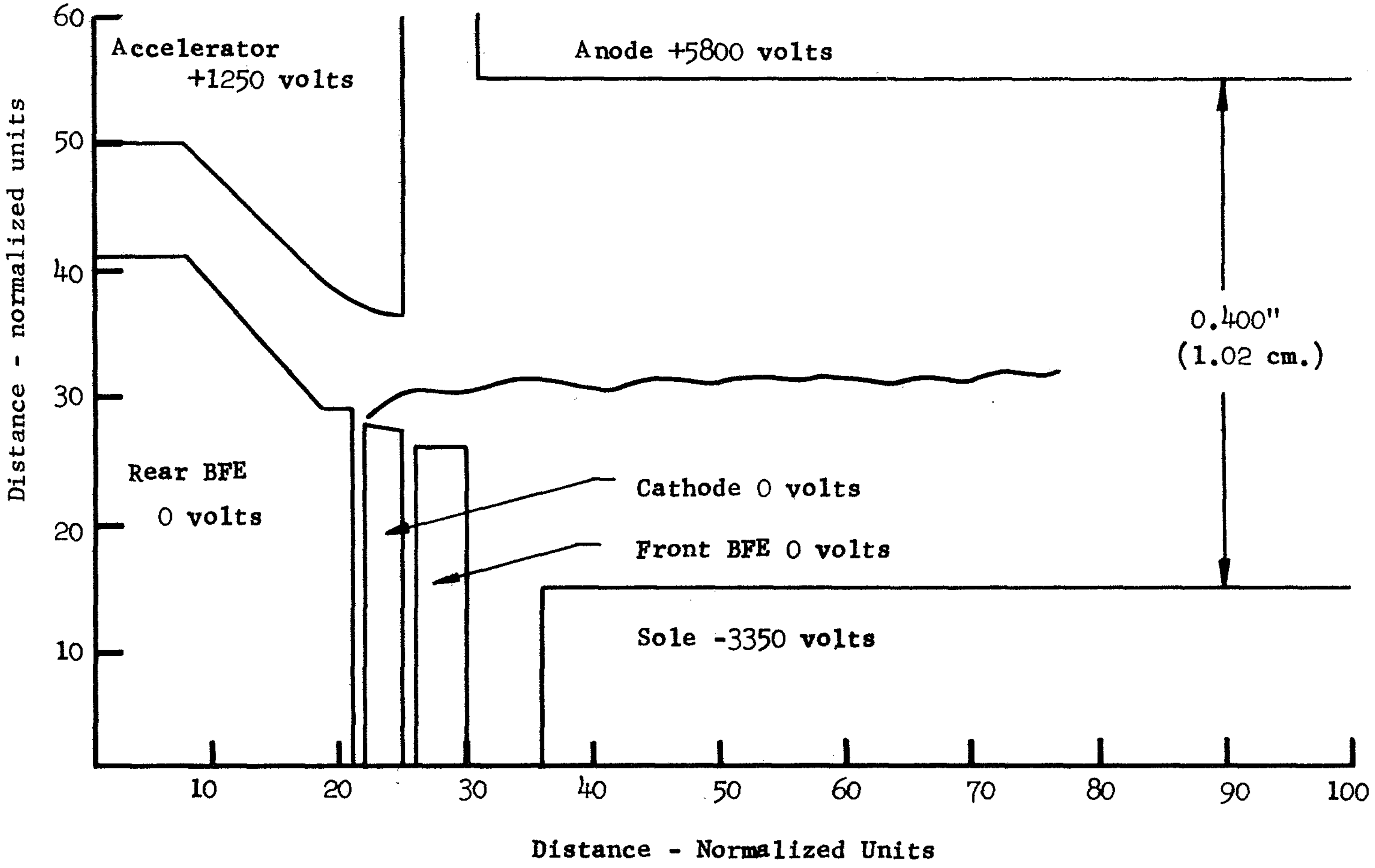

FIGURE 6 ELECTRON TRAJECTORIES IN THE UHF VAXITRON FOR A SOLE BIAS OF -3350 VOLTS.

Distance scales are given in normalized units employed in the computer simulation. One Unit = 0.010 inch (0.0254 cm.).

establish two factors in the design considerations - that the cycloiding in the beam under these launch conditions would be modest and that it represented an energy swing of 17% of the synchronous energy. Since the basic design of the amplifier is aimed at operation with a ratio of anode voltage to synchronous voltage of 20:1, this amount of cycloiding should have little effect on the efficiency of the tube. The range of values obtained for axial velocity distributions shows the degree of control that may be obtained over the effective operating axial velocity. Over the range of values investigated, 50 volts of sole bias adjustment would result in about a 25 to 30 volt change in the axial velocity. Operation with a sole power supply stable to about 1% should make possible operation in a region where the innermost edge of the beam has been slowed down to about 10 volts.

3.3 Large Signal Computer Calculations

In the case of a fully reentrant axial injection crossed-field amplifer, an estimate of the small signal gain may be obtained by taking the circulating current to be the cathode current multiplied by the ratio FRACLN/circuit length. The gain calculation is made via the usual relation:

$$G = -6 - \frac{\alpha}{2} + 55DN \quad \text{db} \tag{3}$$

where α = insertion loss on delay line

D = small signal gain parameter

$$D = \left(\frac{1}{2}\frac{I_c}{V_o}\frac{\omega}{\omega_c}K\right)^{\frac{1}{2}} e^{-\beta y}$$

I_c = circulation current

V_o = synchronous voltage

K = interaction impedance of RF circuit

N = number of RF wavelengths in the delay line

Using this approach, a FRACLN of about 8".(20.4 cm) which is the mean value for the case of -3350 volts of sole bias, yields a small signal gain of about 30 db. The fastest electron with FRACLN of 5" (12.7 cm) predicts a small signal gain of about 22.3 db. Some early large signal calculations carried out for NASA-ERC under Contract NAS12-653 indicated that at a value of FRACLN of 8" (20.4 cm), the simple small signal value still had validity. The results of the large signal computer calculation in that case indicated a saturation gain level of 18.5 db when the tube is driven with 20 watts of RF drive, yielding a power output of 1420 watts and 46.5% efficiency based on the exit potential distribution in the spent beam. The collector elements having the following potentials applied:

Collector Element	Potential (volts)
1	290
2	1390
3	2490
4	3590
5	4690
6	5800

This computer simulation was carried out at a frequency of 300 MHz.

The above large signal run was then repeated with the axial velocities of the electrons increased to correspond to a FRACLN of 5" (12.7 cm) or the velocity to be expected from an outer edge electron. In this instance the simple small signal model fell apart. The gain with 20 watts of drive was reduced to 7.8 db. Only 122 watts of output power was indicated and the efficiency reduced to 7.7%. The efficiencies computed from all future large signal runs are based on this distribution of collector potentials. The run just described did not yet have space charge included in the calculation.

Thus, it became apparent that in order to obtain a reasonable simulation under large signal conditions, runs had to be made with multiple velocity classes simulated in the beam. These runs were carried out under this phase of the analytical program. A series of runs were made containing the three values of FRACLN derived from the trajectory tracing studies-i.e., 4.97" (12.62 cm), 8.14" (20.6 cm), and 11.36" (28.8 cm). These runs were made at a number of RF drive levels, first without space charge, then with the inclusion of space charge, and finally full and partial reflection with space charge was simulated.

The large signal operation of the amplifier with a full circle emitting cathode was investigated with a series of runs carried out under six different sets of operating conditions. Each of the six conditions was for a full circle emitting cathode. Sixty charge rods represent the cathode current. These enter at different distances along the interaction structure and at random values of phase on the RF circuit, as would be the case in actual current injection. Twenty of these charge rods are assigned to each of the velocity classes, resulting in the FRACLNs already stated as 4.97"(12.62 cm), 8.14"(20.6 cm), and 11.36" (28.8 cm) respectively. The simulation is for full reentrancy; however, an examination of the charge rods remaining in the interaction space at the end of the first iteration indicated that most of them would be removed from the system somewhere within the drift tube. Therefore, a second iteration was not necessary since a negligible amount of current would have been recirculated with the values of FRACLN that were chosen. Two values of efficiency were calculated for each of these runs. Based on the distribution of exit potential in the spent beam at the end of the run, efficiency was calculated for the actual six element collector. A discussion of these various runs follows.

3.3.1 Initial Runs Without Space Charge

An initial run with 20 watts of RF drive and no simulation of space charge forces was carried out. The current injection level was 1.8 amperes. A plot of gain and power level on the delay line as a function of wavelengths along the delay line measured from the input end is shown in Figure 7. It is seen that the tube is barely into compression at this drive level and exhibits a conversion efficiency of 47% based on the six element collector. The theoretical efficiency for a collector with a continuous distribution of voltages would be 70.6%. This calculation is based on the exit potential distribution of the spent beam. Examination of the current distribution between anode and sole near the output shows that the current has not interacted strongly with the wave.

The preceding run was repeated at a drive level of 60 watts, resulting in an increase of collector efficiency to 63.1 with 3124 watts of output power. The gain has been compressed 3 db to 17.2 db.

3.3.2 Subsequent Runs Including Space Charge

Having established some reference calculations that did not include space charge forces, the two preceding runs were repeated with full space charge forces at the current injection level of 1.8 amperes. The performance curve for the case of 20 watts of RF drive is given in Figure 9. The gain level achieved is 20.2 db corresponding to 2103 watts of power. The conversion efficiency for the six element collector is 45%. The distribution of current to the various collectors showed that complete saturation was not arrived at with 20 watts of drive. The run including space charge forces was repeated at 60 watts of drive and the results are shown in Figure 10. The saturated gain has been reduced to 17.2 db with 3160 watts of output power. The conversion efficiency with the six element collector is 56.3%.

3.3.3 Calculations on a Reflecting System

An approach which compensates for the limited values of FRACLN which are practically available utilizes reflection of the electron beam at the end spaces back into the interaction space. Under this scheme, collection would take place in the drift space region, resulting in an effectively higher value of circulating

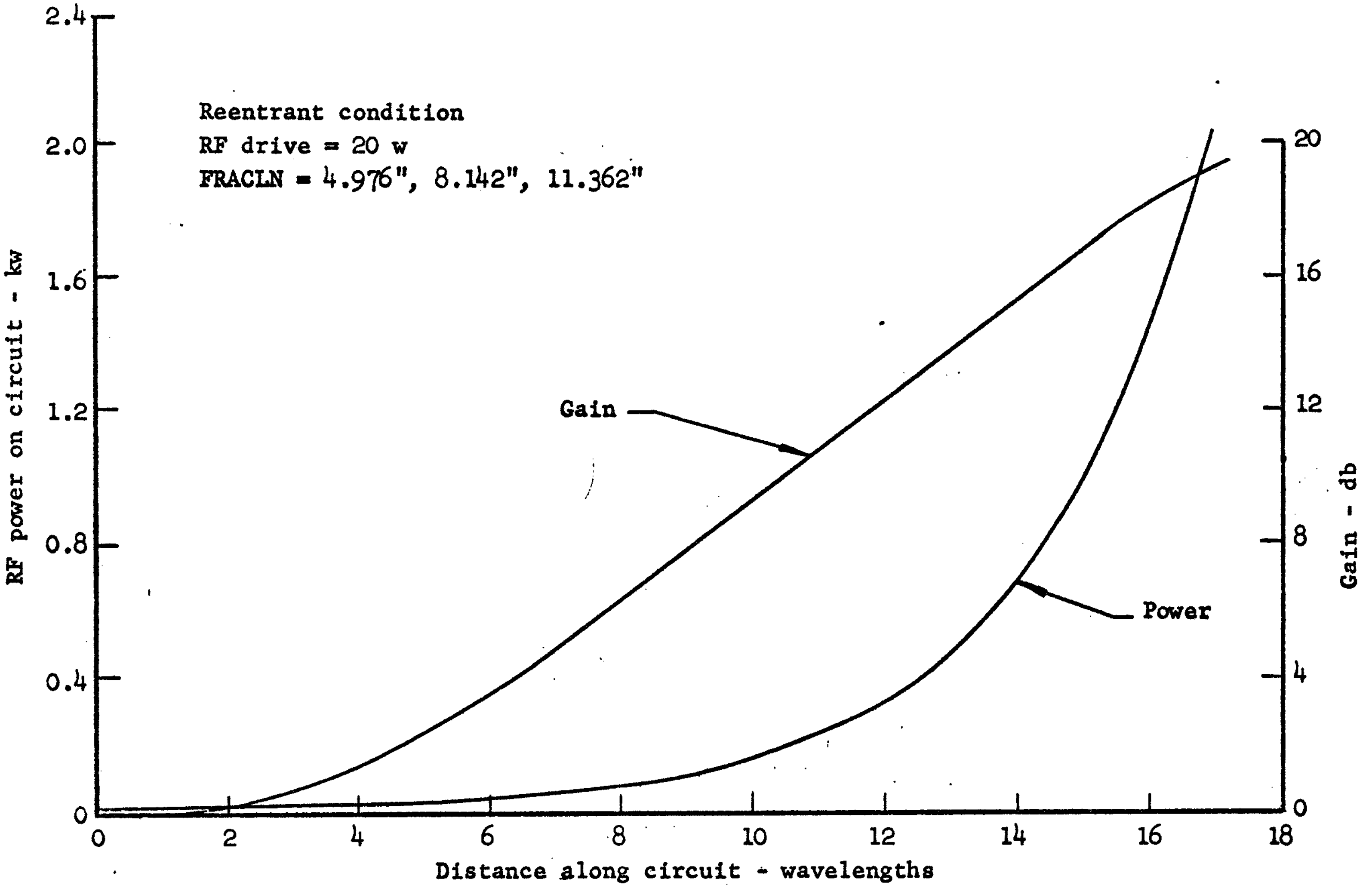

FIGURE 7 COMPUTER RUN FOR EXPERIMENTAL UHF AMPLIFIER AT 20 WATTS DRIVE POWER

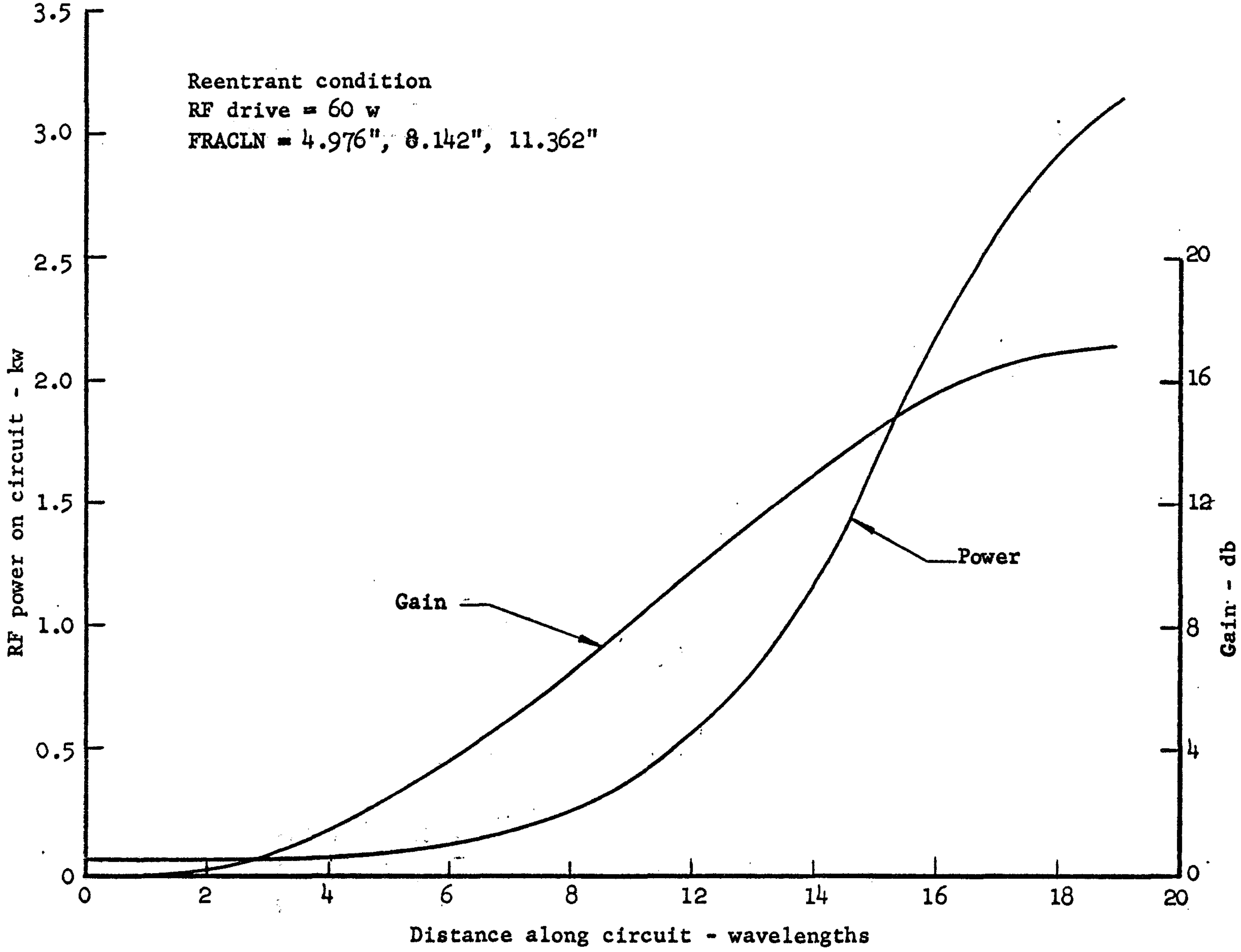

FIGURE 8 COMPUTER RUN FOR EXPERIMENTAL UHF AMPLIFIER AT 60 WATTS DRIVE POWER

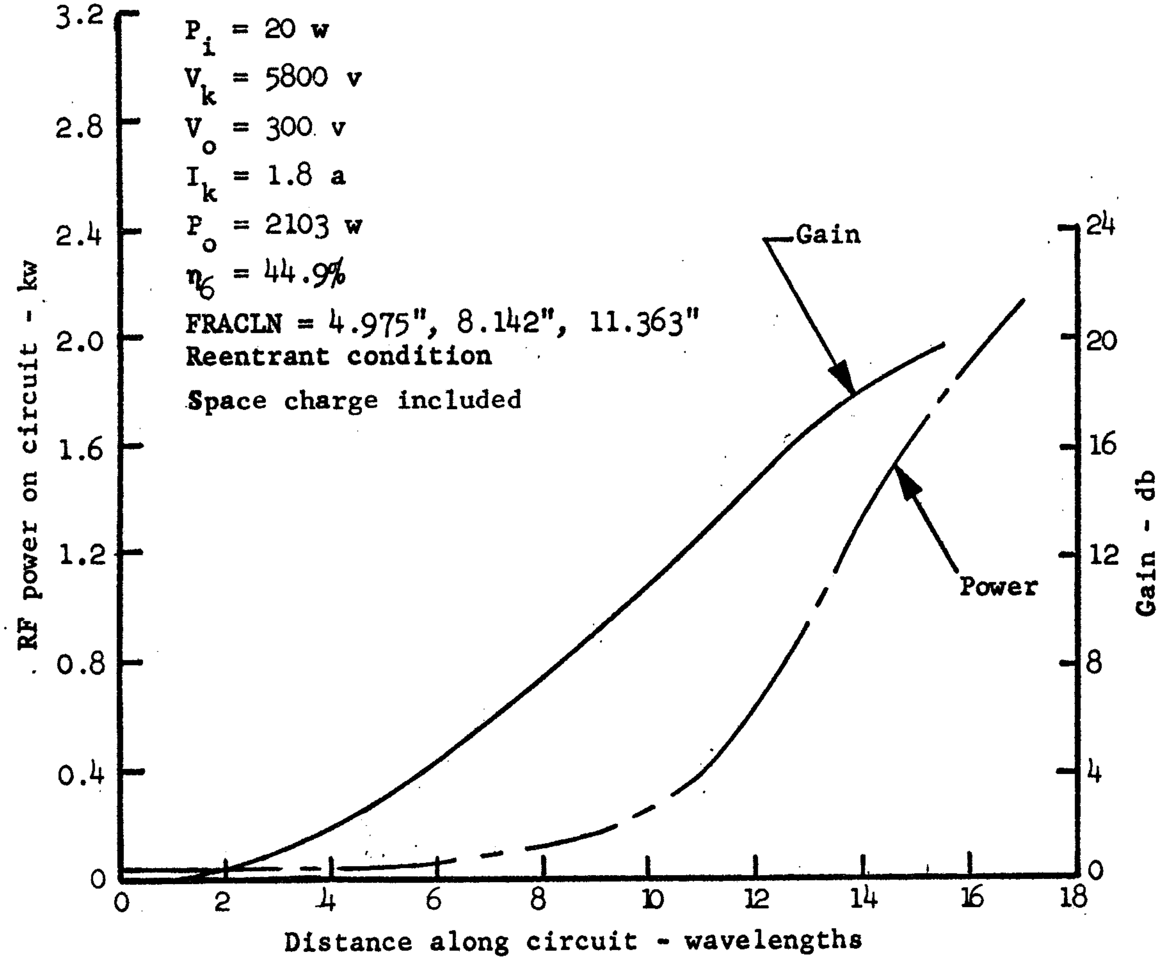

FIGURE 9 COMPUTER SIMULATION RESULTS FOR NON-REFLECTING CONDITIONS AT 20 w DRIVE POWER

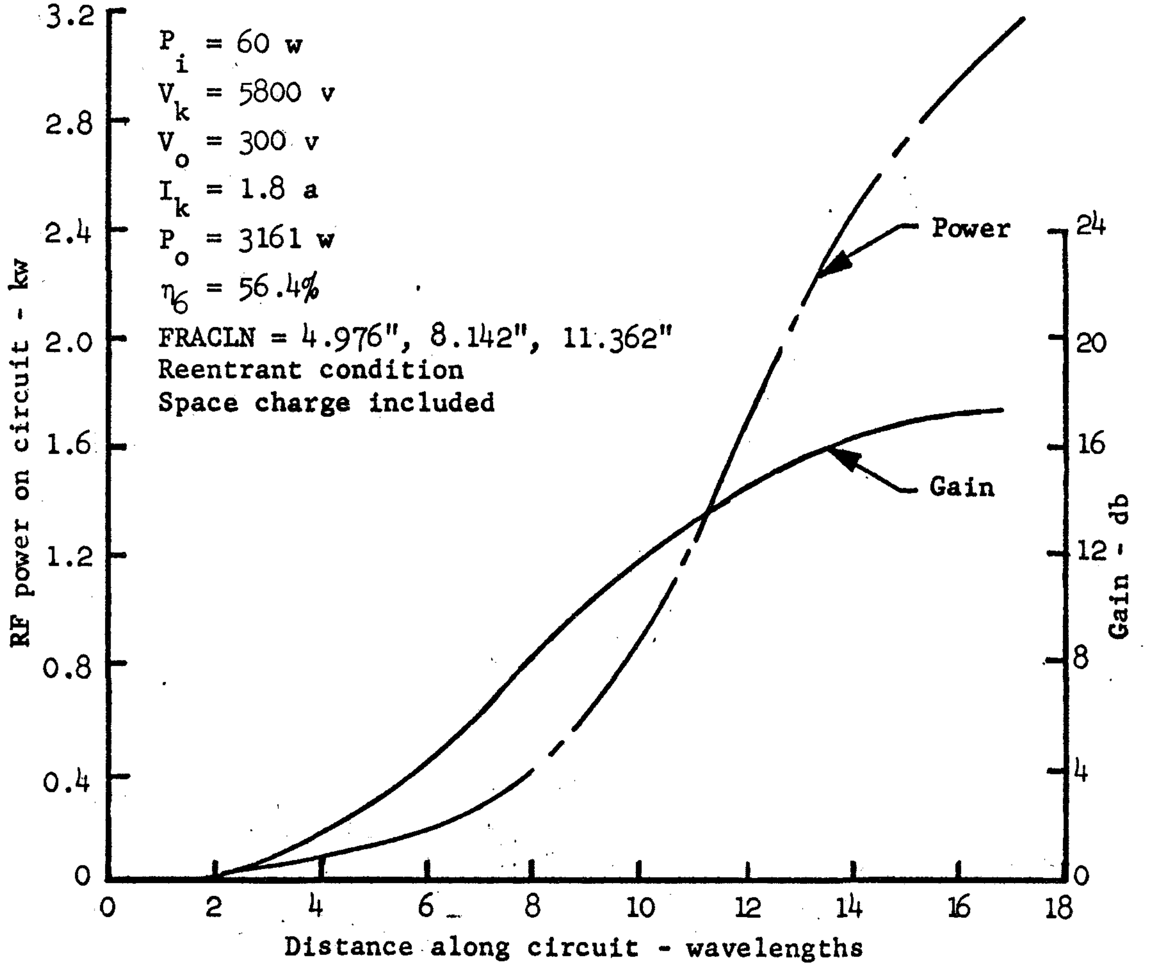

FIGURE 10 COMPUTER SIMULATION RESULTS FOR NON-REFLECTING CONDITIONS AT 60 w DRIVE POWER

current. A run was therefore made simulating total reflection at both the cathode and collector ends of the tube with the current level reduced to 1.0 amps since the effective level of circulating current would be considerably enhanced by the reflection process. The results of this run are shown in Figure 11. A high degree of saturation is achieved with 20 watts of RF drive, the conversion efficiency is 71.5% with a six element collector.

An additional run was made to check the effect of placing the reflection level at cathode potential- i.e., all electrons arriving at the end spaces of the delay line would be reflected if they were above cathode potential and collected if they were below cathode potential. The results of this run are shown in Figure 12. With 20 watts of RF drive, 2436 watts of output is achieved and the efficiency of 68.2% is arrived at with a six element collector. It is seen that there is a very marked increase in efficiency under conditions of full and partial reflection. This is due in large instance to the fact that the number of partially interacted electrons which are collected at lower potentials is greatly reduced so that more of the electron stream is operating at an effectively higher ratio of anode voltage to synchronous voltage. The use of electron reflection from the end spaces eliminates the need for total reentrancy in order to assure maximum efficiency. It makes the elimination of reentrancy desirable to insure that reflecting electrons do not get past the collection point in the drift tube and thus build up a circulating current which could contribute to noise. A practical realization of a scheme for full or partial reflection, therefore, would use a cathode of limited circumferential length placed near the input end of the tube, thus contributing to greater efficiency and resulting in more gain with a lesser length of active circuit.

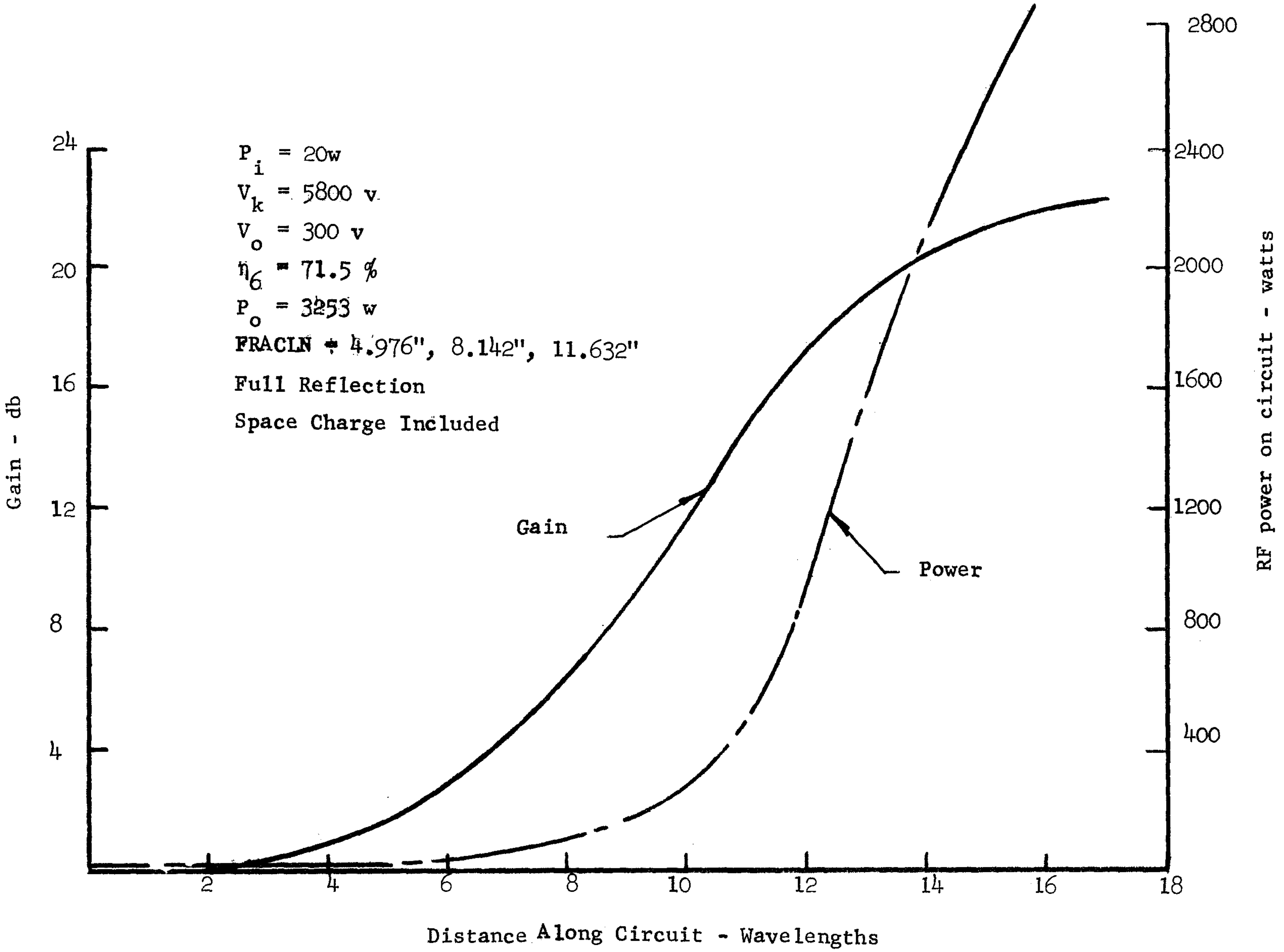

FIGURE 11 COMPUTER SIMULATION RESULTS FOR FULL REFLECTION CONDITIONS.

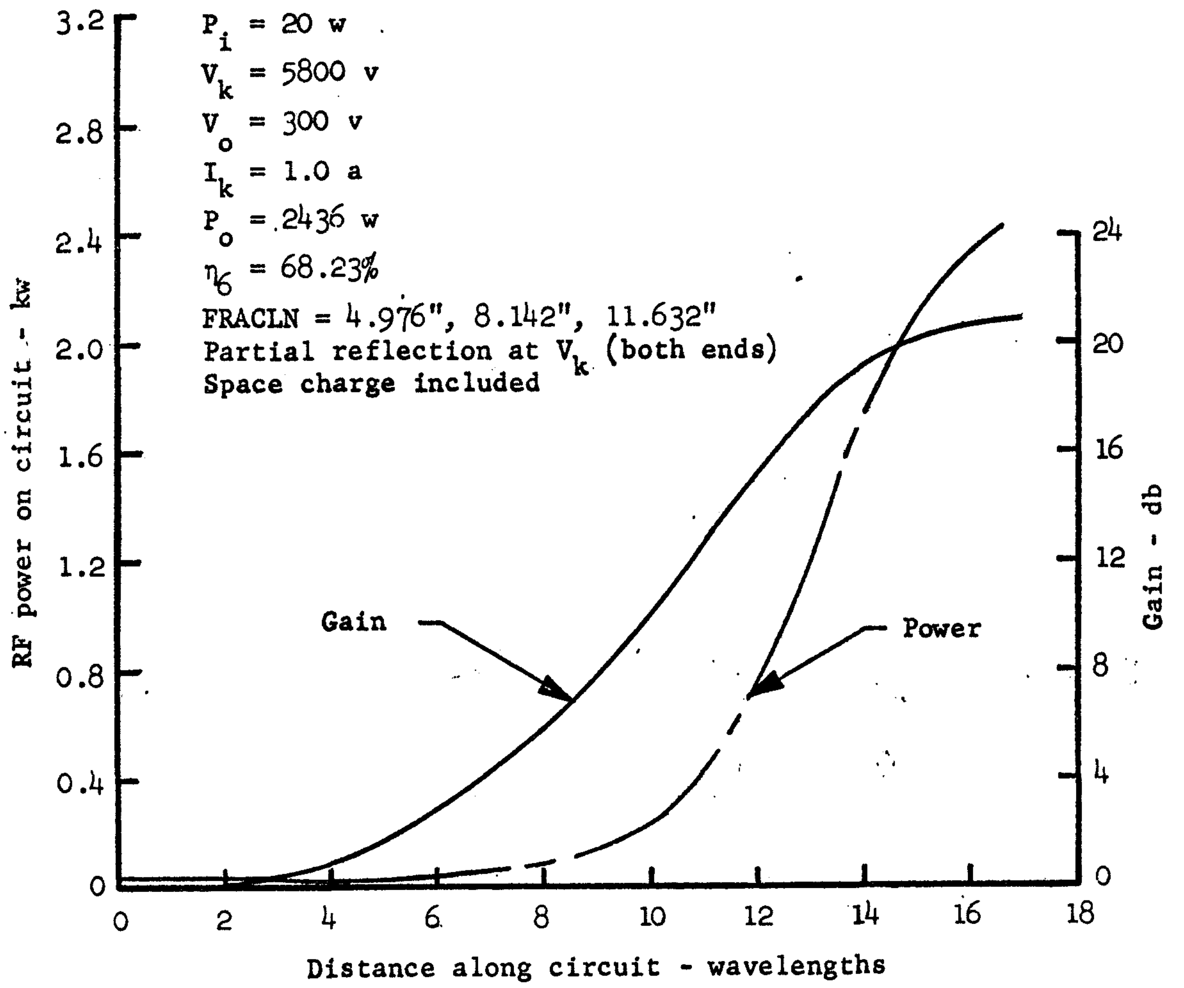

FIGURE 12 COMPUTER SIMULATION RESULTS FOR PARTIAL REFLECTION CONDITIONS AT 20 w DRIVE POWER

3.4 Analysis of Electron Trajectories in Collector Region

As will be brought out in the section discussing test results on the experimental amplifier, the area in which the greatest divergence occurs between the analytical model calculations and the experimental results is in the region of efficiency figures. This is because of the failure of the collector structure to operate effectively. A schematic drawing of the collector region is given in Figure 13. The anode, the sole, and the six collector rings are drawn to scale in this sketch. Also shown is an anode extension ring whose purpose is to extend the anode potential line to the proper geometrical position in the collector region. Two main factors appear to be degrading the measured efficiency of the experimental amplifier. One factor was an excessive amount of current drawn to the anode extension ring under all levels of RF drive. This represents an input of current at full anode potential and results in unused dc power input. In order to investigate any anomalous behavior that might be occurring in the collector region, a series of runs was carried out tracing the paths of the incoming electrons. In each run, seven electrons were injected into the collector region at different radial positions which corresponded to potential positions that would be achieved as a result of varying the drive level. The axial velocity of the electrons was taken to be 50 electron volts in the first series of runs. Later, one run was made with the axial velocity raised to 200 electron volts. The circumferential velocity of the electrons was the synchronous value. The following parameters were kept constant throughout the runs. All voltages are given with respect to cathode potential.

Cathode-Anode Voltage	5800 volts
Sole voltage	-3400 volts
Collector Ring (in order of increasing radius)	
Ring 1	600 volts

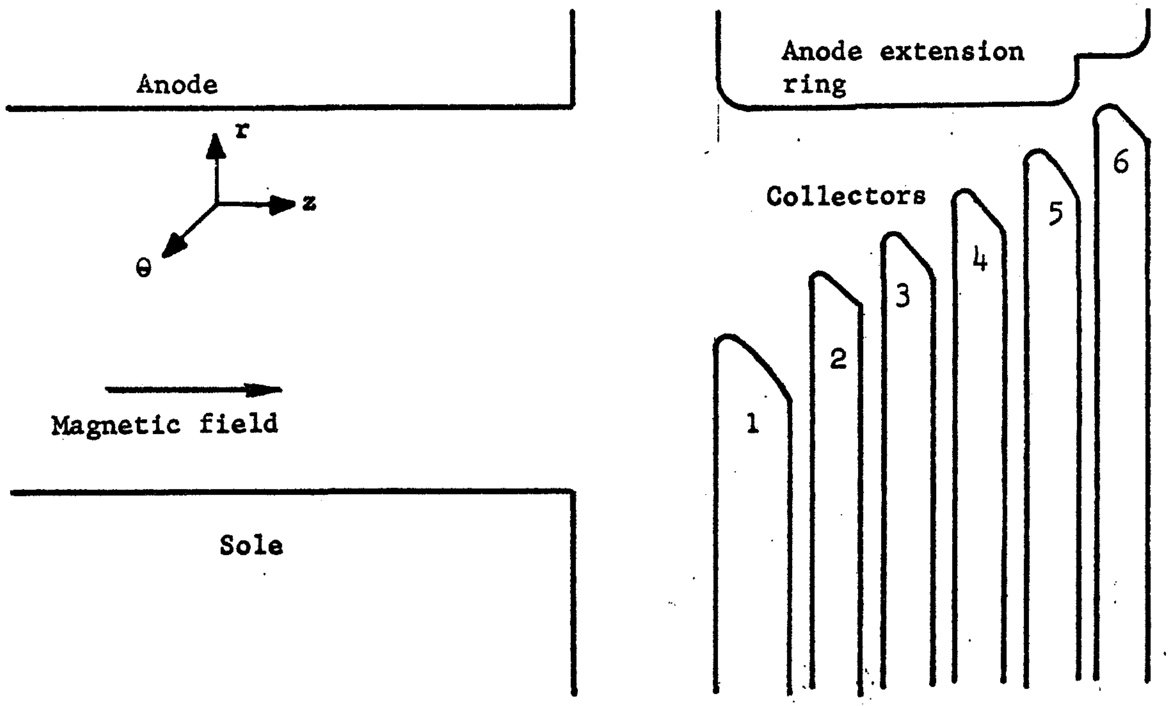

FIGURE 13 SCHEMATIC OF COLLECTOR REGION

Ring 2	1390 volts
Ring 3	2490 volts
Ring 4	3590 volts
Ring 5	4690 volts
Ring 6	5800 volts

To simulate a distribution of electrons due to varying RF drive levels, the electrons were injected at the following potential levels.

Electron 1	-1100 volts
Electron 2	280 volts
Electron 3	1200 volts
Electron 4	2120 volts
Electron 5	3500 volts
Electron 6	4650 volts
Electron 7	5340 volts

The first run was made with the anode extension ring at the anode potential of 5800 volts, its normal operating potential. In this run the seven electrons were assigned axial velocities (towards the collector structure) corresponding to 50 electron volts. This would be typical of the velocity at the outer edge of the electron beam when the bottom edge has been slowed to the equivalent velocity of 10 electron volts.

This first run showed that only Electrons 1, 2, and 3 reached the appropriate collector rings. The four electrons that had been injected at the four highest potential positions were all reflected back into the interaction structure. An examination of the cause for this calculated result showed that there was a perturbation of potential lines into the space between the anode and the anode extension ring and that the extent of this potential perturbation was sufficient to explain the reflection of the higher potential electrons. In the middle of the gap the reduction in potential over that of the anode was on the order of 200 volts. This curving of the potential lines results in a potential gradient directing the electrons back into the interaction space. The spacing between the anode and anode extension ring had originally been chosen so that the anode extension ring would not produce excessive capacitive loading of the bars and the circuit structure. It now appears that this spacing is too great for proper electron optics to prevail and is a possible source of primary electron reflection, for those electrons entering the collector region at the higher potential positions.

In order to assess this effect at higher axial velocities, the preceding run was repeated, assigning to the seven entering electrons an axial velocity corresponding to about 200 electron volts. This was enough forward axial velocity so that only the two electrons at the highest potential (electrons 6 and 7) were reflected into the interaction space. The other five electrons were able to reach the appropriate collector ring.

Thus, having demonstrated that high axial electron velocities are a prerequisite to getting past the potential hill that exists between the anode and the anode extension ring, a series of runs were made to determine whether an adjustment of the anode extension ring potential would help the situation. The axial velocity of the electrons was once again set to 50 electron volts and the potential of the anode extension ring was reduced in successive runs to 5650 volts, 5500 volts, 5350 volts, 5200 volts, and 5500 volts. These five additional runs did not change the basic results. Electrons 4, 5, 6, and 7 were reflected into the interaction space while electrons 1, 2, and 3 were collected as in the initial run. Thus, one possible contributing factor to the electron optics problems in the collector region had been appraised. The addition of secondary electrons and space charge trajectory analysis might form the basis of an explanation for the unexpected distribution of currents in the collector region.

One additional set of runs was carried out to investigate the paths of electrons generated by secondary emission at the collector rings. The secondary emission electrons were simulated by placing a series of seven electrons just in front of the surface of the various collector elements. In the initial simulation each electron was given approximately two electron volts of axial velocity in the direction of the interaction space and two electron volts of axial velocity in the direction of increasing radius, with the initial circumferential velocity being placed at zero. The collector element potentials were as given in the previous section. The electrons were placed approximately 0.01" in front of the various collector rings in all cases except for the first ring near the outer edge. The placement of the electrons was as follows:

Electron No.	Position
1	Near the center of Ring 1
2	outer edge of Ring 1
3	outer edge of Ring 2
4	outer edge of Ring 3
5	outer edge of Ring 4
6	outer edge of Ring 5
7	outer edge of Ring 6

Electrons 1-4 all left the collector region and reentered the interaction space rejoining the main stream. The three electrons (5, 6, and 7) at the highest values of potential behaved differently. Electrons 5 and 6 which were just outside the rings at potentials of 3500 volts and 4650 volts respectively, moved toward the interaction region. They were then turned around and driven into the ring of next higher potential, causing an effective additional dc power input of about 1100 electron volts. The electron at the highest potential of 5800 volts was driven back into the ring from which it would have been emitted. In order to examine the outer range of possible emission velocities, this run was repeated with the axial velocity increased by a factor of 3, bringing the axial velocity directed into the interaction space up to about 18 electron volts. The general pattern of results was the same.

The general trend of these results indicates that the electron that might be emitted from the rings near anode potential are returned to a ring of next higher potential instead of to the ring of emission or to the electron stream in the interaction space. The collection of secondary emission electrons at rings with a higher potential than the point of origin adds an additional increment to the input dc power and thus degrades the effective efficiency of the amplifier. The possibility exists that some correlation may exist between these effects and the distortion of the electric field that was found due to the gap between the anode extension ring and the anode, since this transfer of secondary electrons to higher potential rings is occurring primarily in the region near anode potential where the distortion pattern is strongest.

3.5 Comparison of Experimental Results

Initial testing of the experimental amplifier was carried out at a duty cycle of 0.001 and later increased to 0.01. This was done so that a rapid evaluation of the electronic performance of the tube could be obtained independently of an evaluation of the power handling capabilities of the structure.

The major area in which performance deviated from that predicted by the analytical model was inefficiency. This was due to two main reasons. The first reason was that the amplifier was excessively noisy unless steps were taken to inhibit electron reentrancy through the drift region. In order to inhibit electron reentrancy, the control element that had been inserted into the sole in the drift region was raised to a high positive potential. While this did have the effect of eliminating reentrancy and the undesired background of noise, it also meant the collection of a large amount of current at a potential well above the cathode so that a degradation of efficiency resulted. The other major reason for the poor efficiency performance was the large amount of current drawn to the anode extension ring and the apparent lack of proper switching between the collector elements near anode potential under condition of large signal drive.

To illustrate the efficiency capability of the amplifier at saturation drive, a large negative bias was placed on all the collector rings, including the anode extension ring, so as to drive all the current back into the interaction space with no current being collected on the collector elements. Under these conditions, efficiencies of about 70% were achieved at power output levels of about 1200 and 2400 watts. Under this arrangement of tube elements, spurious outputs appear with the removal of RF drive. However, this mode of operation was set up to evaluate the efficiency capability of the amplifier as a matter apart from the problem of proper operation of the collection structure.

Figure 14 shows an experimental response curve obtained with the various collecting elements set to receive current but with the sole insert tied back to anode potential to completely inhibit reentrancy. The predicted gain of about 20 db has been achieved; however, the efficiency is seen to have been degraded in the manner already discussed. The large signal computer simulation had originally predicted that approximately 2100 watts of power at 45% efficiency would be obtained with 1.8 amperes of cathode current. Experimental results in this case show the predicted level of gain; however, the efficiency and power output for this particular case is half of that predicted. This is believed to be the result of the collector problem discussed in the previous section.

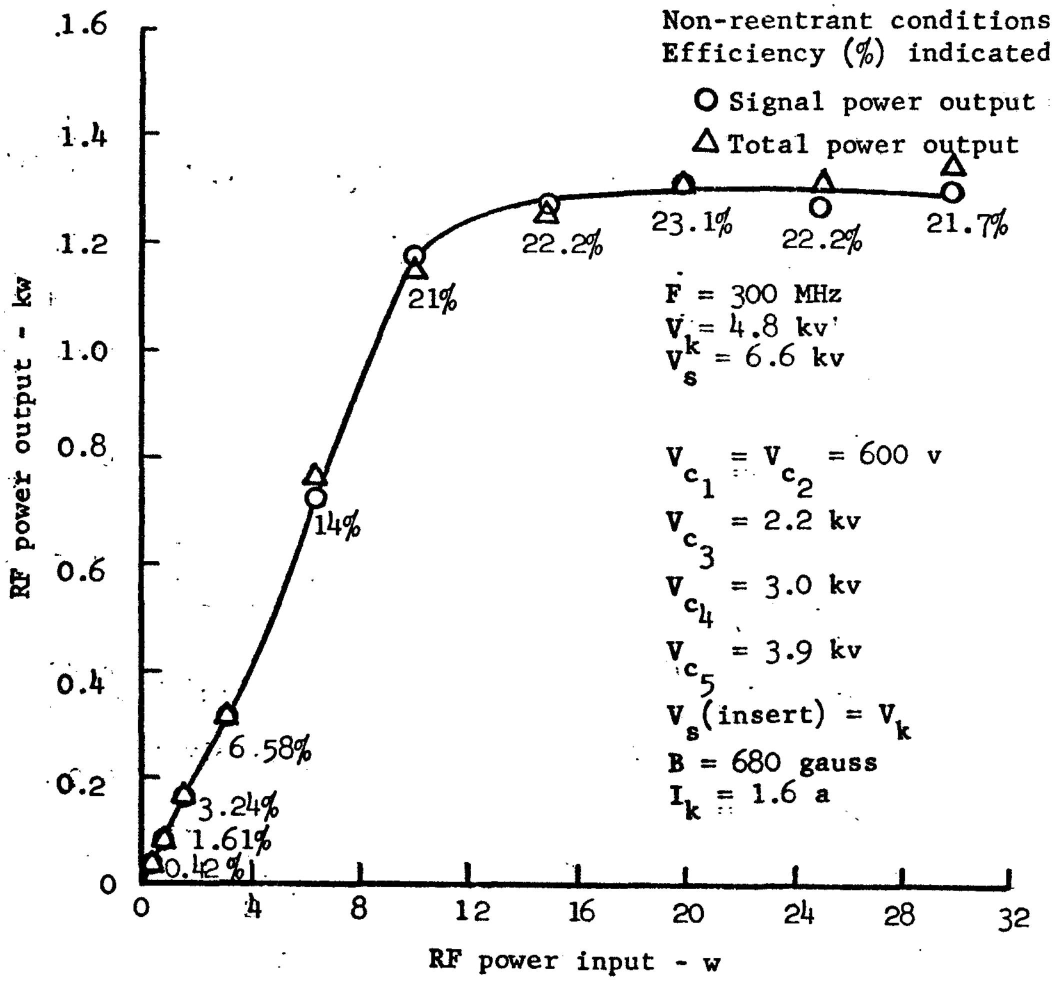

FIGURE 14 RF POWER CHARACTERISTICS FOR EXPERIMENTAL AMPLIFIER UNDER NON-REFLECTING CONDITIONS AT 20 w DRIVE POWER.

4.0 QUALITATIVE DESCRIPTION OF THE NON REENTRANT AXIAL INJECTION CFA

4.1 General Principles

The problems with the beam optics discussed in the previous section have led to a revision in the axial injection tube geometry. Figures 15 through 17 are sketches illustrating the revised principles of operation. Figure 15 shows a view looking into the interaction space from one side. A delay line (slow wave circuit) is mounted on the anode side of the interaction space and a smooth sole electrode is mounted on the negative side opposite the anode. This sole electrode is biased negatively with respect to the cathode. A magnetic field is directed perpendicular to the plane of the paper. The voltage applied between the sole and anode establishes an electric field perpendicular to the magnetic field. In this crossed-field geometry, electrons flow from left to right with a velocity equal to the ratio of the dc electric to the magnetic field. If the gun is designed to properly inject the electrons into the interaction space, the trajectories will be smooth. Any deviation from optimum injection conditions will produce rippling or cycloiding of the trajectories. Minimization of this cycloiding is necessary to optimize the efficiency of the amplifier. Figure 15 shows the beam under zero or very low RF input drive to the amplifier. The beam is injected into the interaction space from one side along about the first quarter of the length of the delay line. After interaction with the RF wave on the delay line, the beam is collected on a collector having one or more elements. The various branches of this collector serve to sort out the different potential energy classes in the spent beam so that electrons are collected at a voltage near their exit potential from the interaction space.

The beam injection system may be seen more clearly in Figures 16 and 17. Figure 16 shows a view looking from the delay

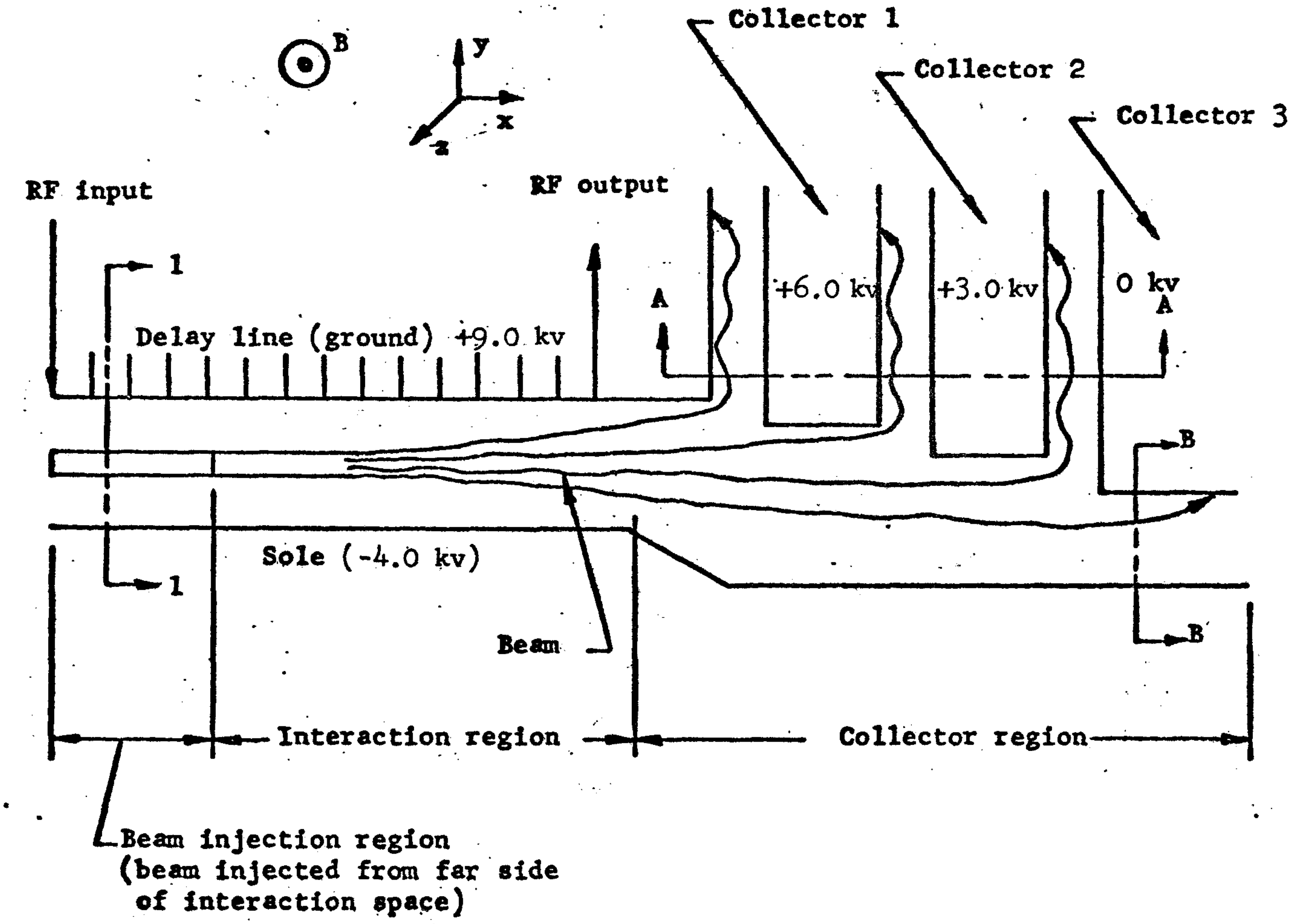

FIGURE 15 SIDE VIEW SCHEMATIC OF VAXITRON AMPLIFIER

Voltages are given with respect to cathode although the delay line is grounded. Electrons are made to collect on collector surfaces by reduction of the magnetic field above plane A-A and to the right of plane B-B. Sketch corresponds to relatively low RF drive. At higher drive powers a considerable portion of the beam will be collected on the delay line. Three collectors are shown, but in practice the number can vary from one to over ten.

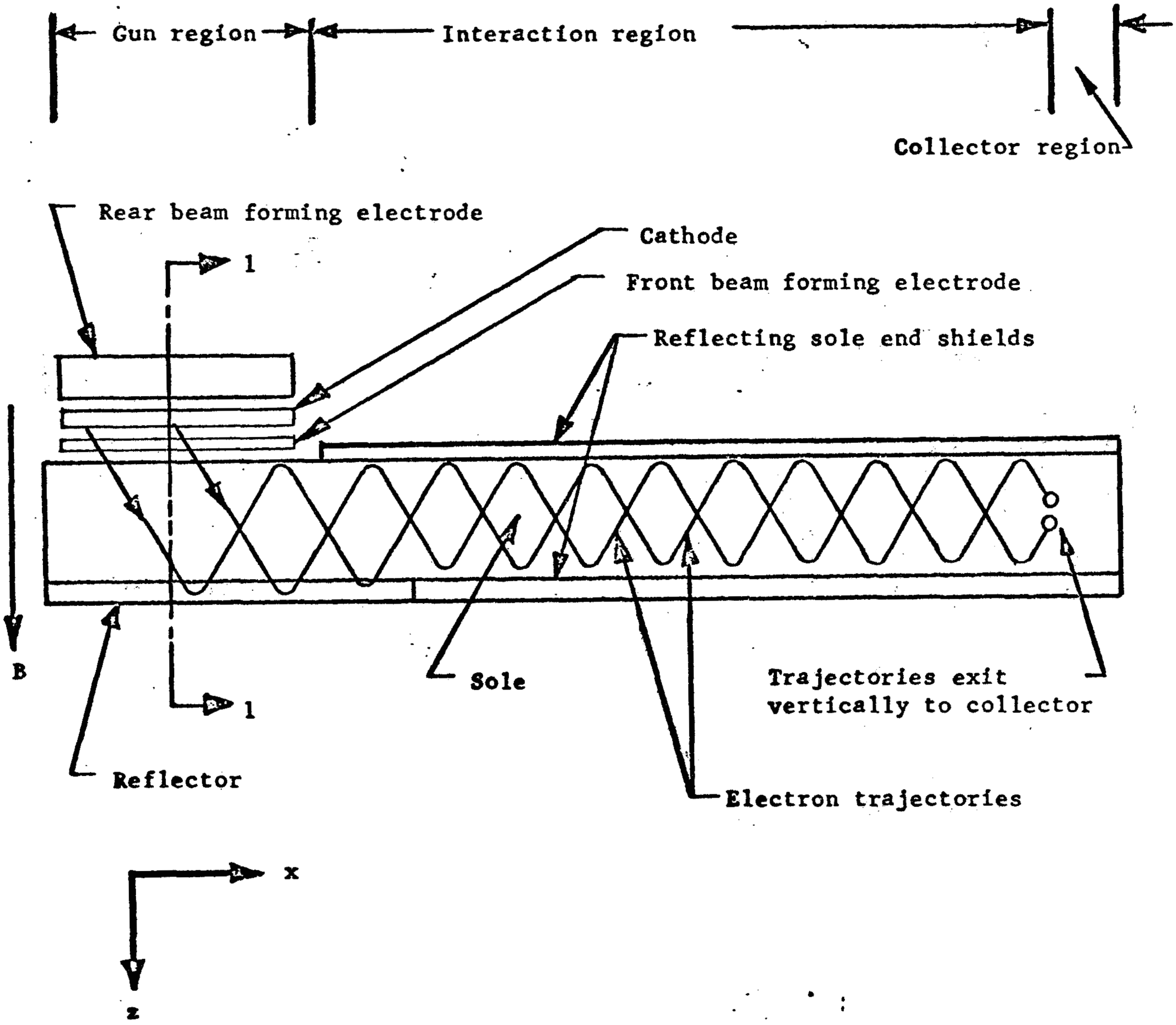

FIGURE 16 SCHEMATIC VIEW LOOKING FROM ANODE TOWARD SOLE SHOWING REFLECTION OF ELECTRONS FROM SIDE SHIELD

Drawing is not to scale and in actual tube, velocity in x direction exceeds that in z direction by several times

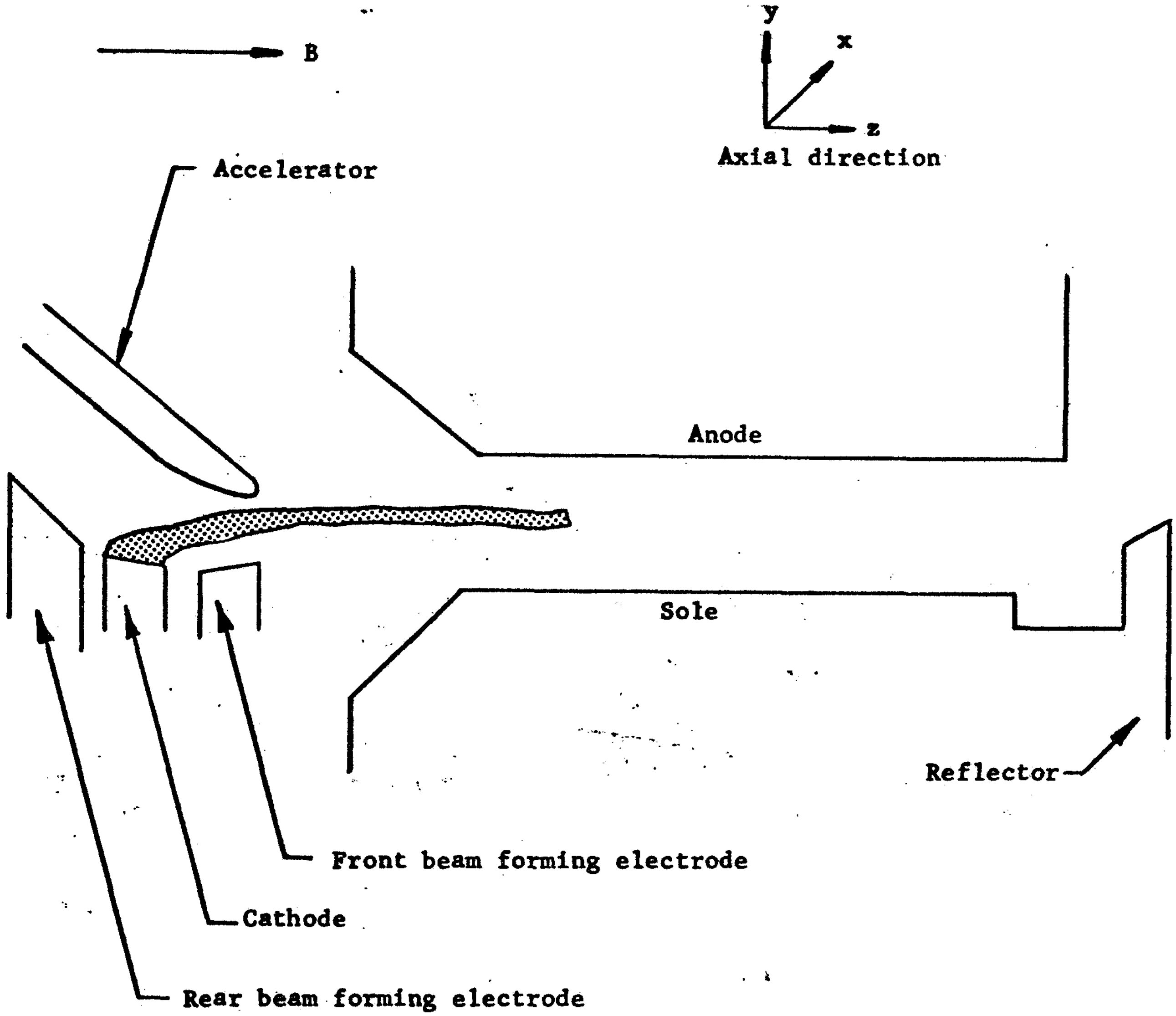

FIGURE 17 SCHEMATIC VIEW OF CROSS SECTION THROUGH 1-1 IN FIGURES 2 AND 3

Beam flows into paper in x direction at a velocity several times higher than axial drift in z direction line toward the sole. This view is highly schematic and does not show details of the gun structure. As may be seen, the beam is injected at a slanting angle across the interaction space and is reflected several times from end shields at the side of the interaction space in the process of traveling from the gun to the collector region. The velocity in the direction down the tube (x direction in Figure 15 and 16) is made substantially larger than the velocity in the axial direction so that there is only a small amount of energy associated with the axial drift velocity. The component of velocity down the tube toward the collector is made synchronous with the wave on the delay line to obtain the desired traveling wave interaction. Figure 17 shows a cross-sectional sketch through plane 1-1 in Figures 15 and 16. This is a view looking down the interaction space in the direction of electron flow toward the collector. This sketch shows the gun electrodes in more detail. As may be seen, the gun is similar to the magnetron injection guns which have been used in some TWTs and klystrons.

Opposite the gun in Figure 17 we show the reflector electrode. This electrode is also shown in Figure 15 and extends alongside the interaction space on both sides. The reflector is really a specially designed form of end hat which is used to improve RF linearity. We will return to a description of its operation in a later section.

4.2 RF Interaction in Crossed-Field Amplifiers

The nature of the interaction taking place in the crossed-field amplifier may be understood better by reference to Figure 18 which shows the beam and the electric fields of the RF wave in a moving frame of reference. For a maximum gain in a crossed-field amplifier the beam is made to travel with its average velocity (equal to E/B) synchronous with the circuit wave velocity. At synchronism the dc electric field forces pulling an electron toward the anode are just balanced by the magnetic field forces pushing it toward the sole.

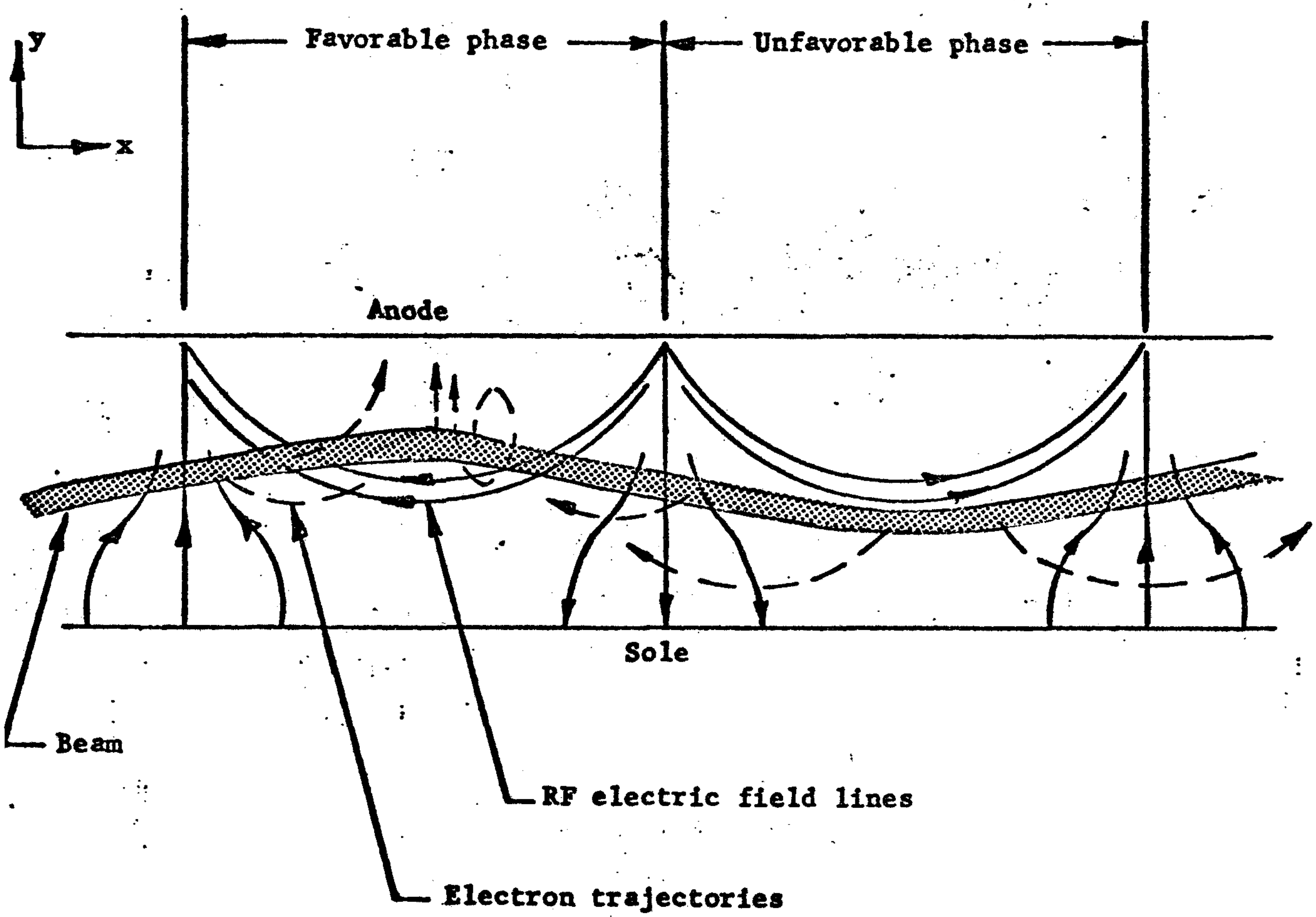

FIGURE 18 SKETCH OF RF INTERACTION IN MOVING FRAME OF REFERENCE

Arrows on RF electric fields are in direction of force on an electron. Sketch shows beam deflected as it would be at a power level 6 db to 10 db below saturation. Dashed lines show paths which will subsequently be taken by electrons. The y components of the RF field are responsible for phase focusing of the beam.

The introduction of the RF fields of the circuit wave upsets this balance. Those electrons in the favorable phase are decelerated by the RF wave. In the process the kinetic energy lost is given up to the RF circuit wave, resulting in amplification of this wave. The mechanism of energy exchange is through the RF currents induced on the delay line by the motion of the electrons. These currents are so phased as to add to the currents already flowing on the line, resulting in enhancement of the circuit wave. As the electrons slow down as a result of the RF interaction, the magnetic field force toward the sole is reduced and the electrons are pulled toward the anode by the dc electric field. In the process the electrons regain kinetic energy from the dc electric field. Electrons in the favorable phase thus undergo a motion by which they continuously give up energy to the circuit wave and regain it from the dc field. In the process they move from the original beam position toward the delay line. Electrons in the unfavorable phase undergo the same process, but with directions reversed so that they extract energy from the circuit wave and move away from the original beam position toward the sole. In the regions between the favorable phase and unfavorable phase, the components of the RF field are such as to produce a focusing of electrons toward the favorable phase. This phase focusing, together with the fact that electrons in the favorable phase move into regions of higher RF field strength while those in the unfavorable phase move into regions of lower RF field strength, results in the net gain of the amplifier. Throughout this process the electrons maintain their synchronism with the circuit wave and thus their average kinetic energy. The energy interchange in the crossed-field amplifier may thus be said to be a result of the motiom of electrons across the dc field from the original beam position toward the anode and the sole. The kinetic energy of the electrons remains approximately constant and this kinetic energy is dissipated on the delay line or collector elements when the electrons are collected. The conversion efficiency of the crossed-field amplifier can be made high by making the ratio of the potential difference between the original beam position and the anode large as compared to the kinetic energy of the beam. If we neglect RF attenuation on the line, we can then calculate a theoretical maximum efficiency. If voltages are measured relative to the cathode taken at zero potential, V_o is the beam synchronous voltage and V_a is the anode voltage, the theoretical efficiency is given by:

$$\text{efficiency} = 100\% \left(1 - \frac{V_o}{V_a}\right) \qquad (4)$$

To maximize this efficiency the ratio of V_a to V_o should be made large. In the present S-band amplifier, this ratio will be in the vicinity of 10 giving a theoretical maximum efficiency of 90%. In practice, of course, the efficiency is reduced because of RF losses on the circuit and because of excessive kinetic energy dissipation on the circuit if the beam is not perfectly focused.

The reason for the second of these effects is indicated in the sketch of Figure 19. Electrons following cycloiding trajectories have an average velocity equal to the E/B drift velocity, but the instantaneous velocity is greater than the average velocity when the electrons are above the mean position of their trajectory. Correspondingly, the electron velocity is less than the average velocity when the electrons are below this mean position. Collection of electrons on the anode occurs near the top of the cycloid and thus at a velocity exceeding the average E/B drift velocity. Therefore, the energy dissipated is greater than that corresponding to V_o the amount depending on the degree of cycloiding. To express this, a factor k is introduced into equation (4) to give:

$$\text{efficiency} = 100\% \left(1 - \frac{kV_o}{V_a}\right) \qquad (5)$$

The magnitude of k varies from 1 for a perfectly focused beam to 4

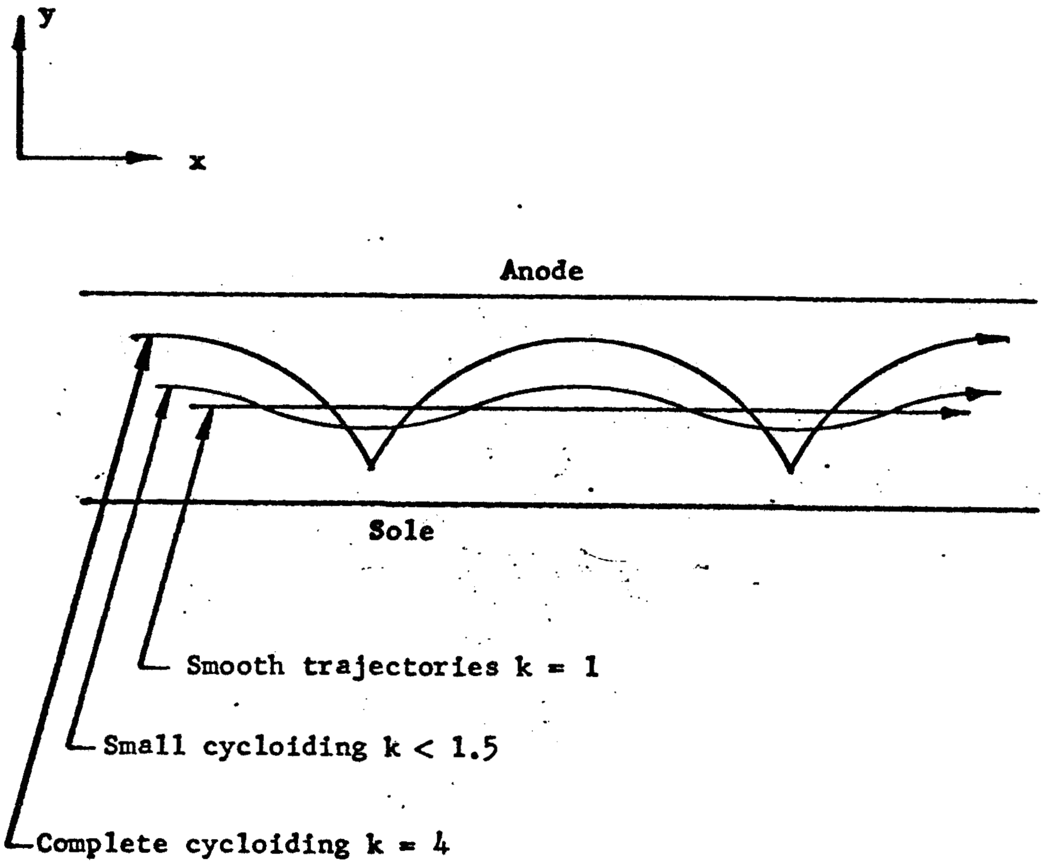

FIGURE 19 SKETCH SHOWING CYCLOIDING TRAJECTORIES

Collection of electrons on the anode occurs near the top of cycloid where velocity is maximum. Velocity in the x direction is given by:

$$v_x = v_o \left[1 + (\sqrt{k} - 1) \sin \omega_c t\right]$$

$$\omega_c = (e/m) B$$

k = cycloiding voltage factor

Where e/m is the charge to mass ratio for an electron, B is the magnetic field and v_o is the synchronous velocity.

for a completely unfocused beam (as occurs in an emitting sole CFA) which has twice the drift velocity at the top of a cycloid. Computer simulation analysis of the S-band amplifier design indicates a k value of about 1.1. This value of k reduces the theoretical energy conversion efficiency to 89%. The effect on conversion efficiency of beam cycloiding is significantly reduced by the high V_a to V_o ratio.

In a crossed-field amplifier, unfavorably phased electrons can reduce the saturated power output and efficiency. If the tube is made long enough, all electrons are eventually phase focused into the favorable phase and strike the delay line. We then have an extended saturation region, as sketched in Figure 20. This extended saturation region occurs since unfavorably phased electrons are being phase focused over this region and are contributing to the circuit wave, although at a significantly reduced rate since less current is interacting. The additional circuit length and the attenuation required to phase focus the remaining current generally result in a decrease in the power output and efficiency. To avoid this, the interaction is terminated after the favorably phased electrons have fully interacted. This region is indicated on the curve presented in Figure 20. This leaves about one-third of the current in the unfavorable phase. This current has gained energy at the expense of the RF wave and moved toward the sole from the original beam position. As a consequence it will collect on a collector element at cathode potential. This improves efficiency greatly as compared to collecting this current at anode potential. However, some power is still wasted because the unfavorably phased electrons are accelerated from a potential less than cathode potential to cathode potential. To some extent, this wasted power may be reduced by the phase focusing properties of the reflector electrode.

The fact that the velocity of the electrons remains synchronous with the circuit wave in a crossed-field amplifier means that as

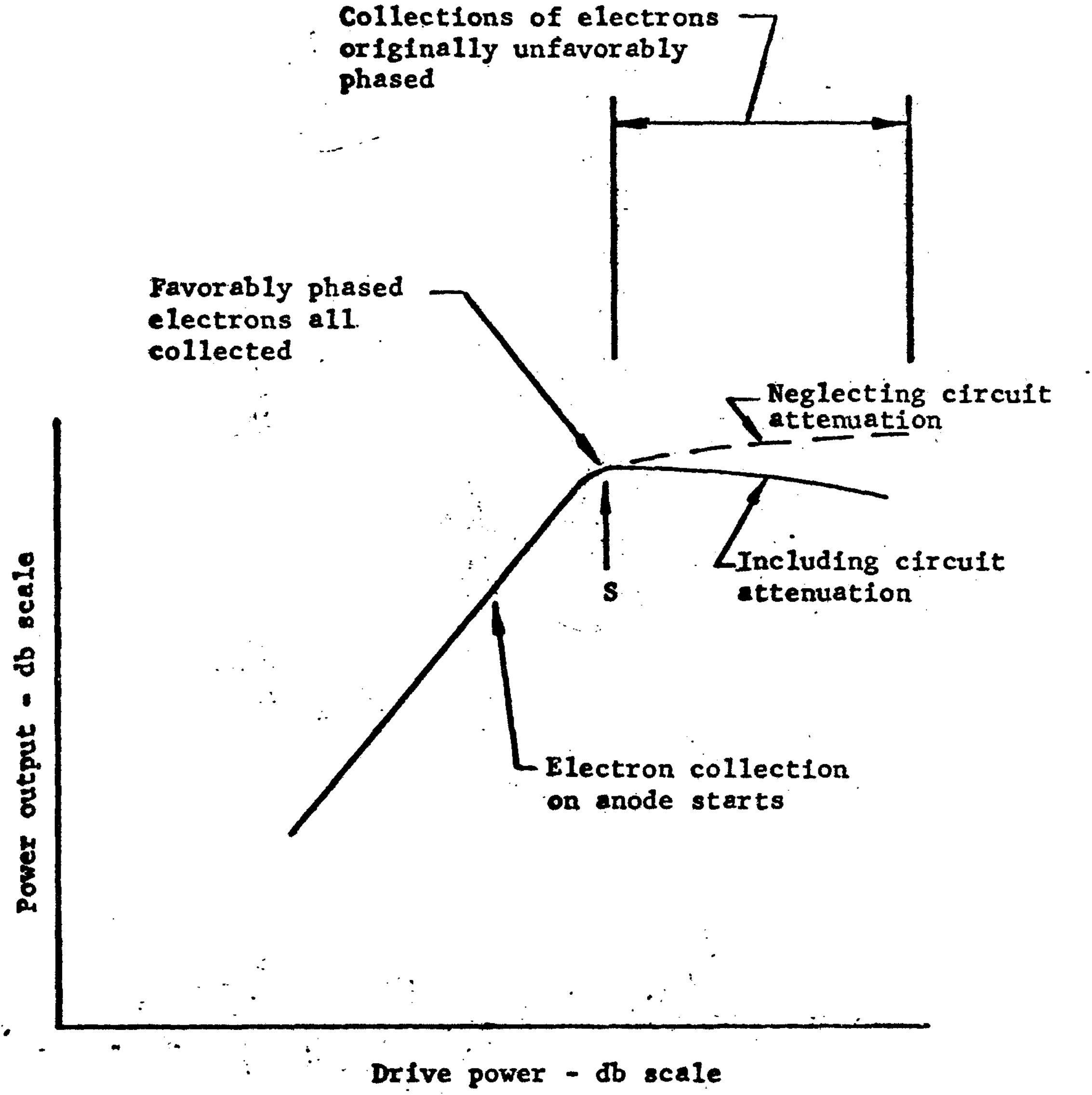

FIGURE 20 SKETCH OF SATURATION CURVE SHOWING WHERE ELECTRONS ORIGINALLY FAVORABLY PHASED AND ORIGINALLY UNFAVORABLY PHASED ARE COLLECTED

The electrons which are originally in the unfavorable phase are gradually phased focused into the favorable phase and collected on the anode. In practice, the tube is driven to point S and the unfavorably phased electrons are collected on a cathode potential collector element.

the bunches are formed, they remain centered in the favorable phase of the RF wave. This, in turn, means that there is relatively little pushing of the phase of the circuit wave as the amplitude of the RF drive is changed. Thus, AM to PM conversion, which contributes to the generation of intermodulation products, is minimized in injected beam crossed-field amplifiers. We have not made detailed experimental studies of this characteristic on our present CFA programs. However, the relative phase shift of the wave with respect to the cold circuit wave is printed out in our computer simulation of the CFA, and from this we can obtain computed values of the AM to PM conversion. The numbers are in the vicinity of 1 degree per db, an order of magnitude less than they are with O-type traveling wave tubes. (It should be noted that AM to PM conversion can also be obtained from computer simulations for O-type tubes and that the values are close to those which are measured on actual tubes.)

A property of crossed-field sheet beams which is substantially different from O-type beams is the ability of the crossed-field beam to amplify in the absence of a slow wave circuit. This amplification comes about due to a slipping stream effect and is often known as diocotron gain. This diocotron gain contributes substantially to the low level gain of the CFA, but it saturates at power levels substantially below the final saturated output power. The existence of this slipping stream gain gives rise to a power input versus power output characteristic as shown in Figure 21. As the drive power is reduced below that required for saturation, there is a gradual increase in gain until the ultimate low level gain is reached. The difference between the high level and low level gain is dependent upon a space charge parameter and the length of the tube. For a tube operated near or at saturation, we need not be concerned about the high values of low level gain. If, however, it is desired to obtain linearity over some dynamic range, a means of making the high and

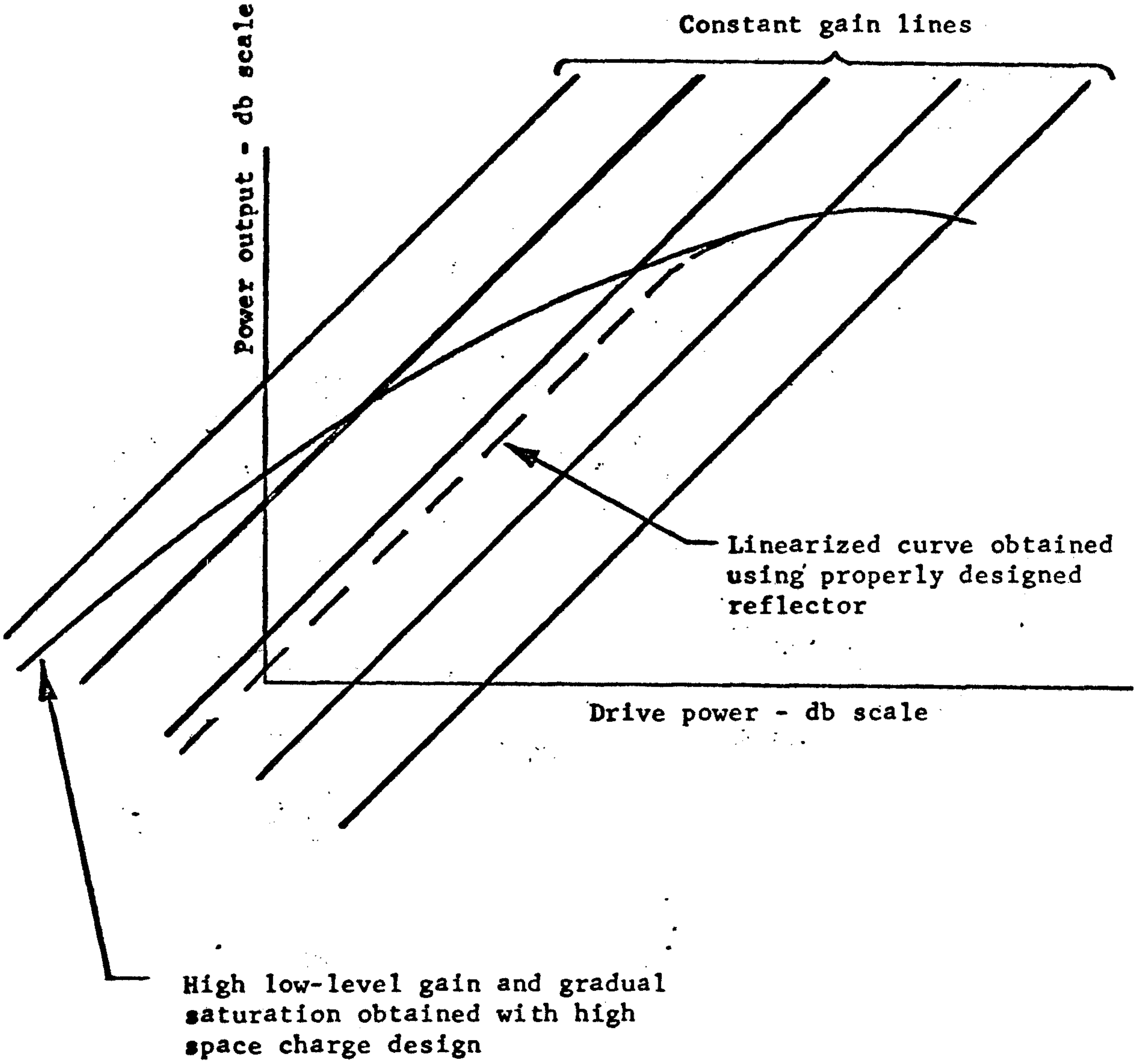

Linearized curve obtained using properly designed reflector

High low-level gain and gradual saturation obtained with high space charge design

FIGURE 21 SKETCH OF POWER OUTPUT VERSUS POWER INPUT CURVES SHOWING GRADUAL SATURATION FOR HIGH VALUES OF SPACE CHARGE PARAMETER AND LINEARIZATION RESULTING FROM USE OF PROPERLY DESIGNED REFLECTOR.

low level gains more nearly equal is required. The Vaxitron concept provides a means of doing this through the use of phase shifts of the electrons relative to the circuit wave every time the electrons are reflected from the side of the interaction space. This concept will be discussed later.

4.3 Beam Collection

Figure 22 shows a multi-element collector system that can be used in a crossed-field device. This collector takes advantage of the fact that the electrons in the spent beam are already spatially sorted, with those electrons which have given up the greatest amount of energy being close to the anode. All electrons have approximately the same velocity in the x direction in Figure 22. The crossed-field collector system also takes advantage of the fact that the E/B drift velocity is in the positive x direction only. Thus, electrons cannot be reflected from the collector system back down the tube toward the gun. This is an important limitation on the design of multi-element collector systems for O-type tubes. In the crossed-field collector system, we first increase the anode to sole spacing. This reduces the dc electric field and consequently, the x directed kinetic energy of the spent electrons. If this reduction in electric field takes place gradually, the electrons simply move away from the anode toward lower potentials and their forward directed velocity is reduced. We then enter the multiple element collector system itself. This consists of a number of branches in the interaction space with the higher potential branches located at right angles to the continuation of the main interaction space. The natural direction of electron flow is thus toward the lower potential branch of the collector system. Only if an electron cannot energetically enter the low potential branch will it turn around and go up the high potential branch. Branching systems of this sort have been studied on the computer and it is found

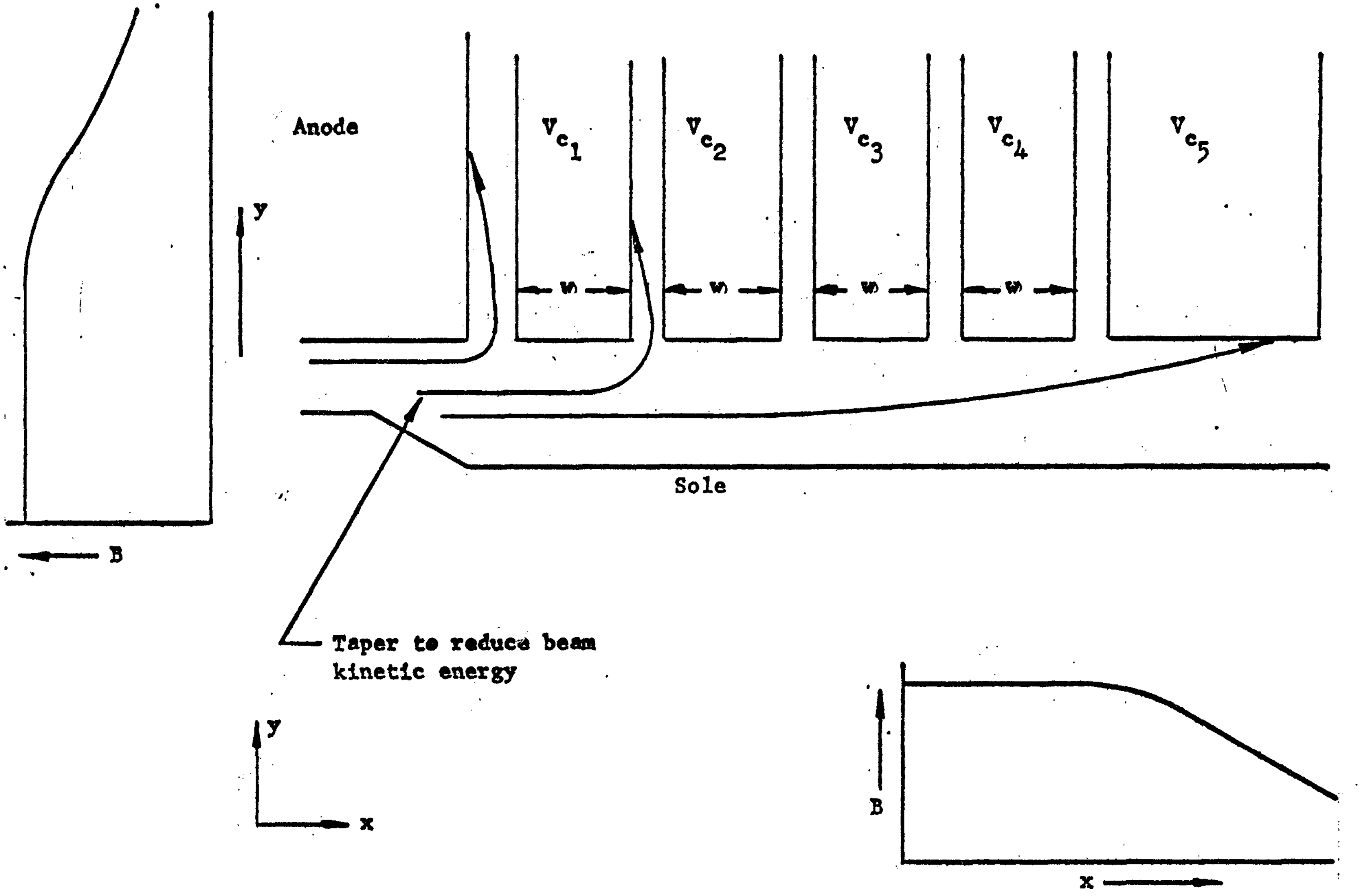

FIGURE 22 SKETCH OF COLLECTOR SYSTEM SHOWING HOW MAGNETIC FIELD DECREASES VERTICALLY AND AT END OF TUBE TO PERMIT ELECTRONS TO COLLECT

that they do an excellent job of sorting the spent beam with practically none of the electrons entering a higher potential branch than is necessary. Once the electrons have been sorted by the branching collector, they move down the vertical channels, as shown in Figure 22. The magnetic field is gradually reduced along these channels (the channels simply run out of the region where the magnetic field is high) and collection then occurs on the high potential surface of each branching channel. Beam collection can also be accomplished by increasing the electric field in the gap between the collector elements. This would require a tapered gap spacing between the collectors. As we increase the number of collector elements employed, we increase the dynamic range over which we can maintain efficient operation. When the tube is operating at saturation, only a single branch and a single collector element appears necessary to obtain efficient operation. In this case the single depressed collector element is run at the cathode potential so that an extra collector voltage is not required. Such a single element depressed collector is a regular feature of our conventional injected beam CFA and it operates about as the computer simulations predict it should. Multiple collector branches are now being intruduced into experimental tubes. It should be noted that the multiple element collector is employed here not to optimize the efficiency at saturation, but to optimize efficiencies at power levels less than saturation where the beam has not fully interacted. For operation at saturation, a single element at cathode potential is all that is required. To optimize efficiency at output power levels below saturation requires additional collector elements since the beam has a greater position spread.

An important question about operation with multiple element collectors is whether we gain efficiency in the CFA more rapidly with multiple voltages than we lose it in the power supply system. Figure 23 shows a sketch of a type of power supply system which has been

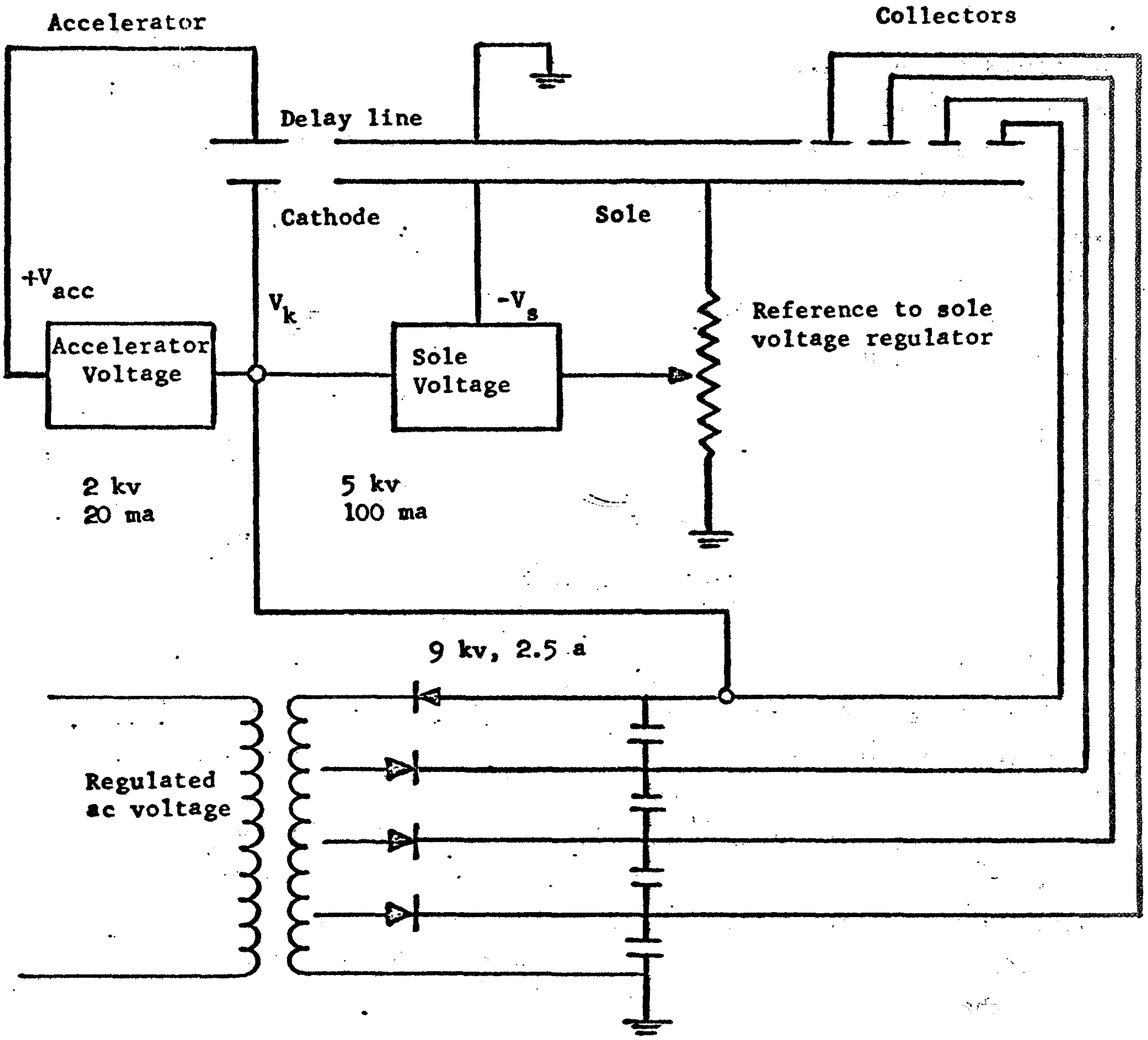

FIGURE 23 SKETCH OF POWER SUPPLY SYSTEM

A tapped transformer is employed to develop multiple collector voltages. The sole supply is regulated by a reference voltage to ground so that the sole to ground voltage may be held tighter than the cathode to ground voltage without requiring as tight a regulation on the high current cathode supply.

considered for satellite applications and which we have been informed can be made to produce the multiplicity of voltages without sacrifice in power supply efficiency. Some size and weight increase is needed but this is believed to be less than 15% for up to 10 collector voltages. This system involves use of tapped power transformer with individual rectifiers for each voltage. Total energy storage is about the same as in a single voltage supply, so the main increase in size comes from the added rectifiers and a somewhatlarger transformer. It can be seen that energy losses are not increased and thus power supply efficiency is not reduced by this arrangement. Fundamental to this approach is the assumption that the collector voltages do not have to be individually adjusted and that their regulation may be somewhat poorer than that of the main cathode voltage. This is the case for the proposed Vaxitron amplifier.

4.4 The Magnetron Injection Gun

It is evident from Figures 15 through 17 that the beam used in the Vaxitron amplifier could alternatively have been injected into the interaction space from the end, and this is what is done in the conventional injected beam crossed-field amplifier. We have found, however, that injection from the side has three significant advantages. First, the axial injection guns have a substantial advantage in the trade-off between noise and cathode current density. Crossed-field guns of the type used for end injection in conventional crossed-field amplifiers become noisy if the width of the cathode becomes an appreciable length in the direction of the beam flow. These noise effects were studied in detail under previous U.S. Army contracts to CSF (Contract No. DA91 591). To avoid such noise generation, it is necessary either to use a short width cathode with resulting high current densities and compromises in tube life, or alternatively, to grid the cathode. Grids in a high power tube of this sort, however, also compromise life and reliability. A principal advantage of the axial injection gun is thus the noise reduction relative to the conventional injected beam gun, which occurs as a result of the tilt of the cathode with respect to the magnetic field. This noise reduction has also been observed in studies of magnetron injection guns for O-type tubes by a number of investigators. The reduction in noise in the axial injection gun, in turn, permits us to operate with larger area cathodes and thus at cathode current densities which are compatible with a substantially increased life requirement. A second important advantage of the axial injection gun is that the resulting axial velocities and consequent reflection of the beam from the sides of the interaction space permit us to introduce the phase shifts which linearize the RF dynamic range characteristics of the tube. We will return to a discussion of the reflector operation in the next paragraph. A third advantage of side injection is that distribution of current injection along the side of the interaction space also results in distribution of the location where electrons strike the circuit and thus reduces power dissipation density. Figure 24 is a cross-section view of an axial injection gun used in a VHF crossed-field amplifier. Guns used in higher frequency tubes are quite similar in principle.

4.5 The Reflector Design

Linearization of the RF output vs. input characteristic (RF dynamic range characteristic) can be accomplished through the shaping of the reflector electrodes. During the time when electrons are near the reflector they are in a region with a y directed dc electric field (Ey) which can be greater or less than that in the main interaction space, depending on the reflector shape. This can be seen in Figure 25, which shows a sketch of the fields in the vicinity of the reflector. This figure is a representation of the type of reflector currently used in which the Ey fields are reduced in the reflector region. The geometry used has been determined by computer studies of the trajec-

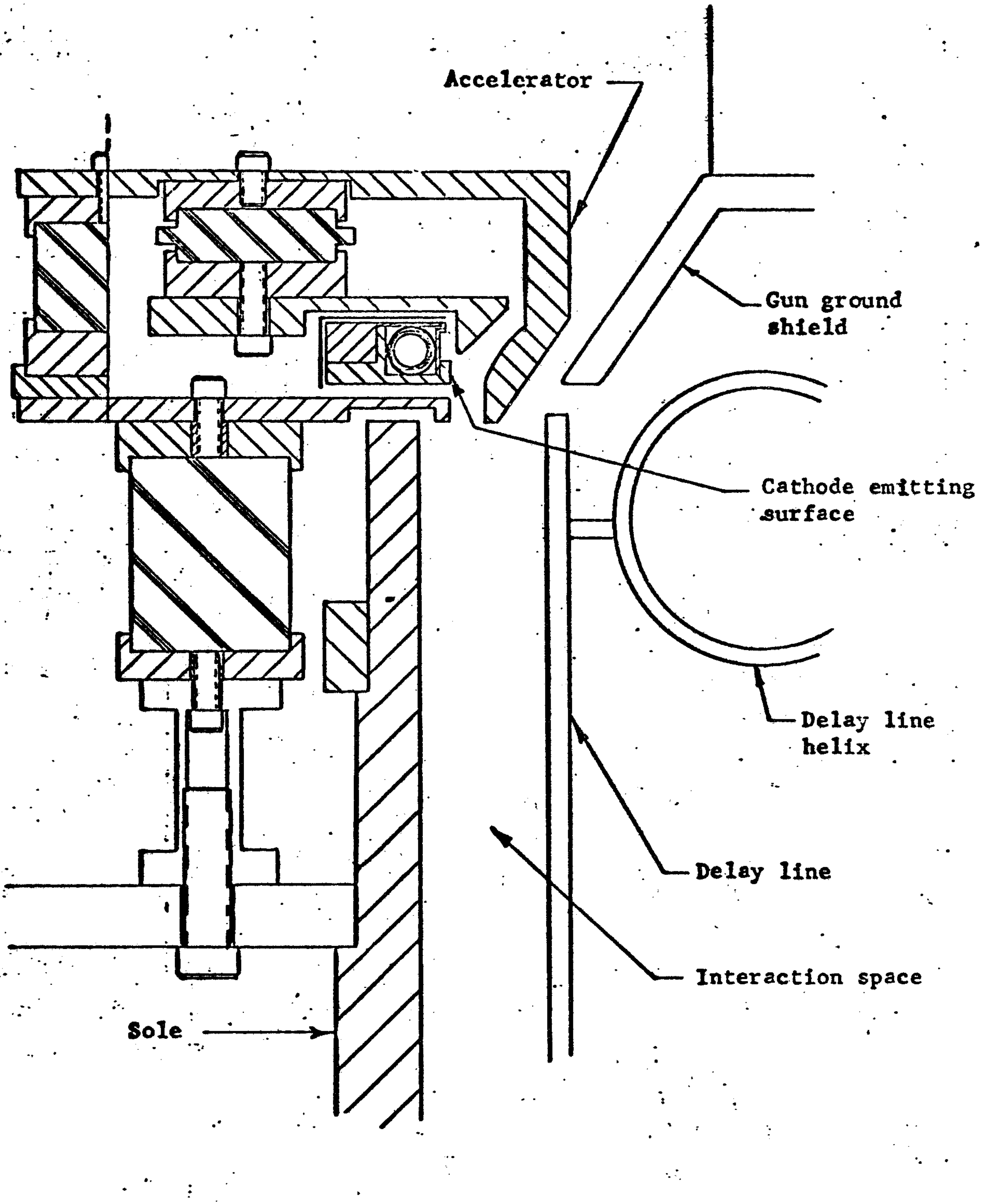

FIGURE 24 CROSS SECTION OF PRESENT VHF AXIAL INJECTION GUN

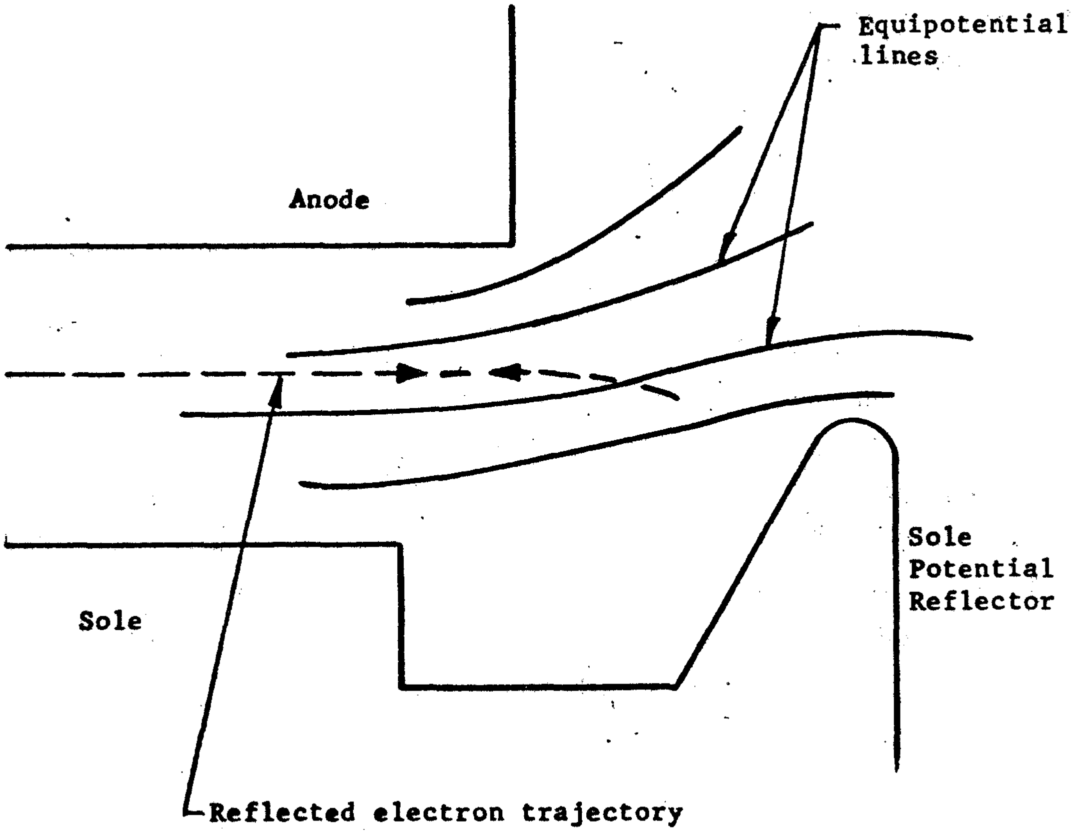

FIGURE 25 SKETCH SHOWING TRAJECTORIES AND EQUIPOTENTIALS IN THE VICINITY OF THE PREBUNCHING COLLECTOR. Reflected electrons return along almost identical path as incident trajectory.

tories in the collector region. As a result of the reduced Ey, the velocity in the x direction (direction of wave propagation) is reduced in the reflector region and consequently a reflected electron is delayed in phase relative to the RF circuit wave. Electrons near the top and bottom of the beam have different axial velocities and therefore undergo a different number of reflections from the side collectors and thus differing relative delays with respect to the circuit wave. This upsets the bunching process to some extent and reduces the high gain which can occur under small signal conditions.

Under large signal conditions, the differential phase shifts are less effective in reducing gain. There are two reasons for this. First, the reflector is designed so that the phase shifts introduced decrease as the beam moves from its original injection position toward the anode. Second, the strong phase focusing forces of the RF wave make the differential phase shifts much less effective in reducing gain.

Using this differential phase shift technique we have been able to extend linear operation and zero signal stability to beam currents (and thus power outputs) several times larger than those that were previously the limit for linearity.

5.0 DESIGN OF THE S-BAND EXPERIMENTAL VEHICLE

In this section we will discuss the design of the experimental tube starting with the delay line and then proceeding to the gun, the side reflectors, the RF interaction calculations and the collector design. The background material, in some cases represents theoretical results obtained on other programs and subsequently applied to this program. The original study of the phase shift undergone on reflections was conducted in this program. The results of the computer studies discussed in section 3 of this report and discussions of these results led, in turn, to the derivation of the "Brillouin Conditions" for an axial injection beam which were finally carried out on RADC Contract F30602-69-C-0205. Some of the key derivations made on the RADC study are included as unclassified appendicies in reference 7. Reference will be made to this set of appendicies in the following discussion.

5.1 The Delay Line

The type of delay line employed on this program is known as a meander line. Figure 26 shows a sketch of this type of line with the dimensions which are used in the experimental tube on this program. The meander line can be viewed as a strip line above a ground plane. Propagation occurs along the meandering path at a velocity equal to the velocity of light, taking into account the slight reduction because of dielectric loading. The phase velocity along the direction of beam propagation is thus approximately equal to the velocity of light multiplied by the ratio of the line pitch to its width.

The particular line employed on this program is not optimum for the ultimate application because it does not provide an optimum trade-off between thermal capability, interaction impedance and attenuation. Further, it is centered somewhat higher in frequency-3.0 GHz rather than 2.0 GHz. It was chosen for the present experi-

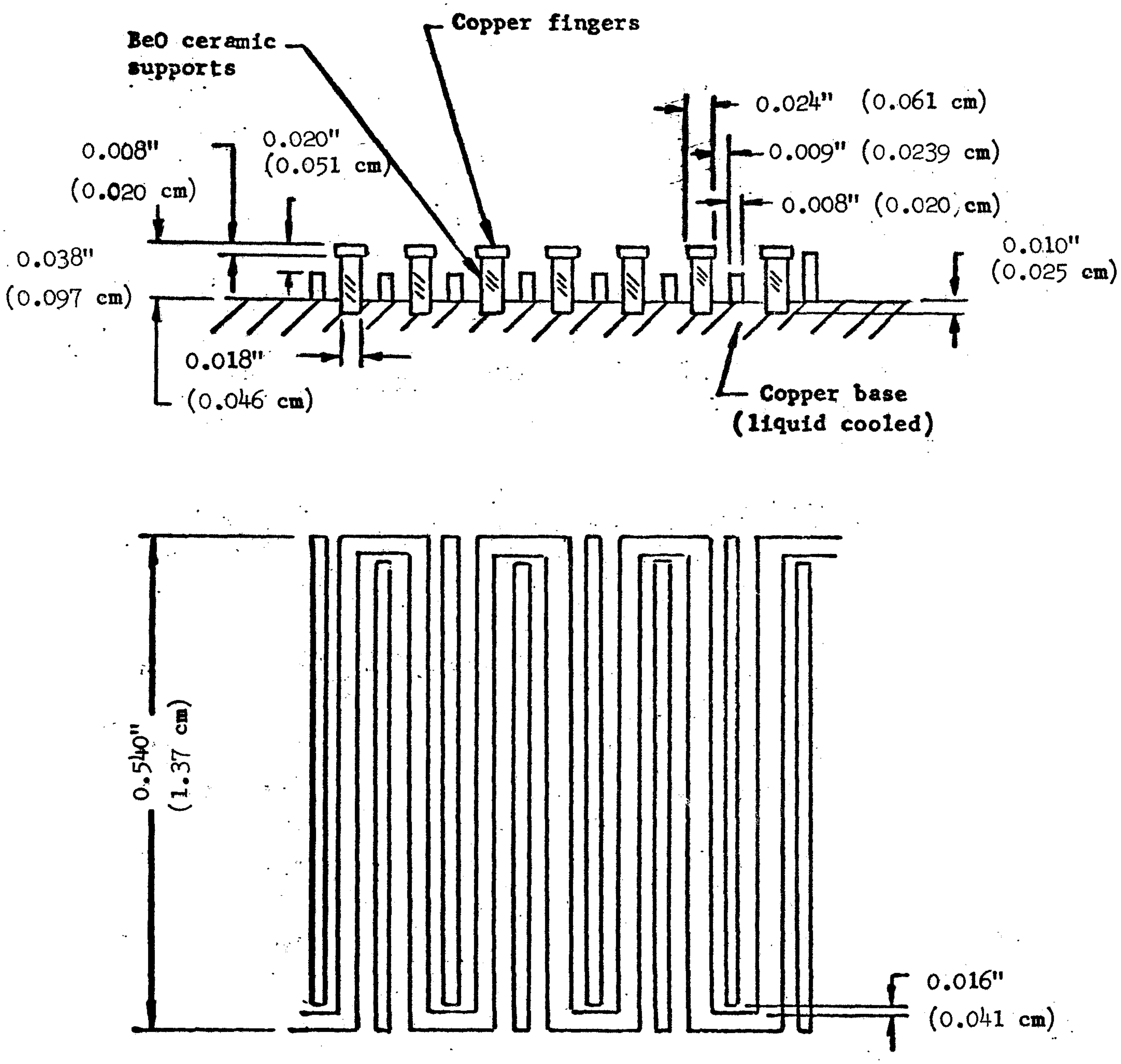

FIGURE 26 MEANDER LINE FOR USE IN THE S-BAND AXIAL INJECTION CFA.

Dimensions are in inches (cm).

mental program because it was readily available through modification of a related existing design.

The meander line is supported from the base by beryllia ceramics. The line is brazed to the ceramics and the ceramics are in turn brazed to the base using a copper-silver eutectic brazing alloy. The relatively short path of the high thermal conductivity beryllia ceramic results in a high power dissipation characteristic for this type of delay line. Liquid cooling channels are located directly beneath the beryllia ceramics and form part of the delay line subassembly.

The dispersion characteristics of the shielded meander line are a composite of the effects due to capacitive coupling of adjacent fingers and due to the reflection introduced at the turnaround points of the meander line. The first of these effects is considered in a formula developed by Mourier and LeBlond (Ref. 9) and by Arnaud (Ref. 10). Figure 27 gives the definition of the capacity coefficients employed in this formula. In terms of these coefficients, the dispersion is given by:

$$\cos k\ell = \frac{\cos \frac{\Theta}{2}}{1 + 2 \frac{C_{12}}{C_{10}} \sin^2 \frac{\Theta}{2}} \qquad (6)$$

where Θ = phase shift per section of the circuit

$k = \omega/c$

ω = radian frequency

c = velocity of light

The capacity coefficients of C_{10} and C_{12} are defined in Figure 28. From this formula it is seen that the dispersion is minimized by minimizing the finger-to-finger capacity C_{12} as compared to the finger-to-

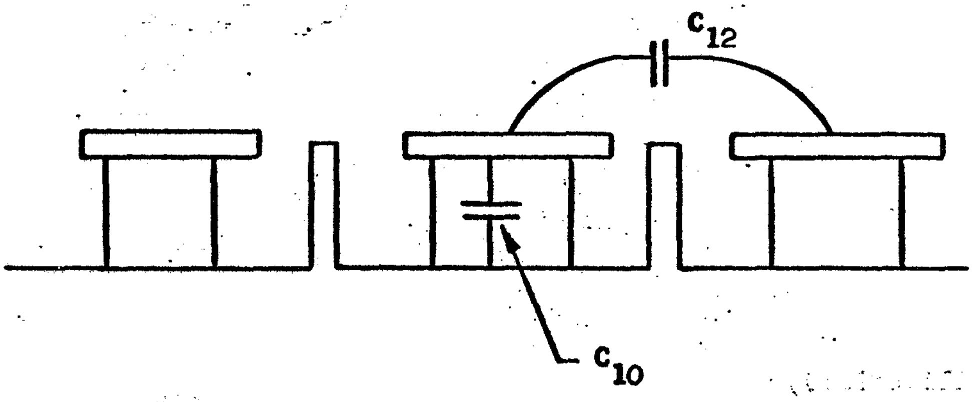

FIGURE 27 THE MOURIER-LEBLOND CAPACITY COEFFICIENTS

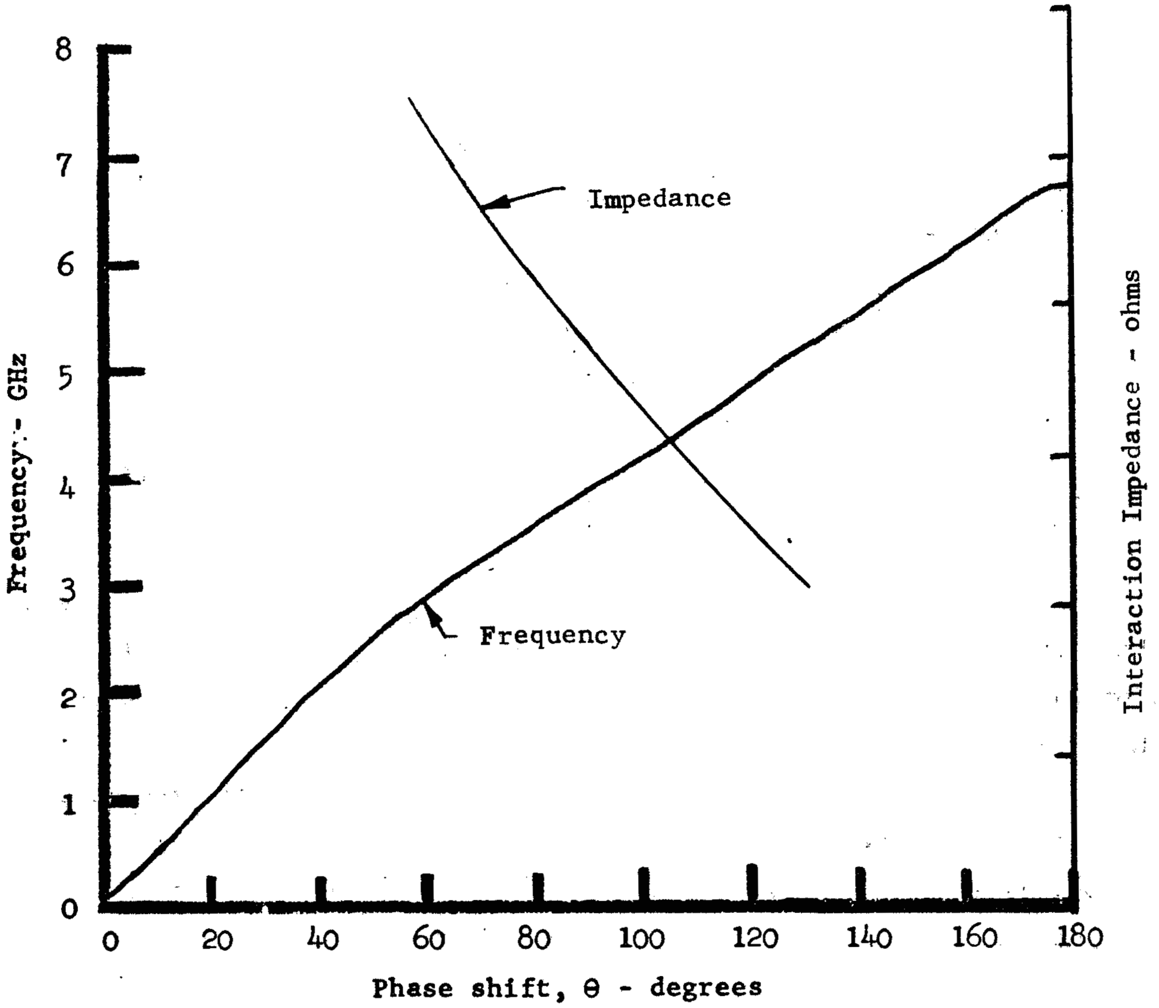

FIGURE 28 DISPERSION AND INTERACTION IMPEDANCE FOR THE S-BAND SLOW WAVE CIRCUIT.

ground capacity, C_{10}. This is the function of the shields in the shielded meander line.

To obtain the effects of the meander line turn-around on the dispersion, we must turn to Campbell's equation, which is given by:

$$\cos \Theta = \cos k\ell - \frac{B}{Y_o} \sin k\ell \tag{7}$$

or

$$\cos \Theta = \cos k\ell - \frac{X}{Z_o} \sin k\ell \tag{8}$$

where Θ is the phase shift per section of the loaded line

ℓ is the line length per period (approximately equal to the meander line width

B is the shunt susceptance of the bend

X is the series reactance of the bend

Y_o is the characteristic admittance of the unloaded line

Z_o is the characteristic impedance of the unloaded line

$Z_o = 1/Y_o$

This equation shows that the dispersion is minimized by making the bend of the meander line as reflectionless as possible. Reflections from the bend are the source of the stop band centered around π phase shift per section.

In theory, it is possible to construct a complete mathematical model of the meander line by employing the results of the Mourier-LeBlond equation to obtain the characteristics of the transmission line section as a function of frequency and then by using these results to determine a frequency dependent Θ_0 to employ in

Campbell's equation to obtain the final dispersion curve. In practice we have resorted to an experimental approach using the theory as a guide rather than trying to carry the calculations into this detail.

Figure 28 shows the experimentally determined dispersion and interaction impedance characteristics for the delay line sketched in Figure 26. The dispersion is low enough to provide a fixed voltage bandwidth of 200 MHz. There is adequate dispersion to insure that the upper band edge frequency is not synchronous with the beam so that oscillations at this frequency will be avoided.

Since the meander line is essentially a two-wire line insulated from ground, it has a characteristic impedance between the line and ground which is constant as a function of frequency. This impedance may be measured experimentally using a time domain reflectometer. Such measurements have shown the characteristic impedance to ground to be 65 ohms. This is the impedance that we must match to from the external lines. The fact that this impedance is relatively constant as a function of frequency greatly assists our matching to the delay line. Once the characteristic impedance to ground is known we can calculate the interaction impedance, which in turn gives us a measure of the electric field strength available to interact with the electron beam. This calculation proceeds by determining the difference in the voltage between finger and ground for two adjacent fingers and setting this equal to the voltage difference between the two fingers. In this manner we can relate the interaction impedance to the characteristic impedance of the line. Details of this derivation are given in Appendix I of Reference 7. In the process of carrying out this derivation it is also necessary to take into account the voltage variation axially along the fingers. As is obvious from reference to the sketch of the 1 ine in Figure 26, the voltage difference between fingers is zero at the turn-around and maximum at the side opposite the turn-around. In our derivation we have taken this effect into account approxiamtely by averaging the impedance at the center and at the sides of the line. The resulting expression for the interaction impedance in terms of the characteristic impedance is given by:

$$K = Z_o \left[\frac{\sin \frac{\theta_g}{2}}{\frac{\theta_g}{2}} \right]^2 \left[\frac{\sin \frac{\theta}{2}}{\frac{\theta}{2}} \right]^2 \left[\frac{1}{2} + \frac{1}{8} \frac{\sin^2 \theta}{\sin^2 \frac{\theta}{2}} \right] \qquad (9)$$

where Z_o is the characteristic impedance of the line
θ is the phase shift per section
θ_g is the gap transit angle

The first of the three factors multiplying the characteristic impedance Z_0 in the above expression will be recognized as the gap factor, which gives the component of the fundamental RF field in terms of the total field across a gap. The second factor results from taking voltage differences between adjacent fingers. The third factor takes into account the variation of impedance across the axial height of the circuit. In practice, each section of the circuit consists of two gaps, one on each side of the ground shield. In our calculation we have neglected this and taken the gap factor as if the shield were absent. We believe that this causes only minor errors in our impedance calculations. Using the above expression we have calculated the interaction impedance as a function of the frequency and included the result in Figure 28. This method of determing the interaction impedance is thus a combination of a theoretical and an experimental method. The iterative impedance of the line is determined experimentally from time domain reflectometer measurements and from this the interaction impedance is calculated using the above expression.

The interaction impedance may also be determined experimentally using perturbation techniques. To employ these techniques, the line is resonated by introducing large reflections at the meander line to coaxial line transducers at the ends of the line. The shift in the resonant frequency is then measured when a thin sheet of dielectric is placed over the face of the line. The interaction impedance can be related to the percentage of shift in the resonant frequency. The expressions employed for reduction of this frequency shift data are derived in Appendix II of Reference 7. Using these expressions, we have measured the interaction impedance of shielded meander lines and compared the results with those obtained from the characteristic impedance measured with the time domain reflectometer. The two techniques agree within about 20%.

Another important characteristic of the delay line is its attenuation. Figure 29 shows the experimentally determined attenuation as a function of frequency for the line employed in the experimental tube. The attenuation values are given in terms of db/in and cm of circuit length. This is the characteristic of importance since it is the ratio of the gain per unit length to the attenuation per unit length, which determines the reduction of efficiency caused by the attenuation. This ratio is of importance only near the RF output where the RF power levels are significant. Higher values of circuit attenuation may be used near the input where the power levels on the delay line are comparatively low without degrading circuit efficiency. In the experimental tubes this has been done by iron plating the delay line over the first two inches of circuit length. This increase in circuit attenuation provides an improved isolation between the RF input and the RF output and enhances stability. The iron plating increases the attenuation in the input portion of the tube by a factor of about two over the values shown in Figure 29. The total insertion loss of the five inch length of line is thus approximately 8 db at 3 GHz.

Although high average power is not an objective of this immediate program, the delay line is capable of supporting high

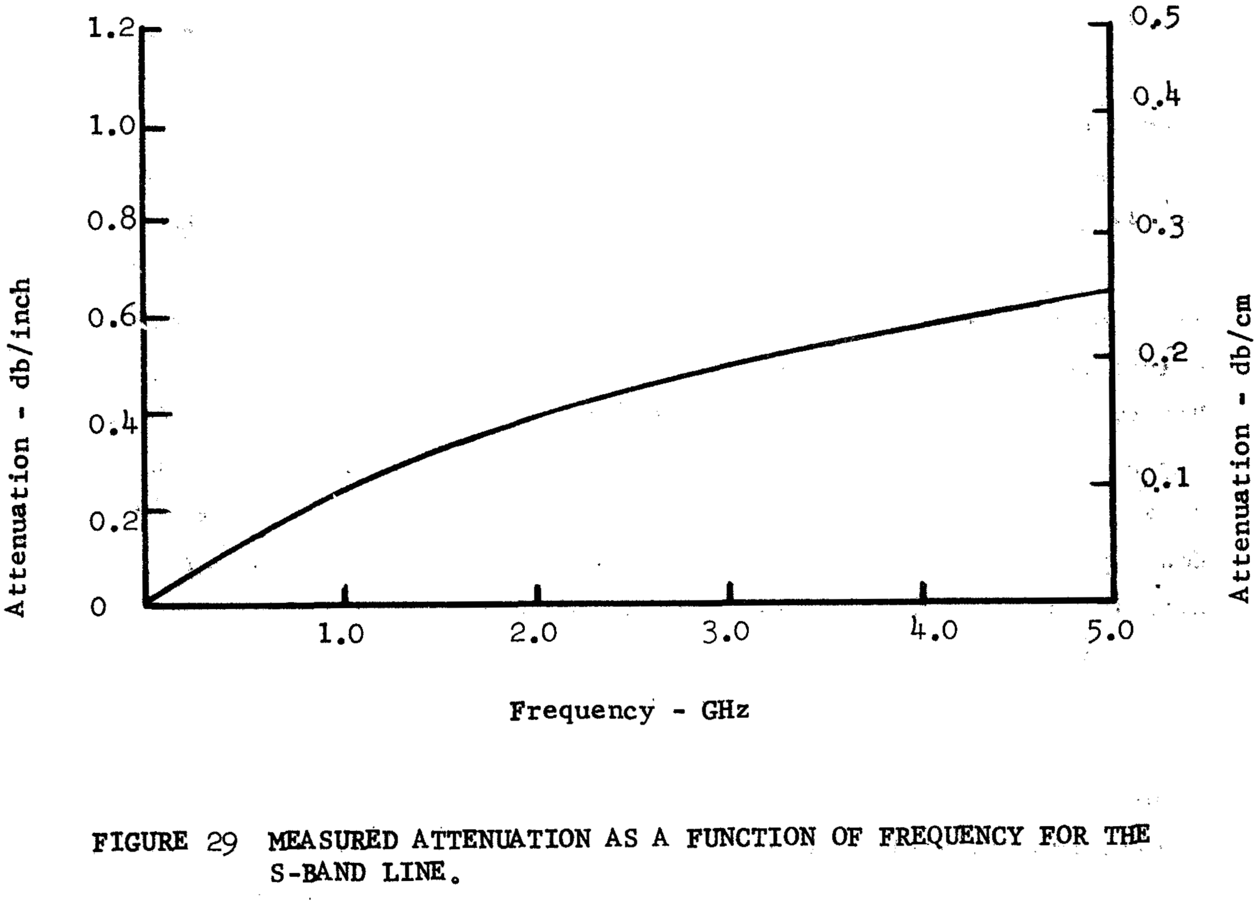

FIGURE 29 MEASURED ATTENUATION AS A FUNCTION OF FREQUENCY FOR THE S-BAND LINE.

average power. We have calculated the thermal impedance in degrees centigrade per watt of power flow from the line to the base. For a single circuit period it is 0.85° C/watt. In the FM mode of operation the maximum dissipation per finger will be about 80 watts so the temperature differential between line and base will be about 70° C. In the AM mode of operation the temperature differential will, of course, be less.

Measurements of the thermal impedance of similar lines have been made using the tester shown in Figure 30. Using this tester and a water cooled base, powers of 135 watts per ceramic have been dissipated without damage to the ceramics in a line having twice the thermal impedance. A separate verification of the thermal calculations has also been obtained by passing 60 cycle current through a delay line and measuring the temperature differential between the delay line and coolant using temperature sensitive liquid crystals.

5.2 The Axial Injection Gun

5.2.1 General Principles

Figure 17 showed the general configuration of the axial injection gun. This type of gun is similar in concept to magnetron injection guns which have previously been used in voltage tunable magnetrons and in certain types of TWTs and klystrons. Beam formation in this type of gun has been studied theoretically by Kino and Taylor (Ref. 8). The reasons we have considered this type of a gun in place of the conventional injected beam gun were listed in the introduction. Its potential for lower current density is illustrated by Figure 31, which shows a comparison of the cathode for the axial injection CFA with that employed in a conventional injected beam CFA using the same type of delay line. The long dimension of the axial injection gun can be increased up to two inches, as compared with 0.550 for the injected beam gun. For the same value of the narrow dimension, the

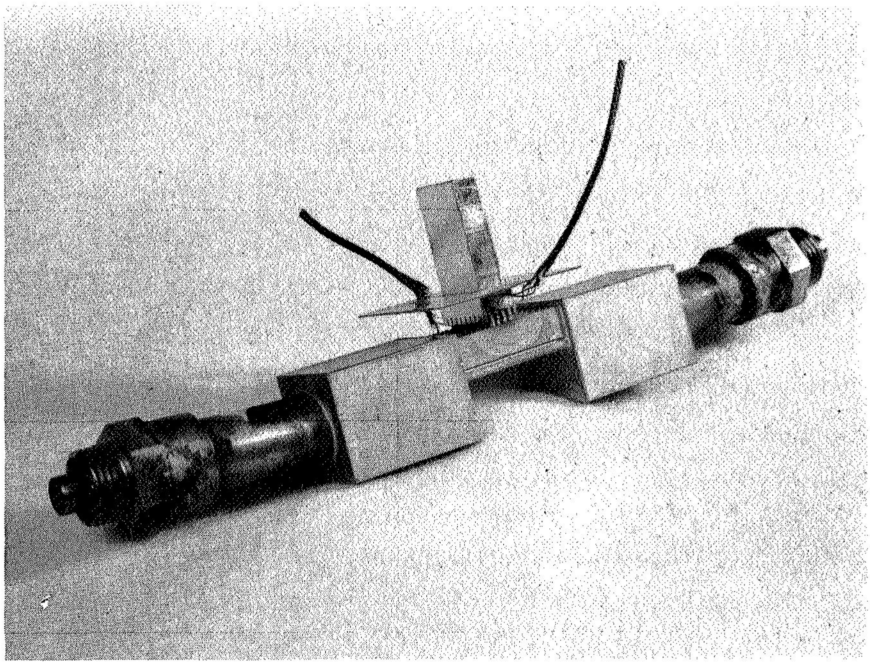

FIGURE 30 THERMAL IMPEDANCE TESTER

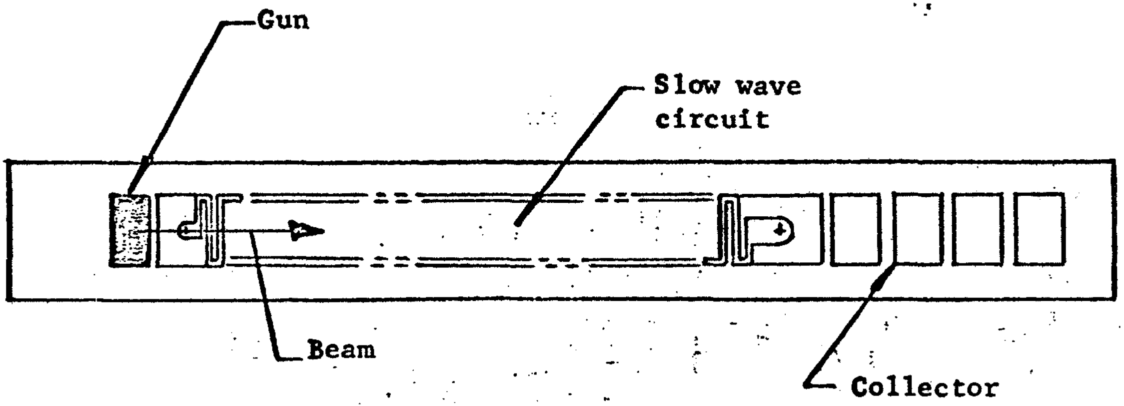

a. Injected beam CFA gun

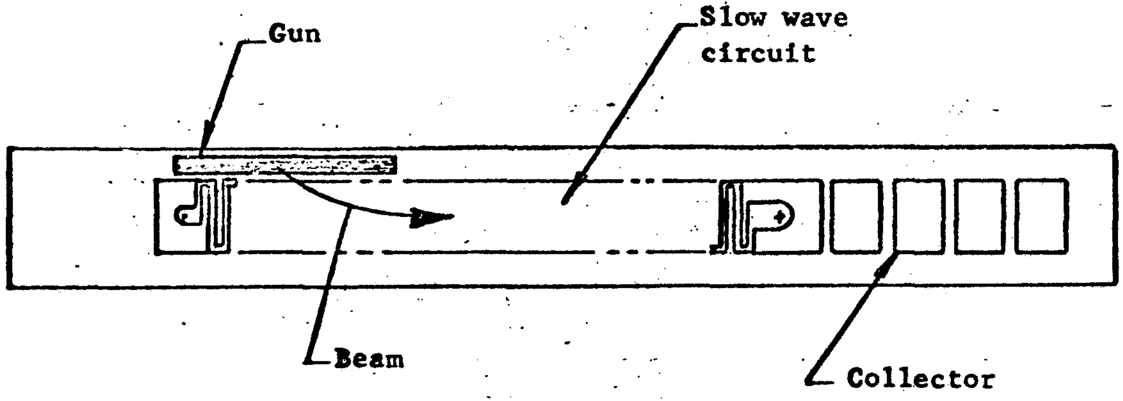

b. Vaxitron axial injection gun

FIGURE 31 SCHEMATIC REPRESENTATION OF AN INJECTED BEAM CFA GUN AND A VAXITRON GUN current density for the axial injection gun will thus be lower by a factor of about 4. At the same time, we believe that because of the noise control properties of the tilted cathode in the axial injection gun we can increase the narrow dimension of the cathode compared to that which would be employed in an ungridded conventional injected beam gun. This means that the axial injection gun could have a current density advantage of at least a factor of 5 compared with an ungridded conventional injected beam gun using the same delay line width. It has been shown that the noise in conventional injected beam guns may be reduced by placing a grid over the cathode. This mades it impossible to increase the narrow dimension in Figure 31 for the conventional injected beam gun. However, if this is done, the current density does not decrease as rapidly as one might initially expect because the grid wires tend to concentrate the current density in the region between the wires. It is our belief that as we increase the cathode width in the injected beam gun by a factor of two, by employing a grid we reduce the peak current density by a factor of only about 1.5. The introduction of the grid in an injected beam tube also provides an element which may significantly reduce the life and reliability of the tube. There thus appears to be a substantial advantage to the axial injection gun in terms of current density as well as life and reliability. In the experimental program we have employed a gun having a width of only 0.050 rather than the 0.150 which we believe is ultimately feasible. This limits our advantage in current density to a factor of about 2 times as compared with a conventional injected beam gun. This, however, is still significant. The resulting current density of the gun employed is 1.9 a/cm^2. With a wider cathode and operation at lower current and higher voltage, the current density can be reduced to about 0.5 a/cm^2.

Figure 32 shows the three regions of the axial injection gun. Region 1 is what we call the Kino region. Here the space charge flow

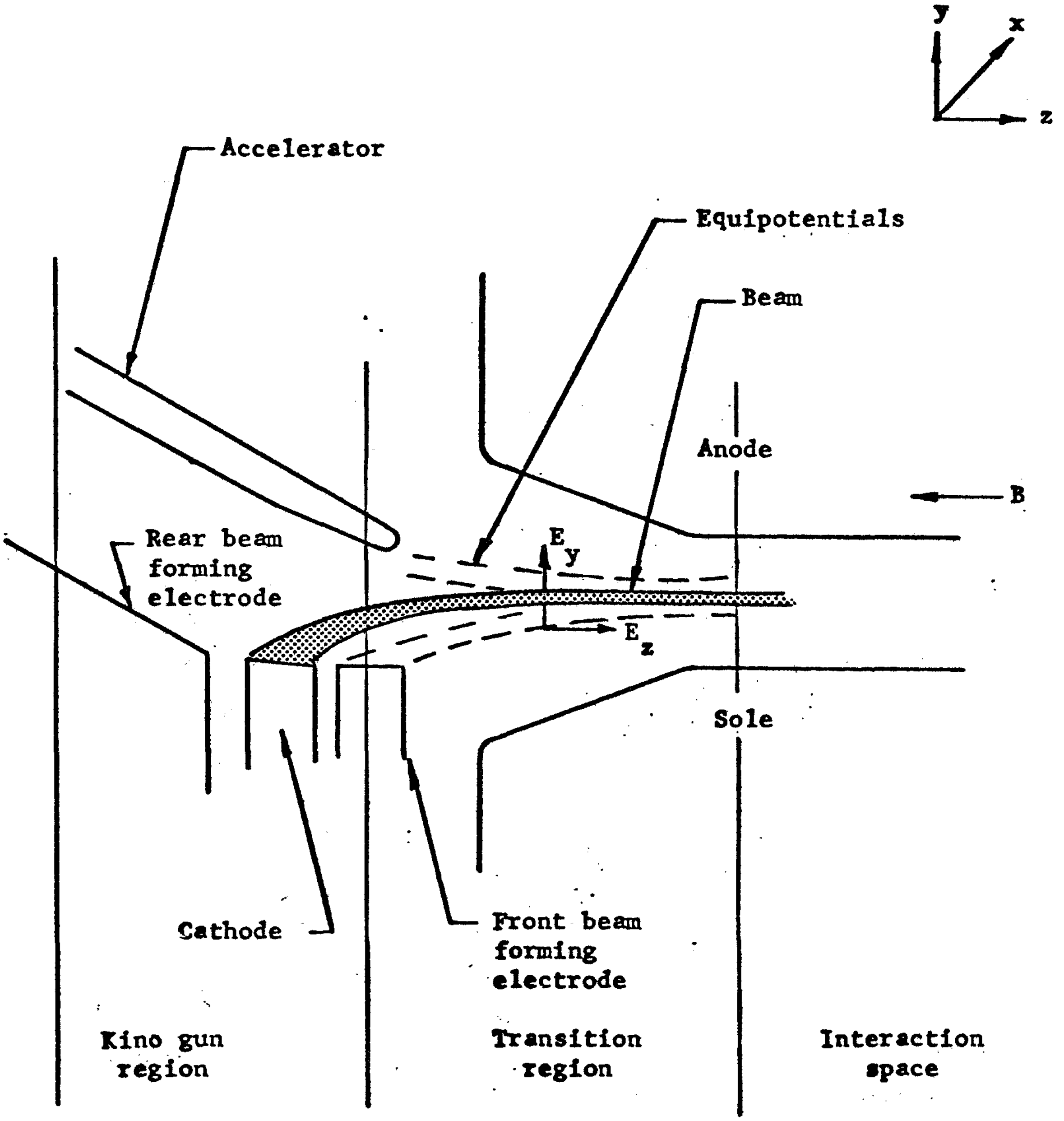

FIGURE 32 SKETCH OF THE AXIAL INJECTION GUN

Slightly accelerating value of E_z in transition region is used to adjust axial drift velocity. At the same time E_y is increased gradually to speed the beam up in the x direction.

follows the ideal trajectories calculated by Kino and Taylor. Electrode shapes in this region are set up in accordance with the Kino-Taylor theory (Ref. 8) to insure this type of space charge flow. If we were to attempt to continue the Kino region until the x velocity in Figure 31 was equal to the circuit synchronous velocity, the Kino region would become very long and the z velocity would become very large. We thus terminate the Kino region after the beam is well formed and at a point where the x and z velocities are relatively low. The beam then enters a transition region. In this region the electric field is increased so as to increase the x velocity in Figure 32 while at the same time the shape of the equipotentials is adjusted to provide either a slight retarding field in the z direction or at least no substantial acceleration of the beam in this direction. The shape of some typical equipotentials is sketched in Figure 32. The third region of the gun is the interaction space proper where the y directed electric field is constant and there is no z directed electric field. In the case of the conventional injected beam tube, the requirements for smooth laminar flow (Brillouin flow) lead to a certain velocity slip across the beam, with this slip being a function of the beam current, the synchronous voltage, the beam width (h in Figure 31), and the magnetic field. In the axial injection case we have derived a similar expression which gives the velocity slip in both the x and z directions. We will now discuss each of these regions of the gun separately.

5.2.2 The Kino Region

The equations for space charge flow in the Kino region are simplest if the coordinates are taken as shown in Figure 33- i.e., with one of the axes parallel to the cathode surface. When the cathode is tilted with respect to the magnetic field, this means that there will be a component of magnetic field perpendicular to the

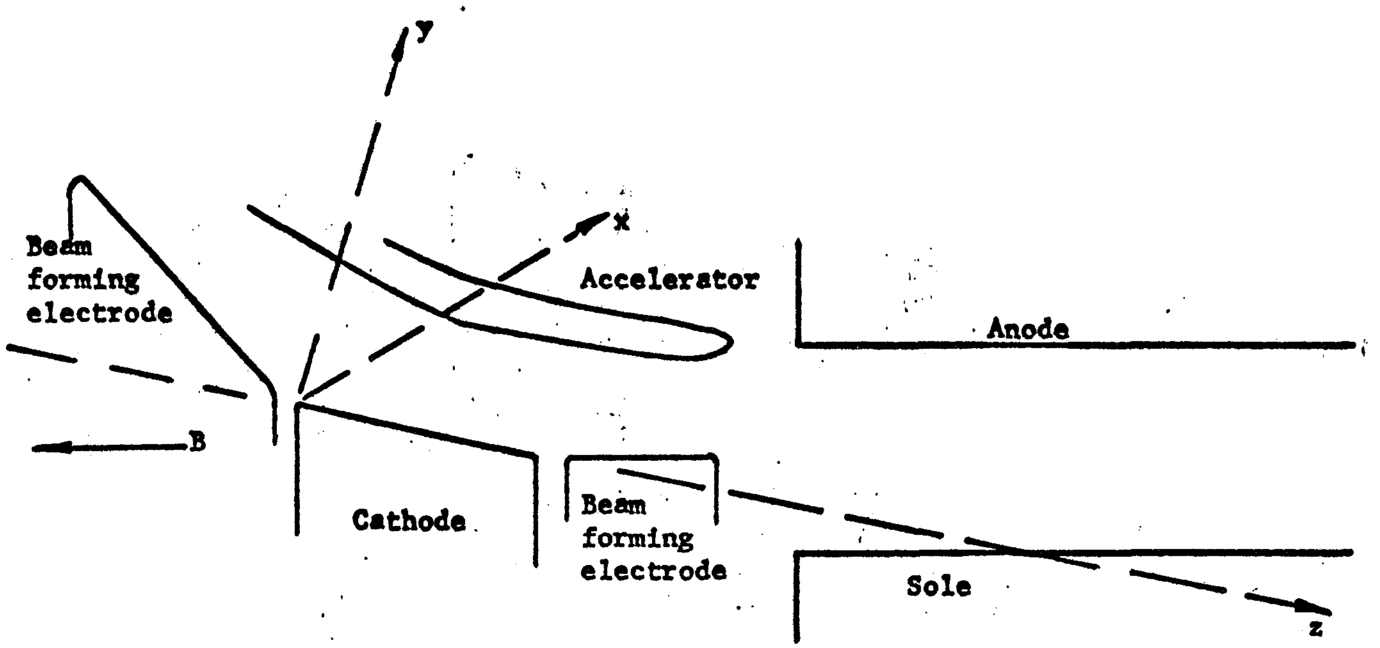

FIGURE 33 COORDINATES USED IN THE KINO-TAYLOR ANALYSIS

The z axis is along the cathode and the x axis is perpendicular to paper.

cathode as well as one parallel to the cathode surface. This is the coordinate system that Kino and Taylor used in their analysis. It is different from the system used in Figure 32, where one of the coordinate axes (the z axis) is taken parallel to the magnetic field. It will later be found that this simplifies the analysis of the transition region. An appropriate transformation of coordinates must be made as we go from one region to the other. The original Kino-Taylor equations are given in normalized form. To understand the effect of various gun parameters on the velocities, it is desirable to put these equations back in unnormalized form. The derivation of the equations we have used is given in Appendix IV of Reference 7. The resulting equations for the top and bottom x and z velocities at the end of the Kino region are given by

$$v_{x_+} = \frac{(7.56 \times 10^3)}{B} \left(\frac{I}{L}\right)^{\frac{1}{3}} (\cos \theta)^{\frac{2}{3}} \left(\frac{J_o}{\sin \theta}\right)^{\frac{1}{3}} \left(\frac{z}{z_o}\right)^{\frac{1}{3}} \tag{10}$$

$$v_{x_-} = v_{x_+} \left(1 - \frac{z_o}{z}\right)^{\frac{1}{3}} \tag{11}$$

$$v_{z_+} = (4.45 \times 10^7) \left(\frac{I}{L}\right)^{\frac{2}{3}} (\cos \theta)^{\frac{1}{3}} \left(\frac{J_o}{\sin \theta}\right)^{\frac{-1}{3}} \left(\frac{z}{z_o}\right)^{\frac{2}{3}} \tag{12}$$

$$v_{z_-} = v_{z_+} \left(1 - \frac{z_o}{z}\right)^{\frac{2}{3}} \tag{13}$$

where v_{x_+} and v_{x_-} are the top and bottom x-directed velocities

v_{z_+} and v_{z_-} are the top and bottom z-directed velocities

I is the beam current

J_o is the cathode current density

θ is the cathode tilt angle

L is the cathode length in the x direction

z_o is the cathode length in the z direction

z is the distance along a trajectory assuming the origin at the rear edge of the cathode.

All quantities are in MKS units.

Equations 10-13 are expressed in the Kino coordinates of Figure 32. To convert them to the coordinates of Figure 31, in which the z axis is parallel to the magnetic field, we use the transformation equations as follows:

$$v_x = v_{x_K} \tag{14}$$

$$v_y = v_{y_K} \cos \theta - v_{z_K} \sin \theta \tag{15}$$

$$v_z = v_{z_K} \cos \theta + v_{y_K} \sin \theta \tag{16}$$

where v_x, v_y and v_z are the velocities in the coordinates of Figure 36 in which the z axis is parallel to the magnetie field

v_{x_K}, v_{y_K} and v_{z_K} are the velocities in the Kino coordinates of Figure 33.

θ is the cathode tilt angle.

These equations have been programmed for a time share computer to give us the exit plane conditions at various distances from the end of the cathode. Results of such calculations for the two inch long gun employed in the experimental tube are summarized in Table III. The table shows the conditions at the exit plane. The values of position and velocity obtained for the trajectory at this point can then be employed as input conditions to the digital computer trajectory tracing calculations which are employed to carry the trajectories through the transition region and into the interaction space.

TABLE III

KINO REGION PARAMETERS AT EXIT PLANE 0.025 INCHES (0.0635 CM) FROM EDGE OF CATHODE FACING INTERACTION SPACE - COORDINATES OF FIGURE 28

Cathode current	1.2 amps
Cathode current density	1.94 amps/cm^2
Cathode length	2.0 inches (5.08 cm)
Cathode width (parallel to magnetic field)	0.050 inches (0.0508 cm)

			Units
Magnetic field	2500	3500	gauss
	0.25	0.35	w/m^2
Top trajectory y	.0064	.0034	in.
	.0162	.0087	cm
Bottom trajectory y	.0043	.0022	in.
	.0109	.0056	cm
Top x voltage	128	65	volts
Top y voltage	0.1	.03	volts
Top z voltage	180	179	volts
Bottom x voltage	62	32	volts
Bottom y voltage	0.1	.03	volts
Bottom z voltage	47	47	volts
Top transit angle ($\omega_c t$)	34	47	radians
Bottom transit angle	23	33	radians

Reference to the above equations show the current density and the angle of tilt as a ratio of J_o to sin Θ. The cosine of Θ also enters into the x directed velocity equations but since the angles are ordinarily quite small, the cosine is almost equal to unity. Therefore, to a good approximation current density and cathode angle appear only as a ratio, $J_o/\sin \Theta$. A given set of exit plane velocity conditions may therefore be obtained with different cathode angles and current densities. The current density may be lowered for a given exit velocity condition by using a shallower cathode angle.

Previous experience with Kino guns in O-type tubes shows that the noise level produced by the gun is a function of the angle of the cathode with respect to the magnetic field (Ref. 11, 12). The existence of high noise levels in crossed-field electron guns under certain conditions has been known for a number of years and it has been postulated that the mechanism for this high level or anomalous noise is the result of a potential minimum instability. Recent theoretical studies by Ho and VanDuzer (Ref. 13) appear to have shed a considerable amount of light on the details of this mechanism. Apparently, the tilt of the cathode surface with respect to the magnetic field interferes with the feedback effects which generate the potential minimum instability. The effect of slight tilts of the cathode surface with respect to the magnetic field in reducing the noise by many orders of magnitude has been noted by several experimenters using magnetron injection guns in O-type tubes.

Recently, similar results have been reported by Wadhwa and Sisoda (Ref. 14) when the guns in conventional injected beam tubes are tilted slightly with respect to the magnetic field. Tilt angles as low as a half degree have proven effective in conventional magnetron injection guns. At present the relationship between the gun parameters, tilt angle, and the onset of high level noise is not known. Experience has indicated that 4 degree tilt angle guns are not noisy and there is substantial evidence to indicate that 2 degree tilt angle guns are also satisfactory. For lower tilt angles we run into the possible danger of increasing gun noise and also into practical limitations on our ability to hold the percentage tolerance on the tilt angle within an acceptable range. For these reasons we have concentrated our efforts in the present program on gun tilt angles in the 2 degree to 4 degree range.

5.2.3 The Transition Region

The axial (z component) and longitudinal (x component) velocity of the electrons, as well as the velocity slip in both of these directions, is further modified in the transition region. At one time it was believed that the z directed velocity slip would not be affected by a significant amount in the transition region and that we could simply modify the x velocity component by increasing the electric field while decelerating the z component by a proper shaping of the equipotentials to provide a decelerating z directed force. During this study it was found, however, that the z directed velocity slip is also substantially modified in the transition region.

It is desirable to maintain the axial velocity as small as possible even when a reflecting system is employed to minimize the energy associated with axial velocities which may not be recovered, and if possible to insure that electrons emitted from the input end of the gun do not return to the gun after their initial reflection from the opposite side of the interaction space. That is, we would prefer to obtain the situation sketched in Figure 34a rather than that in Figure 34b. It is not certain just what the effect of trajectories reflected back into the gun would be. Some initial experiments on an S-band Vaxitron beam tester tend to indicate that this situation is tolerable, at least for some fraction of the gun near the output. Until more is known about this, however, it seems to be a desirable

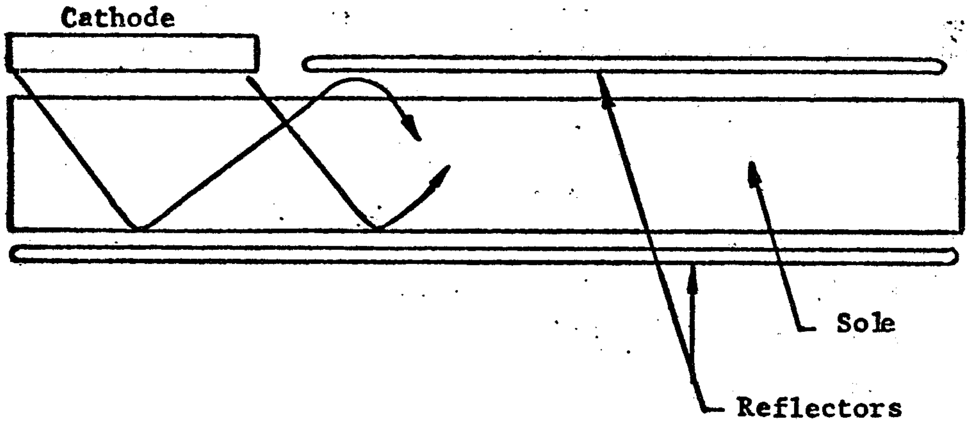

a. Reflected electrons miss gun

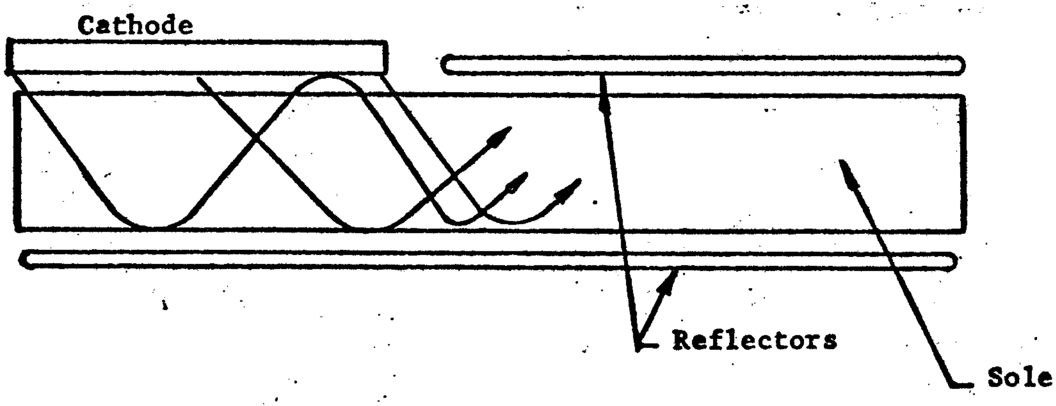

b. Reflected electrons returned to gun

FIGURE 34 SKETCH SHOWING DESIGNS IN WHICH REFLECTED ELECTRONS MISS GUN AND REFLECTED ELECTRONS ARE RETURNED TO GUN

The design (a) avoids possible problems with optics caused by the returning beam. However, design (b) can give lower cathode current density and has been found satisfactory in some preliminary experiments.

procedure to at least minimize the length of the cathode over which reflected electrons return to the gun.

A limitation on the minimum axial velocity of the top beam edge electrons is obtained as a result of the velocity slip in the z direction. Examination of equations 10-13 for the Kino gun region show that at the exit from this region, the electrons at the top edge of the beam have a higher velocity in the z direction than do those at the bottom beam edge. If z directed retarding fields are now applied in the transition region, the z velocity of both the top and bottom edges of the beam is reduced. If the velocity slip is sufficient we eventually reach a condition in which the retarding fields slow the bottom edge of the beam down to zero and turn the bottom edge of the beam back into the gun. At this point the top edge electrons still have a finite z directed velocity. Experimentally it has been found that axial injection guns have a characteristic as sketched in Figure 35 as a function of the sole to cathode voltage. At the knee of this curve, the bottom edge electrons are just barely turned around. The axial velocity of the top edge electrons remains finite at this point. If we want to avoid trapping of current in the gun which appears to be necessary from the standpoint of minimizing noise and cathode back bombardment, the minimum axial velocity of the top edge electrons is therefore fixed by the axial velocity slip in the beam.

Not only is there an axial velocity slip in the beam at the exit of the Kino region, but this velocity slip is further increased in the transition region. The reason for this can be seen by examining the equipotentials in Figure 32. It can be seen that there is a variation in the z directed electric field force as a function of the y coordinate so that if the electric field is increased in the transition region, there will be a difference in the z directed forces applied on the top and bottom edges of the beam in such a direction as to increase the z directed slip. At one time it was thought that

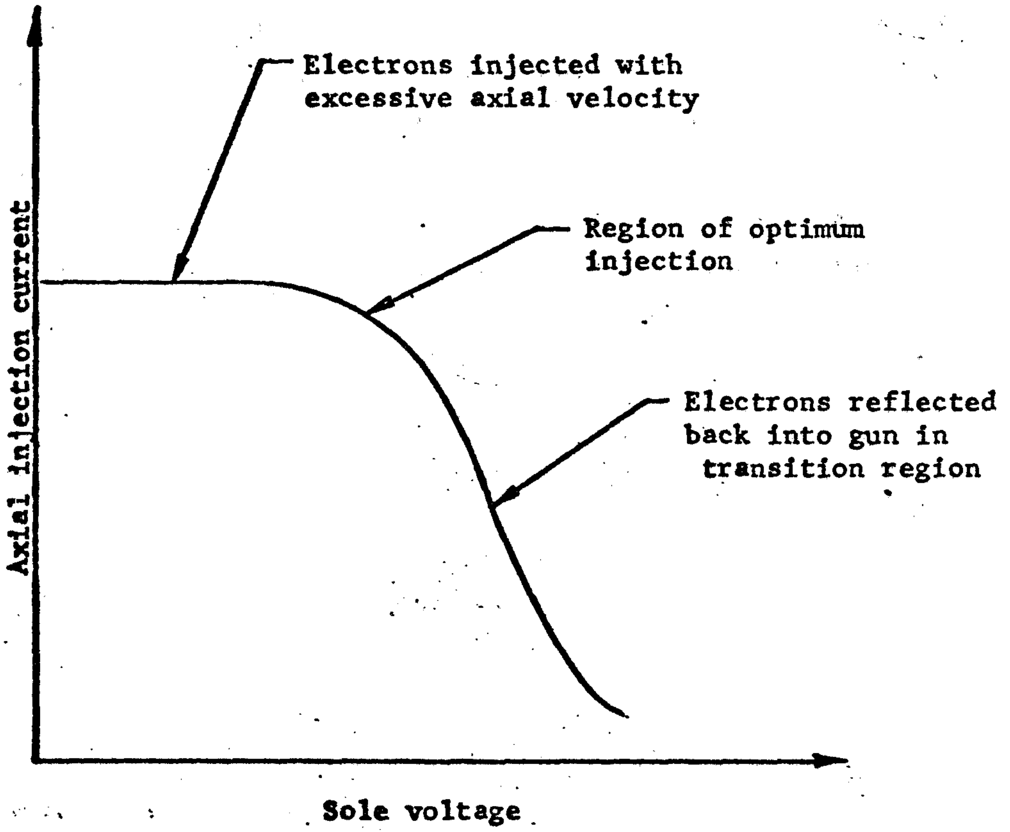

FIGURE 35 TYPICAL DEPENDENCE OF AXIALLY INJECTED CURRENT ON SOLE TO CATHODE VOLTAGE

this effect would be small because the beam is quite thin relative to the interaction space. However, the voltage gradients across the thickness of the beam are substantial, resulting in a total voltage difference between the top and the bottom edge of the beam which is of a significant magnitude. If a reasonable fraction of this total voltage difference is associated with differences in the z velocities, the effect of the field gradients in the transition region will be significant even though the beam is quite thin. Realization of this led us to a more detailed study of the gradients in this region. For this purpose we defined voltages associated with the x, y and z velocities as follows:

$$V_x = \frac{v_x^2}{2\eta} \qquad (17)$$

$$V_y = \frac{v_y^2}{2\eta} \qquad (18)$$

$$V_z = \frac{v_z^2}{2\eta} \qquad (19)$$

$$V = V_x + V_y + V_z \qquad (20)$$

where v_x, v_y and v_z are the x, y, and z directed velocities respectively

η is the charge to mass ratio for an electron

V is the total voltage with respect to the cathode through which an electron has fallen

It should be remembered that the voltages defined above are not vectors but are associated with the individual velocity components. Thus, the three voltages V_x, V_y, and V_z add in a scaler manner to give the total voltage V. In terms of these voltages we were able to develop an approximate expression for the effect of the fields in the transition region on the axial voltage V. This derivation is carried out in Appendix V of Reference 7 for a space charge free beam. The resulting relationship for the axial voltage is given by:

$$\Delta V_{zI} - \Delta V_{zK} = \Delta E_y t \tag{21}$$

where ΔV_{zI} is the difference in top and bottom z voltages in the interaction space

ΔV_{zK} is the difference in top and bottom z voltages at the exit of the Kino region

ΔE_y is the difference in the y directed dc electric field between the interaction space and the Kino gun exit

t is the average beam thickness in the transition region

Equation (21) says that the axial voltage difference between the top and bottom of the beam is increased when the y directed electric field is increased in the transition region to accelerate the beam in the x direction. The equation does not tell us anything specific about either the top or bottom edge axial voltage but only something about the difference between these voltages at the end of the Kino region and in the interaction space. As will be shown in the next section, equation (21) can be generalized to take space charge into account and at the same time can be made exact for a laminar beam.

A digital computer simulation has been employed in practice to design the transition region and to carry the trajectory calculations through the transition region into the main interaction space. Before discussing this computation, however, it is useful to discuss the Brillouin conditions which must obtain in the main interaction space.

5.2.4 The Interaction Space - Conditions for Laminar Flow

In a conventional injected beam system, conditions for laminar flow with no cycloiding can be derived. The system studied is shown in Figure 36. For laminar non-cycloiding flow to occur, there must be an exact force balance on all of the electrons. This results in crossed-field Brillouin flow. It can be shown that this requires a variation in x directed velocity across the beam which may be related to the magnetic field, B by:

$$\frac{\partial v_x}{\partial y} = \omega_c \tag{22}$$

where $\omega_c = \eta B$, and η is the charge to mass ratio for an electron.

The Brillouin thickness of the beam, t_o, is then related to the total velocity slip by:

$$\Delta v_x = \omega_c t_o$$

At the same time, the charge density throughout the beam is constant and is given by:

$$\rho = \eta \; {}_o B^2 \tag{23}$$

where ρ is the charge density

ϵ_o is the permittivity of free space

Setting the dc beam current equal to:

$$I = \rho v_x A \tag{24}$$

where A is the cross-sectional area of the beam, we can obtain an expression relating the velocity slip to the dc parameters of the beam. This is done by integrating the above equation across the thickness of the beam and expressing the velocity at the midplane

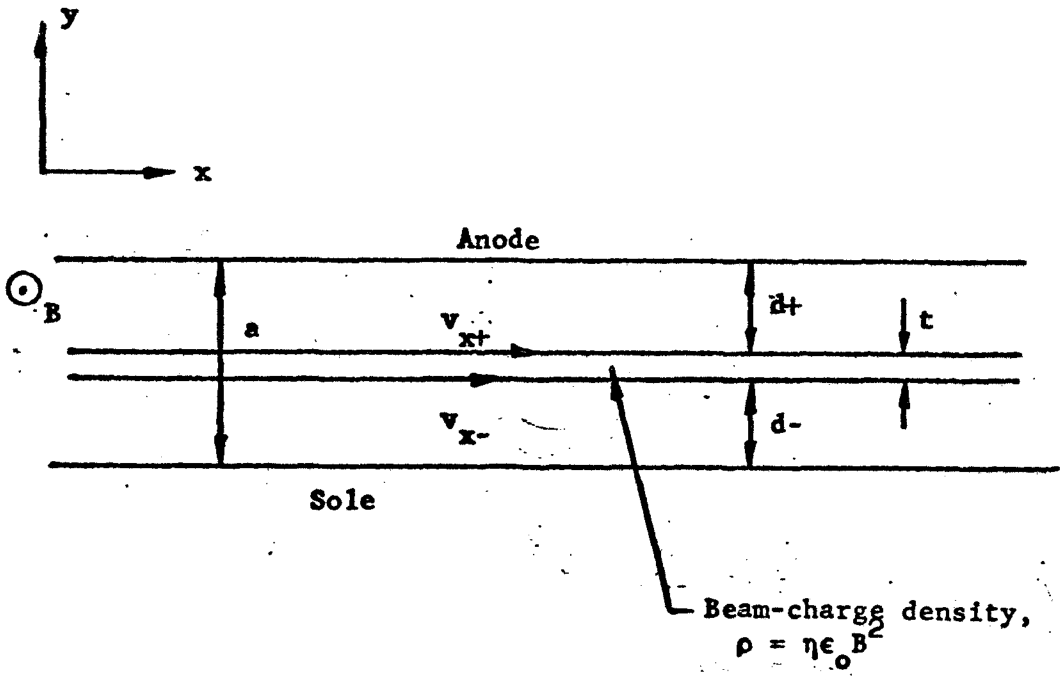

FIGURE 36 SKETCH OF COORDINATES AND DIMENSIONS USED IN STUDY OF A CONVENTIONAL INJECTED BEAM

The velocity, v_o, is the beam mid-plane velocity which is made synchronous with the circuit wave velocity.

of the beam in terms of a voltage which is normally made synchronous with the circuit wave velocity. We thus have an expression between current, magnetic field, synchronous voltage, beam width, and velocity slip given by:

$$I = 2\epsilon_o \eta_o h V_o B\left(\frac{\Delta v}{v_o}\right) \qquad (25)$$

where h is the beam width

v_o is the midplane x velocity

Δv is the velocity difference between the top and bottom edge of the beam

If we know I, h, V_o, and B, we can thus find the velocity slip from equation (25) and the beam thickness from equation (22).

The above equations do not hold in the axial injection case because there are additional velocity components in the z direction. We have, therefore, rederived the conditions for laminar flow for the axial injection case. Before turning to a consideration of these results, it is of interest to examine what happens in the space charge free case. We will need these results later when discussing some of our space charge free trajectory tracing studies using the digital computer. In the absence of space charge, the conventional injected beam sketched in Figure 35 travels in the x direction with a velocity equal to the ratio of the dc electric to the magnetic field. The case of the axial injection beam without space charge is considered in Appendix VI of Reference 7. The system studied there appears similar to that sketched in Figure 36 in the x-y plane and appears as sketched in Figure 37 in the y-z plane. The results show that the x directed velocity is given by the E/B ratio just as is the case in the conventional injected beam without axial velocities. However, in the axial injection case, there is an additional velocity slip in the z direction which is given by:

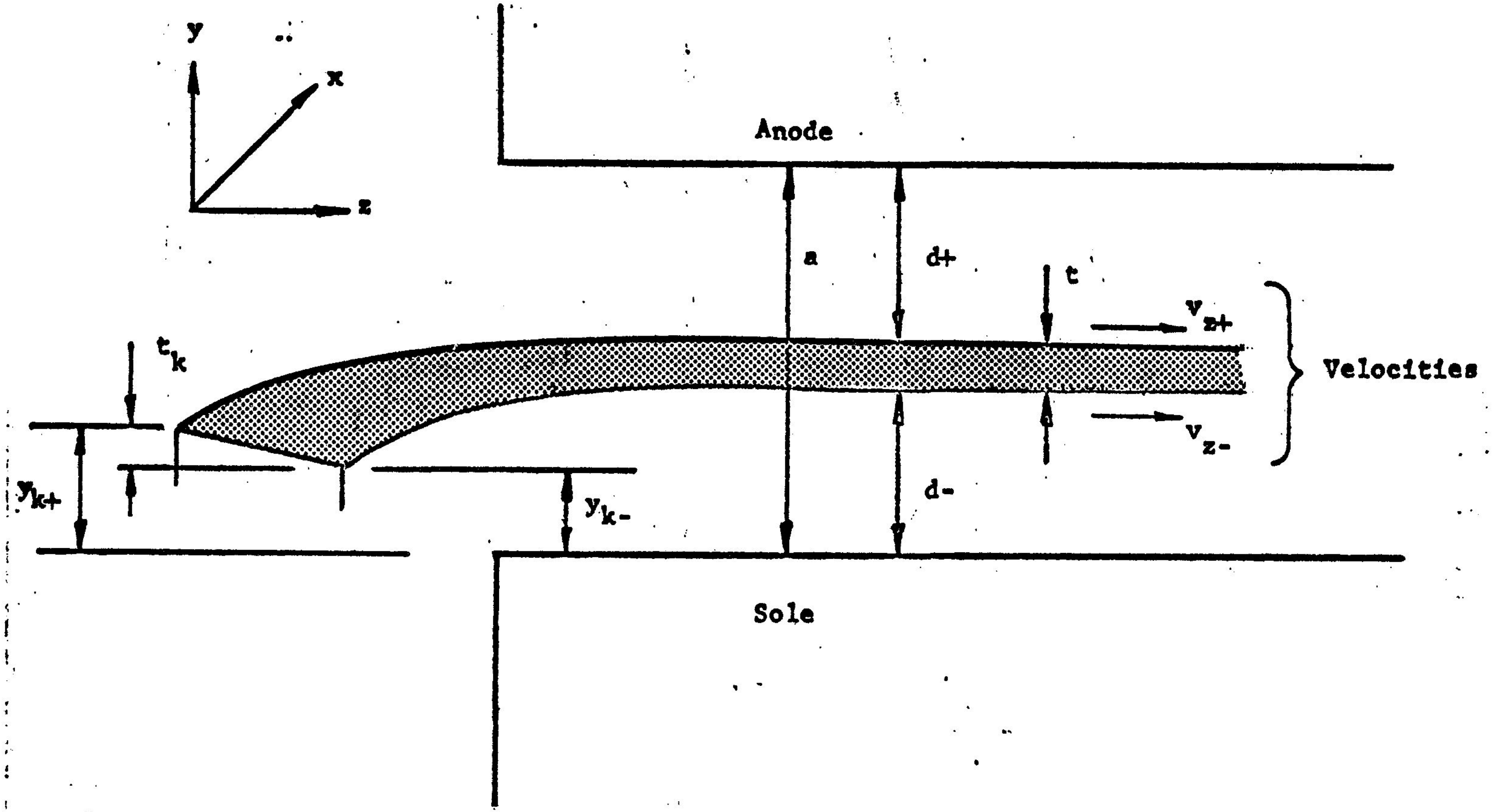

FIGURE 37 SKETCH OF COORDINATES AND DIMENSIONS USED IN STUDY OF AXIAL INJECTION

$$\Delta V_z = E_y t_k \tag{26}$$

where ΔV_z is the difference in the voltage associated with the z velocities at the top and bottom of the beam

E_y is the dc electric field in the interaction space

t_k is the vertical projection of the cathode as shown in Figure 36.

The difference in the voltage associated with the z directed velocity is thus shown to be related to the electric field strength in the interaction space and to the vertical projection of the cathode, t_k. This result was rather surprising to us when first derived since it relates a property of the beam in the interaction space (the axial velocity slip) to a particular property of the cathode (its vertical projection), without regard to the nature of the gun fields and the transition region between the cathode and the interaction space. The restrictions under which this equation holds are simply that the beam be laminar.

In Appendix VII of Reference 7 we have expanded the derivation to include the effects of space charge. The results are a composite of the axial injection properties derived in Appendix VI of Reference 4 and the properties of the conventional injected beam Brillouin flow. Specifically, we find the following.

1. The beam thickness is increased by t_k over the Brillouin beam thickness for a conventional injected beam. The total beam thickness is thus given by $(t_o + t_k)$ where t_o is obtained from equations (25) and (23).
2. The x directed velocity slip is related to the beam parameters just as is the case for a conventional injected beam and may thus be calculated from equation (26).
3. The axial velocity slip is given by the same expression as applies for the axial injection system in the absence of space

charge - i.e., by equation (26). The only modification here is that the value of E_y to be employed is now that at the center layer of the beam. Again we see that the beam thickness and the axial velocities are related to the vertical projection of the cathode. These conclusions are restricted to the case of laminar flow in the beam. The exact expression for the change in V_z in the transition region may now be seen to be the derivative of the expression in equation (26) which holds for the general case, and is thus expression (21) with the vertical projection of the cathode, t_k, used in place of t.

These expressions show that there is a fundamental limit on how small we can make the axial velocity slip for a given interaction space design and that this limit depends simply on the vertical projection of the cathode.

Another important equation used in studying the axial injection system may be derived by integrating the equation for the x directed force. The fact that E_x is zero for the axial injection system permits this integration to be carried out directly. This situation is analogous to the derivation of Busch's theorem in θ-type beams and we have indeed called the result Busch's theorem for the axial injection beam. This integration is carried out in Appendix VIII of Reference 4. The result is:

$$v_x = \eta B \, (y - y_k) \qquad (27)$$

where y_k is the y coordinate value at which a trajectory leaves the cathode.

This equation relates the position of any trajectory in the interaction space to the magnetic field and to the cathode position. The desired beam position in the interaction space is normally determined by the RF design. Equation (27) is then employed to determine the position of the cathode with respect to the anode and the sole. As shown in Appendix VIII of Reference 7, this expression can then be employed to derive an expression for the sole voltage corresponding to a given value of the axial velocity of the bottom beam edge. This equation is:

$$V_s = (v_{x_-})\, B \left(y_{k_-} + \frac{v_{x_-}}{\eta B}\right) - (V_{x_-} + V_{z_-}) \qquad (28)$$

where V_s is the sole to cathode voltage

y_{k_-} is the distance from the sole to the edge of the cathode facing the interaction space

The remainder of the variables are as defined above.

The sole voltage for which the bottom edge of the beam is just turned around and we reach the knee of the curve sketched in Figure 29 is obtained by solving equation (28) with V_{z_-} set equal to zero. When using the above equations, the x velocities may be obtained from the assumed synchronous velocity and the velocity slip across the beam as expressed by equation (25).

A complete set of equations to describe the dc beam in the interaction space has now been derived. These equations are summarized in Figure 38. The equations are written so that current, synchronous voltage, magnetic field, beam width, anode to sole spacing, cathode spacing, the vertical projection of the cathode are assumed as independent variables. The equations then calculate the location of the beam in the interaction space, the beam thickness, the x and z velocities at the top and the bottom of the beam, and the cathode and sole voltage. These equations have been programmed for the time share computer and typical results will be presented in a later section.

5.2.5 Digital Computer Studies of Axial Injection Flow

While the equations developed in the above sections tell us some interesting general properties about beams, they are restricted to laminar beams and do not consider the effects of trajectory crossings in the beam. They also do not tell us anything about how to design the transition region to minimize cycloiding of the beam

Velocity slip $\frac{\Delta v}{v} = \frac{1}{2\eta\epsilon_o V_o B}$

Circuit synchronous velocity $v_o = \sqrt{2\eta V_o}$

$$v_{x_+} = v_o\left(1 + \frac{\Delta v}{v}\right) \qquad v_{x_-} = v_o\left(1 - \frac{\Delta v}{v}\right)$$

$$V_{x_+} = \frac{v_{x_+}^2}{2\eta} \qquad V_{x_-} = \frac{v_{x_-}^2}{2\eta}$$

$$t = \frac{v_{x_+} - v_{x_-}}{\eta B} + t_k$$

$$E_o = v_o B$$

$$V_{z_+} = V_{z_-} + E_o t_k$$

$$d_- = \frac{v_{x_-}}{\eta B} + y_k \qquad d_+ = a - d_- - t$$

Cathode to anode voltage $V_{ka} = v_{x_+} d_+ B + V_{x_+} + V_{z_+}$

Sole to cathode voltage $V_{sk} = v_{x_-} d_- B - V_{x_-} - V_{z_-}$

Sole to anode voltage $V_{sa} = V_{sk} + V_{ka}$

FIGURE 38 dc BEAM EQUATIONS SUMMARIZED
(Quantities as defined in Figures 36 and 37)

in the interaction space. Thus, for the design of axial injection guns, we turn to the use of digital computer techniques. The computer program used in these studies traces axial injection trajectories in the absence of space charge. A program including space charge would, of course, be more desirable and has been under preparation as part of this study. However, at the time of writing this report, it was not ready for use. We can, however, determine a great deal of useful information from intelligent use of the space charge free trajectory tracing program.

The computer program derived for axial injection trajectory tracing assumes the cross section of the system to remain constant as a function of the x direction. LaPlace's equation is thus solved in two-dimensional coordinates - the y and z dimensions. This is done by relaxation techniques using a 100 by 240 matrix (corresponding to y and z dimensions respectively). Electrode boundaries and voltages, along with initial trajectory positions and velocities are read into the program. LaPlace's equation is then solved to find the voltages at all of the matrix points. Trajectories are then traced through the system using three dimensional force equations and the trajectory information is printed out. A second matrix is used in the program to store the "error voltages" which are related to the voltage differences at each matrix point on successive iterations through the matrix in the solution of LaPlace's equation. This error voltage matrix may be employed to determine regions in the matrix where convergence is poor. Sometimes, convergence may be speeded up by making appropriate initial estimates of the voltages in the system and feeding them into the matrix. In versions of the program employing space charge, the second matrix is also used to store space charge densities. The full program with the two matricies requires about 400,000 bytes of storage on an IBM System 360 computer. It solves most systems we have investigated in a few minutes of running time on an IBM 360/65. Trajectory information as well as the two voltage matrices are printed out by the computer. The technique for the solution of LaPlace's equation employed is taken from previous work by Boers (Ref. 15).

Some particular attention to initial conditions for the trajectories is required when we attempt to obtain useful information employing the space charge free trajectory tracing program. We are attempting to use information available on the trajectories calculated from the Kino conditions at the exit of the interaction space as input conditions to the computer program. We then trace trajectories through the transition region and into the main interaction space. If we use the exact Kino exit plane parameters as input velocities to the space charge free trajectory tracing routine, we would encounter some problems. In the Kino gun region, the forces are balanced so that the trajectories are not cycloiding in the x direction. If we used the same velocities without space charge, the forces would not be properly balanced and cycloiding of the trajectories would occur. To obtain a better approximation to the axial situation using the space charge free program, we employ some of the concepts developed in the above section for the laminar beam. We have shown in Section 5.2.4 that the axial velocity slip in the beam is not affected by the presence of space charge and depends only on the vertical projection of the cathode. Therefore, in the space charge free simulations, we use the z directed velocities for the trajectories which are determined from the Kino equations (including rotation of the coordinates at the exit of the Kino gun region). For the x directed velocities, we then employ the E/B velocity using the actual electrode spacings and voltages. From the z and x velocities (y velocity is ordinarily negligible), we calculate the potential for each trajectory and reposition the starting point of the trajectory for the space charge free simulation at the correct potential. Forces in the x direction are now balanced and input velocities in the z direction are the same as would be obtained employing space charge.

In our initial attempts to employ the program for the design of X-band guns, we ran into effects which were originally not anticipated. It appeared that our beam was being trapped in the gun even though equation (28) indicated that the beam should be able to get into the interaction space and the axial velocity of the bottom beam edge should have been larger than zero by a comfortable margin. A more detailed analysis of the voltage matrix printed out by the computer showed that the reason this was occurring was that a potential barrier existed between the exit of the gun and the interaction space, and that electrons were reflected into the gun at this barrier. Equation (28) gives information about the velocities in the interaction space without detailed consideration of the fields between the cathode and the interaction space. Implicit in the use of the equation, however, is the assumption that the trajectories are capable of getting into the interaction space - i.e., that there are no potential barriers between the cathode and the interaction space which return the electrons to the cathode region. It thus became clear that another use of the computer program would have to be the elimination of such potential barriers. To investigate this effect, we added a feature to the program through which the z component of the electric field is integrated to give the voltage V_z associated with the z velocity. This information is printed out for each trajectory point. When this was done, it was found that it was possible to obtain a relationship between V_z and z as shown in Figure 39. The curve is sketched here for several values of sole voltage. Because of a potential barrier between the Kino gun exit region and the interaction space, there is a minimum in the V_z voltage. When, through adjustment of this sole to cathode voltage, this minimum

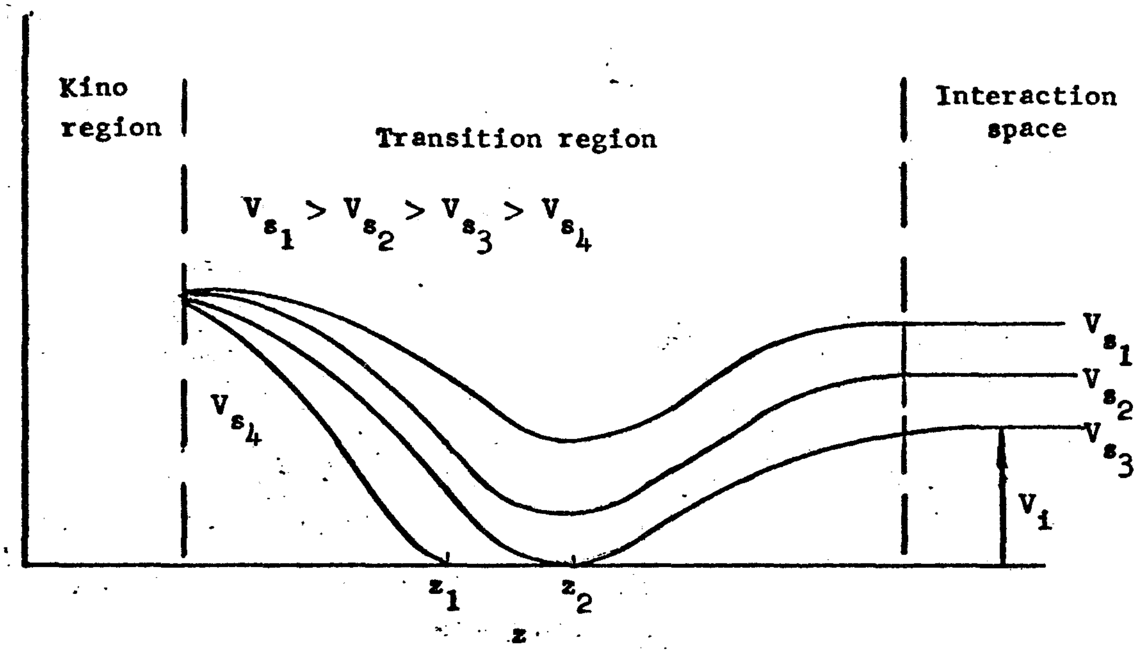

FIGURE 39 SKETCH OF V_z AS A FUNCTION OF z FOR FOUR VALUES OF SOLE TO CATHODE VOLTAGE.

For the sole to cathode voltage, V_{s_4}, the electrons are turned around at z_1. For a voltage of V_{s_2}, the trajectories are just able to get past the potential minimum at z_2 and enter the interaction space. Between z_2 and the interaction space, they are accelerated in the z direction through a potential, V_i. As the sole voltage is decreased the axial velocity of the first electrons permitted to enter the interaction space is thus V_i.

is made tangent with zero voltage, the bottom edge trajectories are turned around and reflected into the gun. As the sole voltage is made a little less negative so that the trajectories are not turned around, the axial velocity in the interaction space suddenly jumps to a finite value indicated by V_i in Figure 39. To make equation (28) valid, it is necessary to eliminate the minimum curves such as shown in Figure 38. This must be done through trial and error using the computer program to evaluate various trial designs.

5.2.6 The Final Gun Design

Table III summarizes the Kino region parameters of the gun design. Table IV summarizes the interaction region parameters. Figure 40 shows the electrode cross-section in the gun and through the transition region into the interaction space. The transition region has been designed by successive approximations using the digital computer and the axial injection trajectory tracing computer program. As may be seen in Figure 40, the final design incorporates a taper in the anode to sole spacing in the transition region between the Kino gun and the interaction space. This taper gradually increases the y-directed electric field strength and thus the electron velocity in the x direction (direction of wave propagation). As a result of the taper, the trajectory enters the interaction space smoothly and with a minimum of cycloiding. The ratio of the maximum voltage of the top of a cycloid to the average voltage of the electron is 1.10. This is the K factor of equation (5) which enters into the efficiency calculation. Without the taper this ratio would have been at least 1.5.

Figure 41 shows the voltage V_z discussed in the previous section as a function of z. It is seen that the curve is smooth and has only a small dip between the gun and the interaction space. This means that there are no significant potential traps between

TABLE IV

INTERACTION REGION PARAMETERS

Cathode current	1.25 amps
Synchronous voltage	1240 volts
Beam width (parallel to B)	0.540 inc. (1.37 cm)
Anode to sole spacing	0.108 in. 0.274 cm)
Distance y_k (see Figure 28)	0.036 in. (0.915 cm)
Distance t_k (see Figure 28)	0.0036 in. (0.0915 cm)
Bottom Z voltage (calculations give sole voltage, which yields this bottom Z voltage)	200 volts

B		Cathode Voltage (volts)	Sole Voltage (volts)	Top Z Voltage (volts)	Fractional X Velocity Slip	d_+ (Figure 28)		t (Figure 28)	
Gauss	w/m^2					ins.	cm	ins.	cm
2500	.25	8817	14292	677	.094	.0488	.124	.0054	.0137
3000	.30	10747	17196	772	.079	.0522	.133	.0048	.0122
3500	.35	12671	20088	868	.067	.0549	.139	.0045	.0114

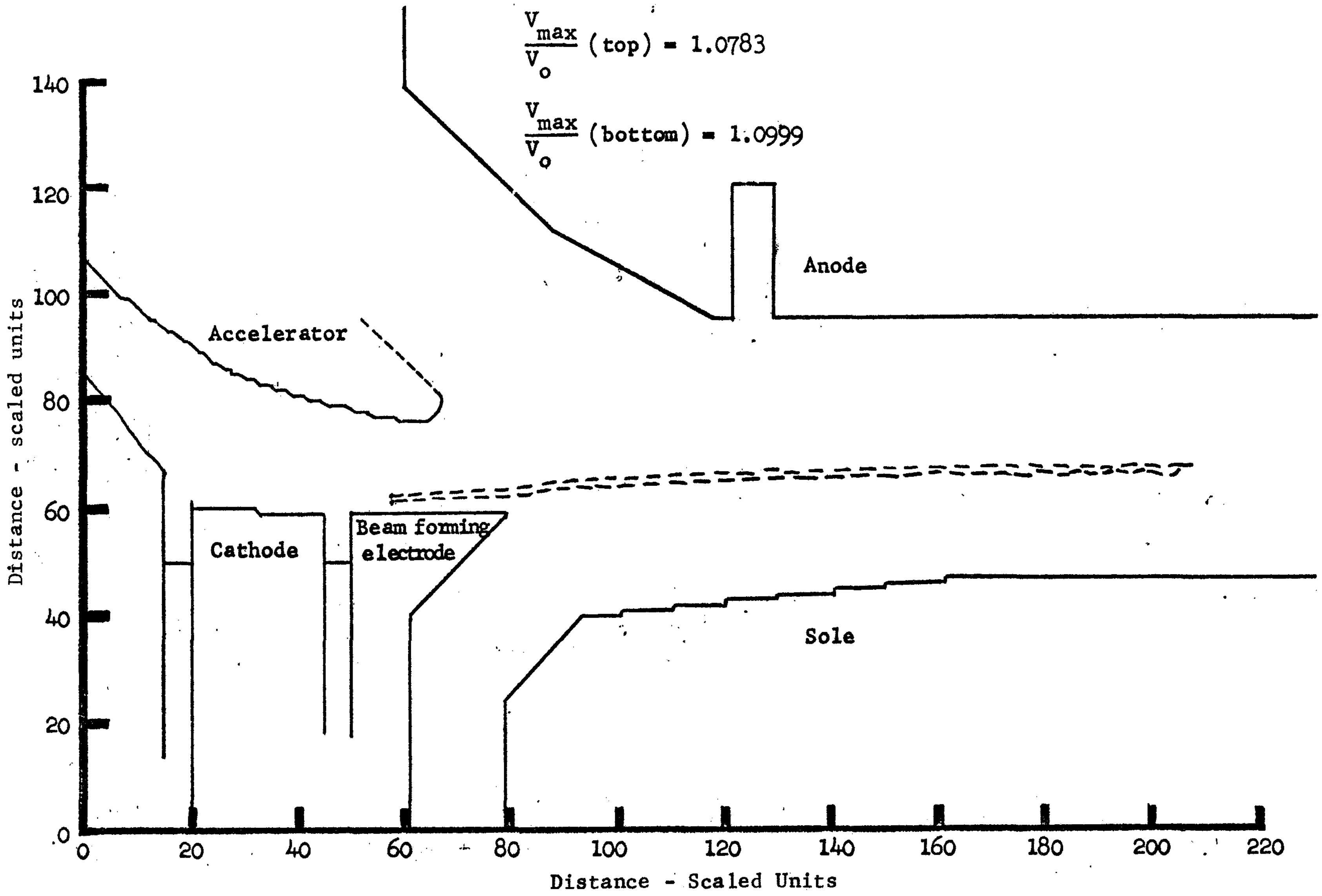

FIGURE 40 GUN LAYOUT FOR COMPUTER SOLUTION SHOWING SPACE CHARGE FREE TRAJECTORIES

The distance scales are in scaled units employed in the computer simulation. One scaled unit = 2×10^{-3} in. (5.08×10^{-3} in.)

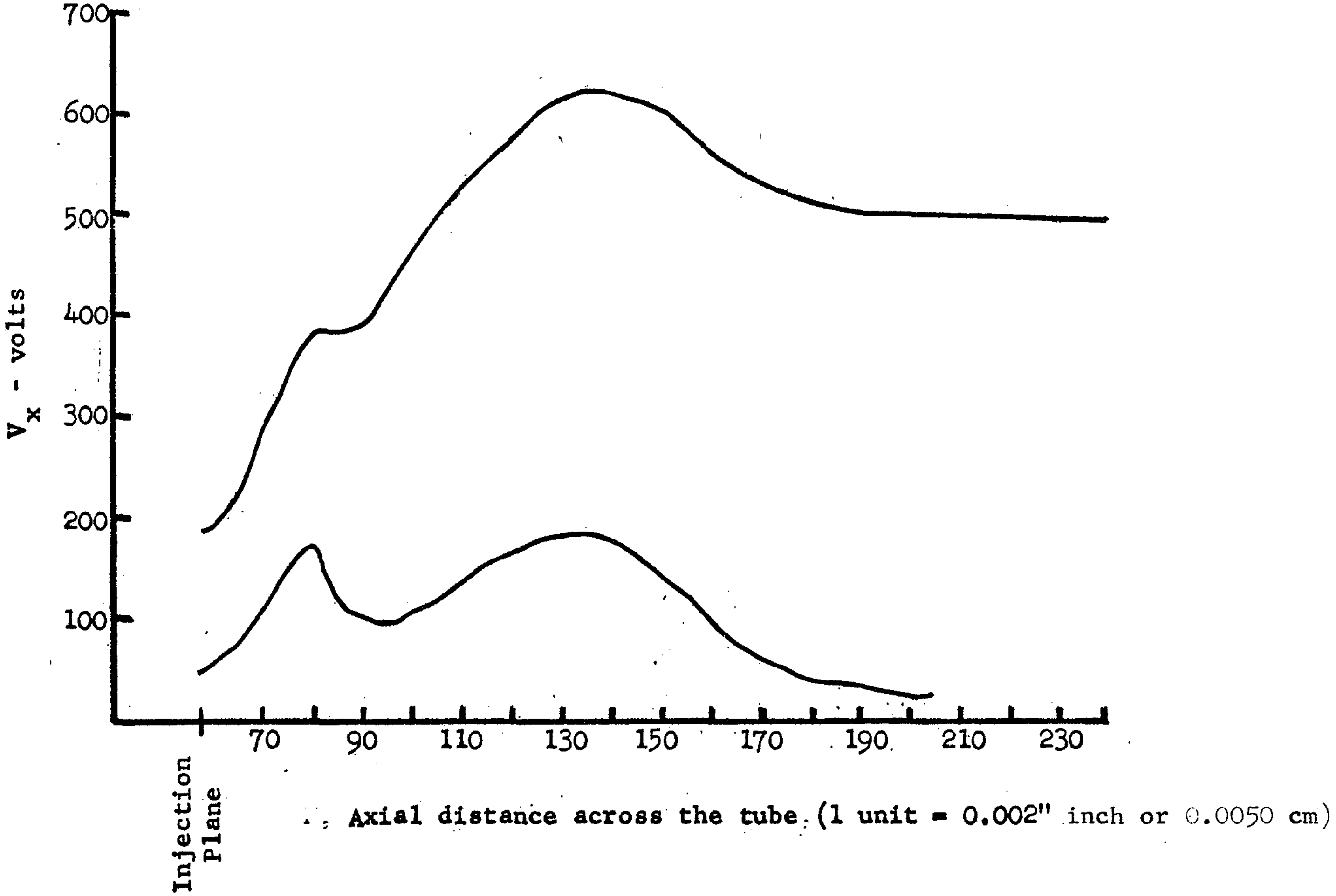

FIGURE 41 VOLTAGE EQUIVALENT OF AXIAL VELOCITIES FOR TOP AND BOTTOM BEAM TRAJECTORIES COMPUTED FOR THE DESIGN OF FIGURE 40.

the gun and the interaction space and the equations of section 5.2.4 are valid. A number of iterations were needed using the digital computer to reach this point. The shape of the transition region taper is not critical with respect to minimizing the cycloiding but it is quite critical with respect to the avoidance of potential traps in the V_z versus z curve.

Table V gives a summary of the results obtained from the gun trajectory calculation.

A similar gun but without the taper has been used successfully on other programs in operating tubes. Figure 42 shows the trajectories in this case. The beam cycloids with a ratio of maximum to average energy of about 1.5. because of the more abrupt injection into the interaction space. With the V/V_o ratio employed the cycloiding would reduce the efficiency by about five percentage points.

5.3 The Reflector Design

Figure 43 shows the shape of a typical reflector such as was employed on this program. The reflector is essentially an end hat physically connected to the sole. Equipotentials in the vicinity of the reflector are sketched in Figure 43. It can be seen that the electric field in the y direction in Figure 43 is different in the reflector region than it is in the main interaction space. Typical electron trajectories are also sketched in Figure 43. These were obtained using the digital computer program for axial injection flow.

Considerable thought has been given to the design of these reflector electrodes. Analysis of previous side reflector designs using the computer program has uncovered two possible problems. First a side reflector can introduce unwanted electron cycloiding and second after reflection an electron can be advanced or retarded in phase relative to the RF wave. The phase shift occurs because in the process of being reflected an electron spends some time in a

TABLE V

SUMMARY OF RESULTS OF TRAJECTORY TRACING CALCULATIONS FOR S-BAND GUN OF FIGURE 40

Values in Interaction Space

Cathode to sole voltage	-5232 volts
Cathode to anode voltage	8769 volts
V_{max}/V_o - top trajectory	1.08
V_{max}/V_o - bottom trajectory	1.10
V_z (top)	784 volts
V_z (bottom)	330 volts
ΔV_z	454 volts

E_y = 130 volts/mil (51,000 volts/cm)

t_k = 0.0036 in. (0.0915 cm)

$\Delta V_z = E_y t_k$ from laminar beam theory = 466 volts

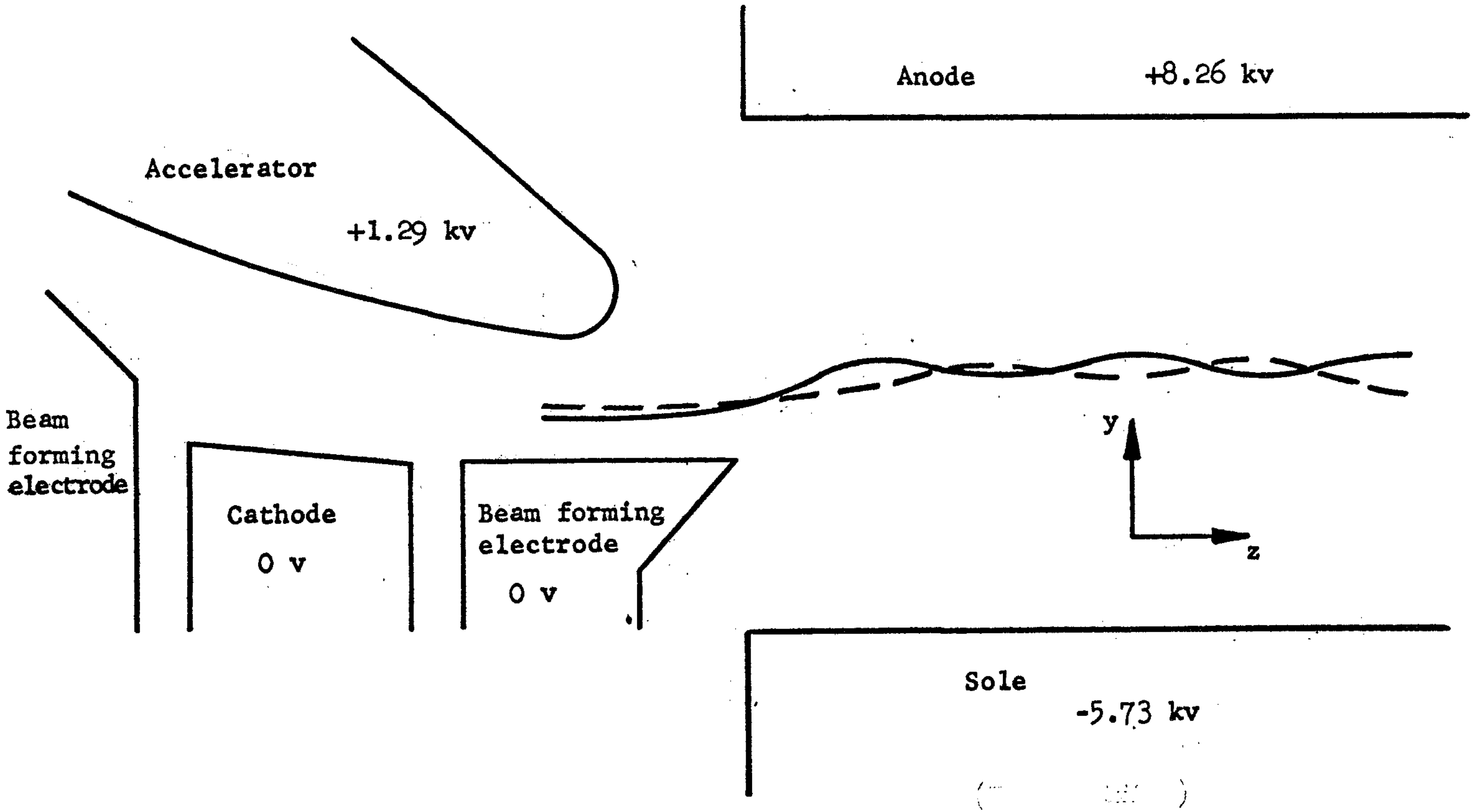

FIGURE 42 CALCULATED TRAJECTORIES IN y-z PLANE FOR S-BAND AXIAL INJECTION GUN WITHOUT TAPERED TRANSITION REGION

The ratio of the maximum energy on a cycloid to the average energy for this gun is about 1.5.

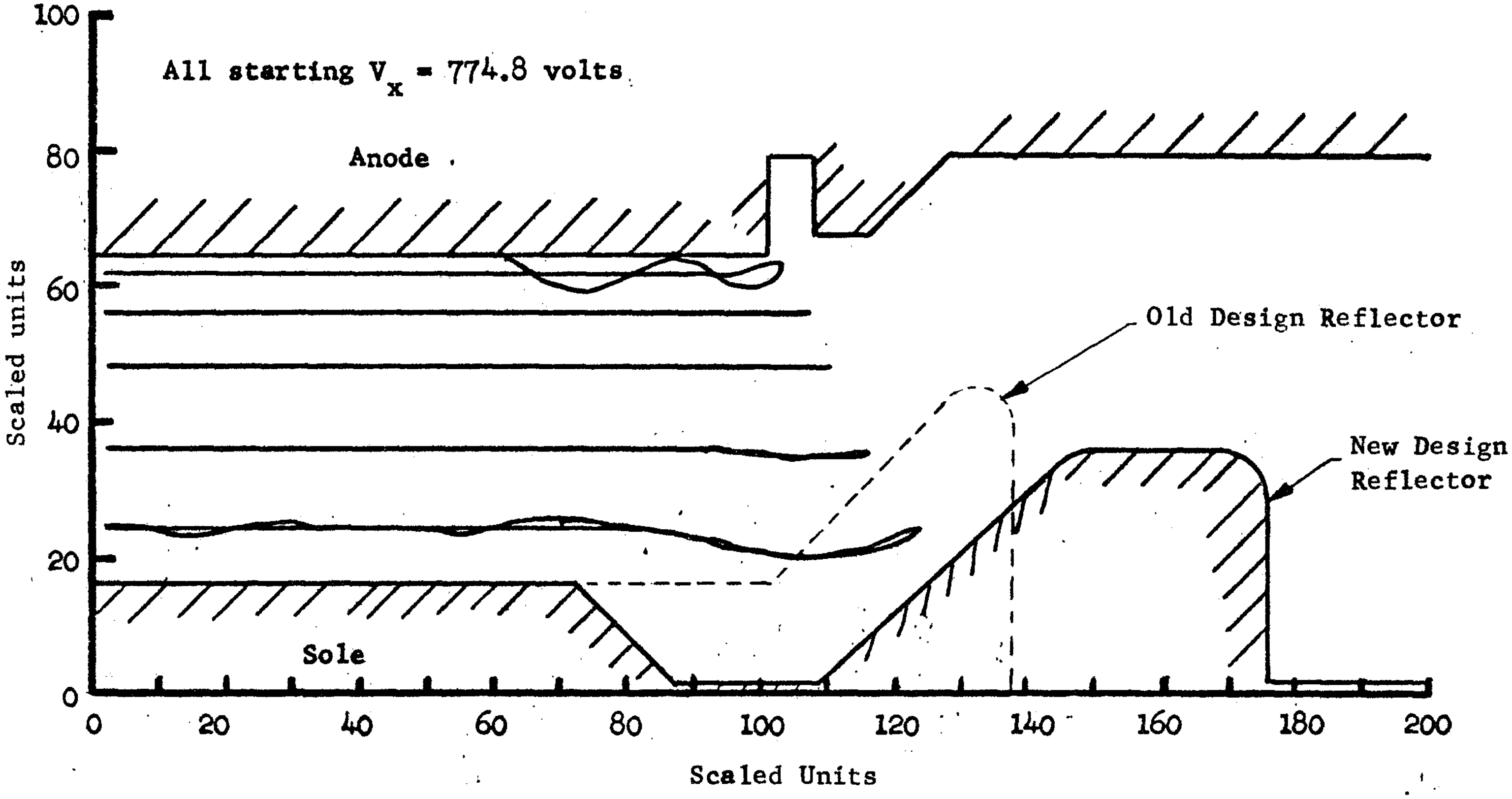

FIGURE 43 OLD AND NEW REFLECTOR DESIGNS.

Trajectories are shown for the new design. Distance scales are in scaled units used in the computer simulation. One scaled unit = 2×10^{-3} in. (5.08×10^{-3} cms).

region of Ey field different from that in the main interaction space. The velocity in the x direction in Figure 43, which is the direction of propagation of the RF wave, is equal to the ratio of Ey to the magnetic field B. In the reflection process, an electron thus travels through a region in the vicinity of the reflector, where the Ey field and consequently the x velocity is different than it is in the main interaction space. Because of this, a reflected electron undergoes a phase shift relative to the wave. Depending on the design of the reflector region and the level between the sole and the anode at which an electron is incident on the collector, this phase shift may represent either an advance or retardation of the electrons with respect to the wave. Since electrons at the top and the bottom of the beam have different axial velocities and thus undergo a different number of reflections during their transit from gun to collector, the phase shift introduced by the reflections from the side can have a significant effect on the RF bunching process.

The possibility of a phase shift between electrons and wave during the reflection process was first raised by Mr. Peter Ramins of NASA in June of 1969 with reference to the UHF tube then being investigated. For the particular parameters of this tube it did not at the time appear to be of significance. When initial results were obtained on the RADC tube, it was found that while the efficiency was about as predicted, the large signal gain was lower than predicted. In the process of investigating this effect on the present NASA program (since it had implications for our design) we investigated the reflection phase shift using the axial injection computer program. Figure 43 also shows the reflector design at this stage. Figure 44 shows the reflector phase shift characteristics determined from the computer calculated trajectories for the design of both Figure 42 and Figure 43. The original design had relatively little phase shift for electrons incident on the reflector at the

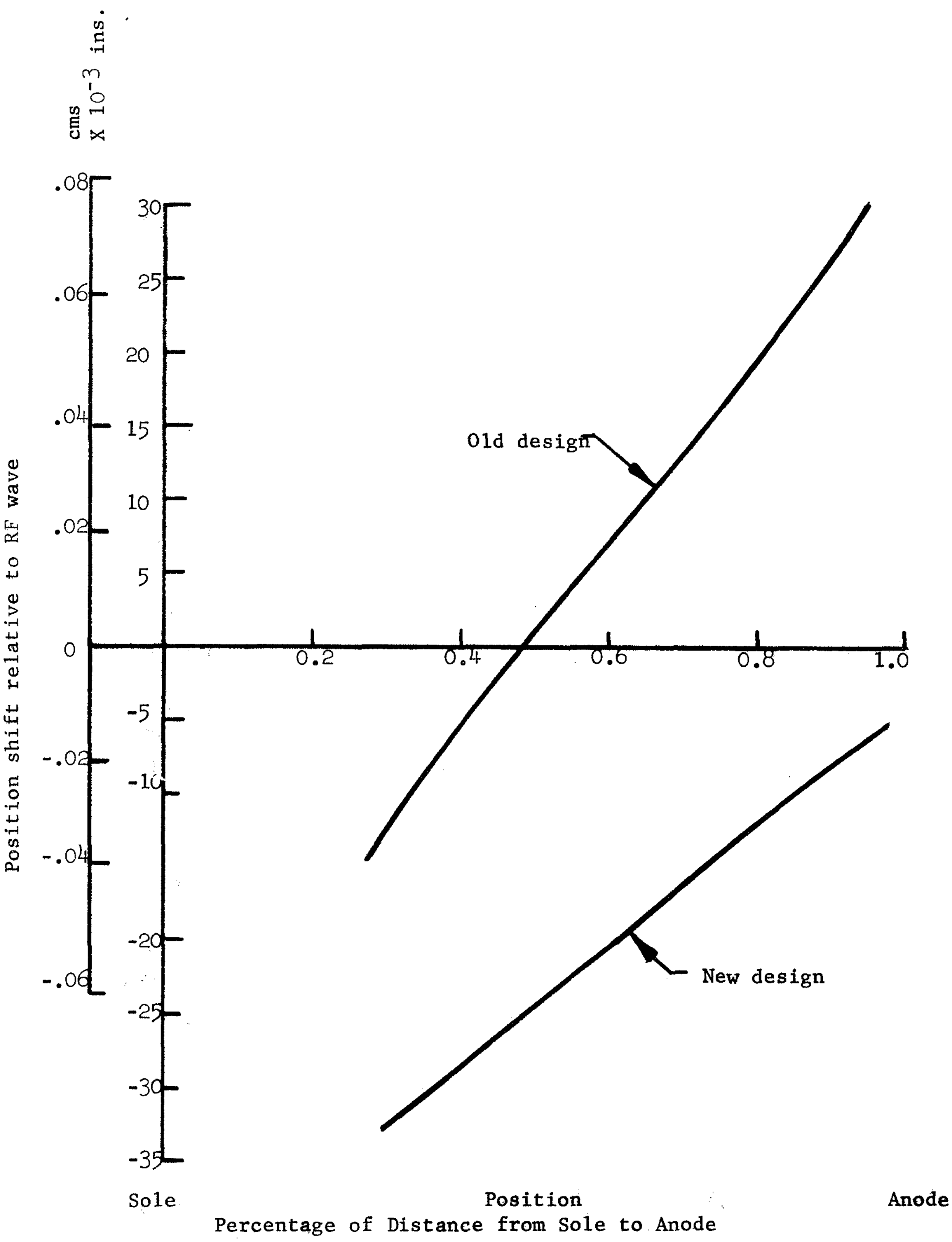

FIGURE 44 PHASE SHIFT OF REFLECTED ELECTRON TRAJECTORY RELATIVE TO RF WAVE AS A FUNCTION OF LEVEL OF INCIDENCE OF TRAJECTORY BETWEEN SOLE AND ANODE

origninal beam level and a phase advance for electrons incident on the collector near the anode level.

Once we realized the reflector phase shifts could be important, we modified the large signal computer program to include these phase shifts. Calculations of the original design showed an effect on gain but a much smaller effect on power output and efficiency. This is evidently the case because of the influence of the RF phase focusing forces in rephasing the electrons after the phase shift. The reflector characteristics thus appeared to explain the discrepancies we saw between the RADC tube performance and the large signal computations.

A problem we had encountered with the RADC tube was a very non-linear dynamic range characteristic as a consequence of the space charge contribution to the small signal gain. It is known that the large values of small signal gain can be reduced by non-uniformities in the interaction space design which have a relatively small effect on the large signal interaction because of the strong phase focusing forces. We thus reasoned that a reflector characteristic as shown for the new design in Figure 43 could be used to linearize the dynamic range. Under small signal conditions the electrons incident on the reflector at the original beam level undergo a phase shift which reduces the small signal gain. Under large signal conditions the phase focusing forces reduce the effectiveness of this phase shift, and in addition, as electrons move toward the anode the phase shift is reduced. This reflector design was chosen for use on this program and was also employed in a subsequent RADC tube. Results on the RADC tube showed substantially improved linearity (Ref. 5).

The reflector design of Figure 42 has been arrived at through a number of iterations using the axial injection trajectory tracing program. As may be seen from figure 42, nearly all of the electrons are reflected with very little cycloiding. Only for those electrons very close to the anode is cycloiding introduced. Since electrons in this region have a very high velocity toward the anode, only a small amount of current will be incident on the reflector at these levels. To obtain the desired phase shift characteristic, the notch in the sole prior to the reflector was found to be necessary.

5.4 The Collector Design

Figure 45 shows a sketch of the collector design employed on this program. There are four separate collector elements located on the anode side of the interaction space. The collector elements are conduction cooled through beryllia supported ceramics to the liquid cooled body of the tube. As shown in Figure 45, the highest voltage collector element is adjacent to the delay line and the cathode potential collector element is at the end of the tube. The spent electron beam is distributed in space across the interaction space, with the highest potential electrons located close to the anode. The highest potential electrons are diverted into the channel adjacent to the anode. The next highest potential group of electrons are diverted into the channel between the first and second collectors, as shown in Figure 45. Figure 45 shows typical trajectories in the region of a single branching channel, as determined by digital computer trajectory tracing techniques. Studies of this sort have shown that the exact shape of the branching channels is not critical and the voltages applied to the collectors are not critical. Distribution of the spent beam occurs in accordance with the potential distribution on the collector elements, with those electrons at a higher potential than a given collector element being diverted into the branching channel. It is thus possible for us to employ unregulated voltages on the collectors. This greatly simplifies the power supply for the multiple element collector and makes it possible

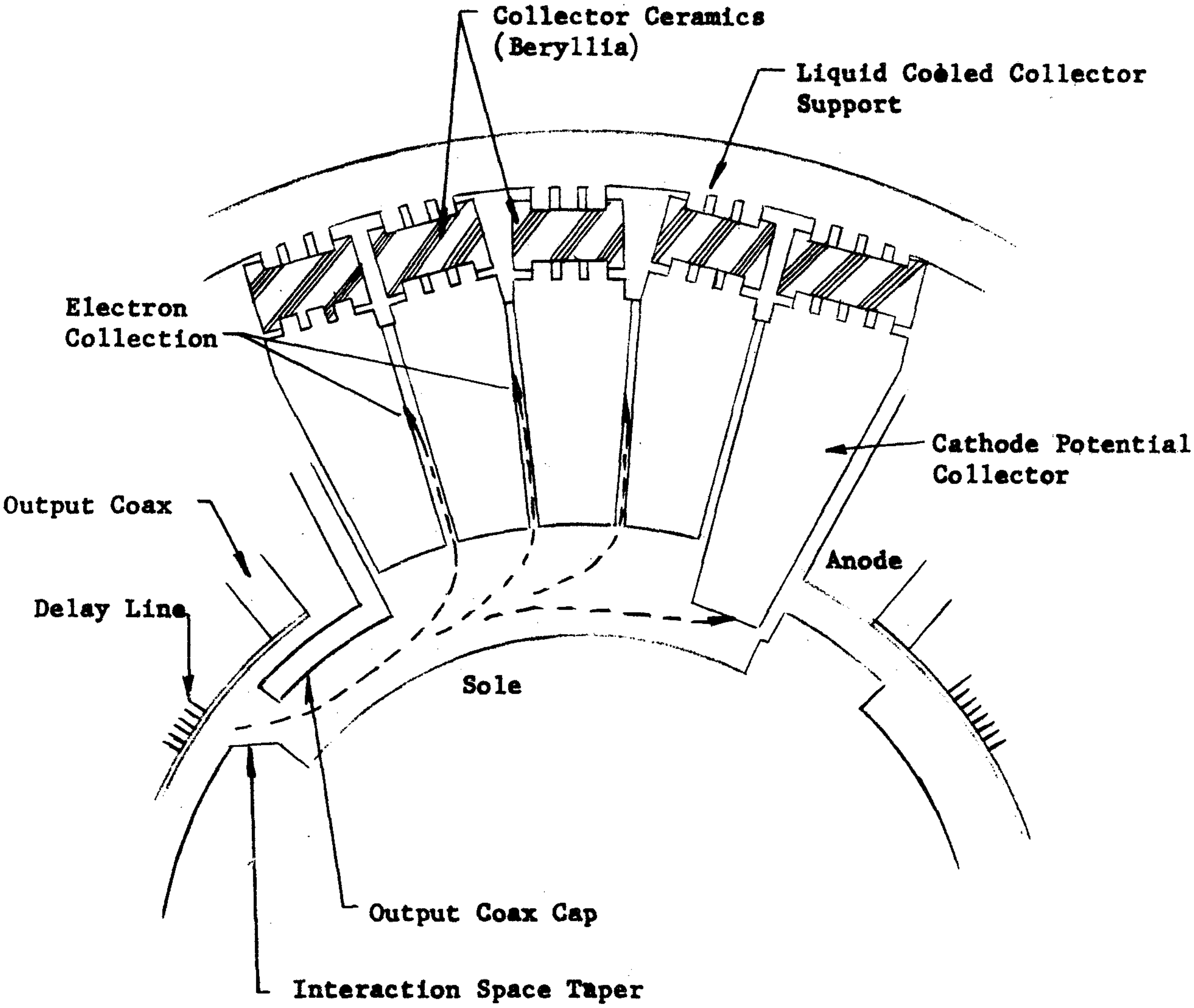

FIGURE 45 SKETCH OF PRESENT COLLECTOR STRUCTURE

Unfavorably phased electrons are collected as cathode potential collector far end remote from heat sink. Collection is assured at this point because of reduced collector to sole spacing.

for us to derive the voltages from an unregulated tapped power supply. From our discussions with power supply designers we have learned that this is feasible without degrading the power supply efficiency and with a relatively small increase in the power supply size as compared to a single voltage power supply.

Once the electrons in the beam have been diverted into the collector channels, collection of the electrons is obtained on the higher potential surface of the branching channel through a gradual reduction of the magnetic field as the branching channel moves away from the interaction space. By adjusting the rate of magnetic field decay we can adjust the dissipation density of the electrons on the collector surface. The width, w, in Figure 45, and the length of the collector channel, l, may be determined arbitrarily from power dissipation considerations and they are not critically related to the RF performance of the tube. This permits us to design a collector which is adequate for the powers which would be required in various applications.

It should be noted that collection of electrons occurs on surfaces at which the dc field gradient suppresses the emission of secondary electrons. Because the electron flow in a crossed-field device is unidirectional, and because the collector is at the end of the tube in the present design, no secondary electrons (even if a few are generated near the corners of the collector elements) can return to the main interaction space.

5.5 Interaction and Large Signal Studies

5.5.1 Preliminary Design Studies

To a certain extent, the design of the high power tube has been made around the capabilities of a delay line which has the required thermal properties and which we have demonstrated can be satisfactorily fabricated. Characteristics of this line were presented in Section 5.1 and are summari~ed in Table VI. Using the value of synchronous voltage chosen, designs can be constructed having a number of different voltages and currents. Increasing the anode to cathode voltage increases the V/V_o ratio and thus improves the electronic efficiency of the CFA which is given by:

$$E = 100\% \left(1 - k \frac{V_o}{V}\right) \qquad (29)$$

where E is the efficiency

V_o is the synchronous beam voltage

V is the cathode to anode voltage

k is a factor which depends on the degree of beam focusing. k varies from 1.0 for a perfectly focused beam to 4.0 for full cycloiding.

This efficiency is a measure of the efficiency of energy conversions from dc to RF for those electrons which strike the delay line. The energy which is converted to RF must, however, flow through the finite attentuation of the delay line to the output. This results in an efficiency degradation which is sometimes expressed by multiplying the above efficiency by a circuit efficiency. In addition, there is a further efficiency degradation due to the unfavorably phased current which is collected either on a side collector or on an end collector. Increasing the V/V_o ratio improves electronic efficiency, but it requires an increase in the magnetic field which reduces the gain per unit length of the tube and therefore reduces the circuit efficiency. An optimum compromise is usually obtained when the electronic and circuit efficiencies result in about equal power dissipations due to current interception on the delay line and attenuation on the delay line. Computer studies of the large signal behavior have indicated that a V/V_o ratio of about ten is close to optimum for this tube. This gives us a cathode voltage of 10 kv.

TABLE VI

DELAY LINE PARAMETERS

Line pitch = 0.048 in. (0.122 cm)
Line width = 0.540 in. (1.370 cm)

Frequency	3.0	3.85	4.80	GHz
Characteristic impedance	65	65	65	ohms
Interaction impedance	50	37.5	25.0	ohms
Phase shift per section	63	90	120.0	degrees
	1.10	1.57	2.09	radians
Synchronous voltage	1241	1002	876	volts
Attenuation	0.50	0.57	0.65	db/in.
	0.20	0.22	0.25	db/cm

Because some of the current will recirculate to collector electrodes either at or near cathode potential, we require a cathode current somewhat higher than the total beam power divided by the anode to cathode voltage. We have made an initial estimate that approximately 1.2 amp of cathode current will be required.

As a next step in the design, we must choose the distance of the beam from the delay line and thus the gain per unit length and the total length of the circuit. Placing the beam very close to the line results in a very high gain per unit length, but also requires a high magnetic field which complicates the gun design and, because the gain is obtained in a short physical length, results in relatively high power dissipation densities. Moving the beam away from the line lowers the magnetic field and lowers the power dissipation densities while increasing the line length. This tends to decrease the circuit efficiency and results in a greater dissipation of power as a result of circuit attenuation.

A further consideration is the possibility of a cyclotron interaction when the tube is operated near a field of 2750 gauss ($.27 w/m^2$). At this field value, electrons crossing the vanes near the edge of the meander line are exposed to the same phase of the RF voltage once each cyclotron period. Operating at this magnetic field could result in a cumulative cyclotron type of interaction which would increase or "pump up" the cycloiding motion of the electrons. Increased cycloiding would, in turn, result in reduced efficiency of operation. Experience on the RADC program has not shown clear evidence of a problem at this field value, so the effect on efficiency is not a major one. Nevertheless, it appears to be desirable for us to stay away from this particular field value by at least 10%.

Two designs have been investigated - a low field and a high field design. The parameters for these two designs are summarized in Table VII. The operating voltages as a function of frequency have been calculated from the relations summarized in section 3.2 and are shown in Figure 46. At fixed voltage the output power should be essentially constant over 200 MHz and the 3 db bandwidth should be about 1000 MHz wide. The nominal beam spacing for the low and high field designs is 0.042 and 0.048 inch (0.1065 and 0.122 cm) respectively. Calculations on the gun show that the same design can accommodate either field value and beam spacing without the introduction of excessive cycloiding.

Now we turn to some first order estimates of the gain of the tube using an approximate theory. This theory serves only as a preliminary design tool. An approximate equation for the high level gain is obtained by calculating the gain, G, neglecting space charge. When we do this, we obtain:

$$G = -6 - \frac{\alpha}{2} + 54.8\ DN \qquad \text{db} \tag{30}$$

where D is the gain parameter

N is the number of slow wave lengths on the circuit

α is the circuit attenuation

The actual large signal gain is usually slightly higher than that given by this equation because of space charge effects. The gain parameter D is given by:

$$D^2 = \frac{1}{2}\left(\frac{I}{V_o}\right)\left(\frac{\omega}{\omega_c}\right) K \left(\frac{\sinh \beta y}{\sinh \beta A}\right)^2 \coth \beta y \tag{31}$$

where I is the beam current

V_o is the circuit synchronous velocity

ω is the radian frequency

ω_c is the cyclotron frequency

TABLE VII

ELECTRICAL DESIGN PARAMETERS

	Low Field	High Field	Units
Frequency	3.0	3.0	GHz
Magnetic field	0.25	0.35	w/m^2
Cathode voltage	7948	11432	volts
Sole voltage	12567	17676	volts
Beam current	1.25	1.25	amps
Line to sole spacing	0.095 0.241	0.095 0.241	inches cms
Line to beam spacing	0.042 0.107	0.048 0.122	inches cms
Sole to front cathode edge spacing	0.030 0.076	0.030 0.076	inches cms
Synchronous voltage	1240	1240	volts
V/V_o ratio	6.4	9.25	
Gain parameter, D	0.040	0.029	
Space charge parameter, S	1.17	1.14	
Nominal output power	5	5	kw
Input power	20	20	w
Gain	24	24	db
Nominal efficiency	55	60	%

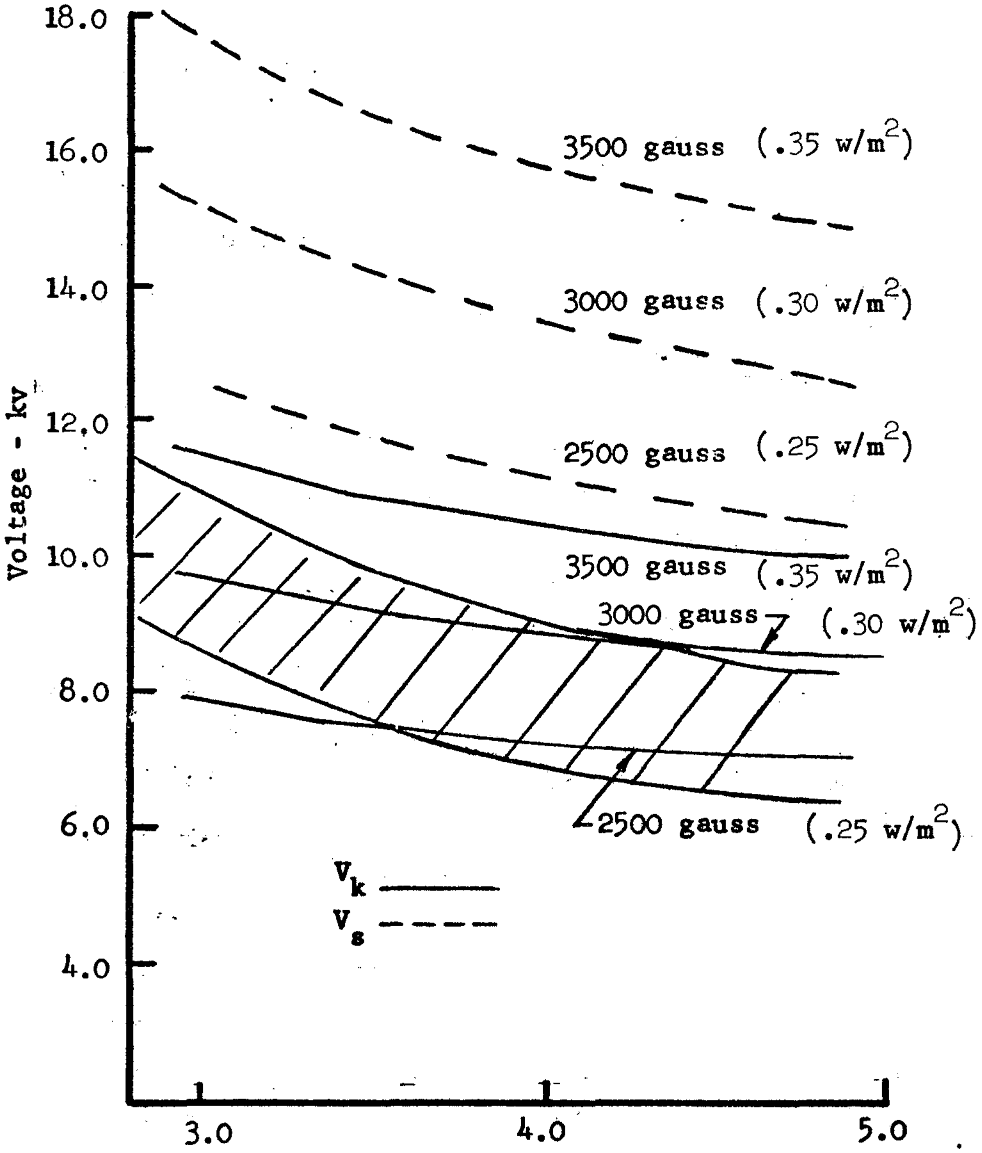

FIGURE 46 CALCULATED OPERATING VOLTAGES FOR VARIOUS VALUES OF MAGNETIC FIELD SHOWING THE "FORBIDDEN" REGION

K is the circuit interaction impedance

β_y is the sole to beam transit angle

βA is the cathode to anode transit angle

The parameter, β, is the ratio of the radian frequency, ω, to the circuit phase velocity, v.

$$\beta = \frac{\omega}{v} \tag{32}$$

Calculations of the low level gain including space charge may be conducted employing an additional space charge parameter, S. This parameter is defined as:

$$S = \frac{1}{2D} \frac{\Delta v}{v_o} \tag{33}$$

where Δv is the total velocity slip across the beam

v_o is the synchronous velocity

The low level gain is given in terms of D, S, and α by:

$$\text{Gain} = -20 \log_{10} 2(1 + S^2) - \frac{\alpha}{2(1 + S^2)} + 54.8\, DN\sqrt{1 + S^2} \tag{34}$$

A time share computer program has been written for examining a number of preliminary designs using these equations. The calculated gain both with and without space charge is shown in Figure 47 for an operating current of 1.0 amps.

Figure 47 shows that space charge effects introduce a difference between the large and small signal gain which, in turn, increases with frequency. The tube tends to be more and more nonlinear at higher frequencies. The reflector design employed is expected to be adequate to give a linear dynamic range characteristic to at least 3.5 GHz.

5.5.2 The Large Signal Computer Program

The large signal computer program we are employing for

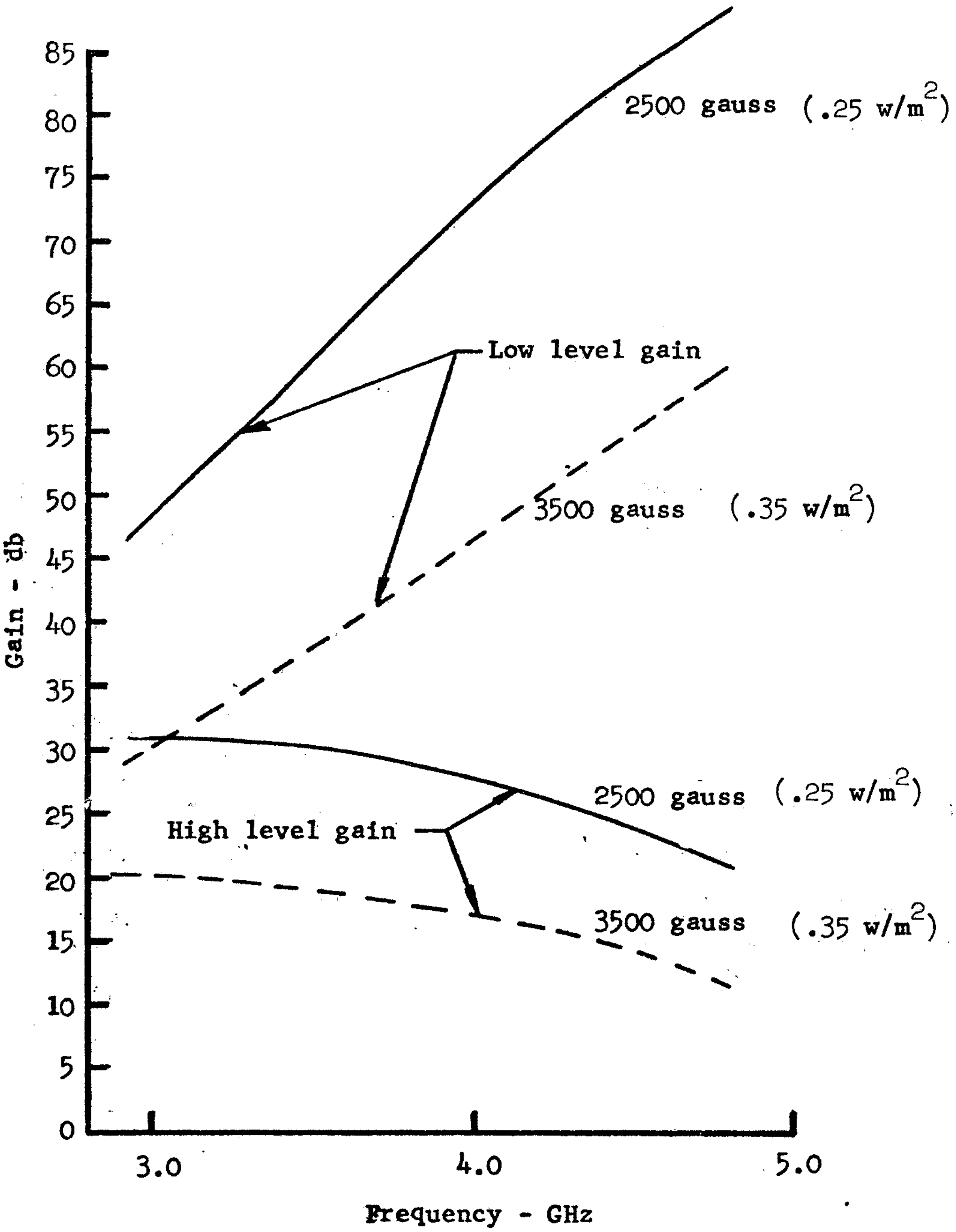

FIGURE 47 CALCULATED HIGH AND LOW LEVEL GAINS FOR THE TWO VALUES OF OPERATING MAGNETIC FIELD

studying injected beam and axial injection tubes is quite sophisticated and has undergone years of refinement. A digital computer such as an IBM 360/65 employed in the batch processing mode is necessary. The general principles of the computer program follow those described in an original paper by Hull and Kooyers (Ref. 16). The particular injected beam program we are currently employing was obtained from G. P. Kooyers of Universal Computer Applications and represents several iterations of improvement since the preparation of the original program. The current program employs new methods of calculating the space charge through the use of elliptic functions, and modified methods of taking into account the effects of frame acceleration in the force equations. The whole program is in double precision so as to permit us to do meaningful low level studies. The computer analysis proceeds by breaking up the space charge into a number of individual charge rods. A single wavelength of the space charge and the RF circuit wave are then followed through the tube, breaking the total transit time of the wave through the tube into a number of very small time steps. For each time step, the forces on the space charge rods are calculated from the RF field strengths and from the location of the other charged rods. The rods are then allowed to move a small increment with these forces held constant. The current induced in the delay line as a result of the rod motions is then calculated and the amplitude of the RF fields on the line is incremented. Effects of attenuation are also taken into account.

To study the axial injection system, this program has been further modified by the Varian/Eastern Tube Division, Union, N. J. To produce a true three-dimensional simulation would have been extremely complicated and would have required an excessive amount of computer time. However, we can obtain sufficient accuracy by simulating the third dimension by introducing the space charge rods into a basically two-dimensional simulation such as used for the conventional injected beam. The rods are introduced at various positions along the interaction space. In the program currently in use, various logical branches allow us to test the rods after they have been in the interaction space for one or more axial drift transit times across the space. This permits us to introduce collectors on the far side of the interaction space, to reflect the rods entirely or in some cases to reflect those above a certain level and collect those below a certain level. The program thus allows us to calculate the effects of collecting unfavorably phased electrons at a partial reflector on the side of the interaction space opposite to the gun. The axial drift velocity of the electrons across the interaction space is simulated in this program by introducing rods suddenly into the interaction space, allowing them to remain in the interaction space for a time equal to the axial transit of the current across the interaction space, and then either removing or reflecting the rods depending on the logic we have chosen.

5.5.3 Large Signal Calculations

Using the large signal computer program, calculations have been made at both the low and the high magnetic field levels. These calculations included the effect of reflector phase shift employing the "new" characteristic shown in Figure 44. The gain as a function of length is shown in Figures 48 and 49 for the low and high field cases respectively. The calculated efficiency in both cases is between 55% and 60% for the five collector designs we are employing at this time. In making the calculations we have assumed that three fourths of the kinetic energy associated with the x directed velocity (direction of wave propagation) is recovered in the collector but that there is no recovery of axial kinetic energy. Each charge rod in the interaction space at the end of the calculation

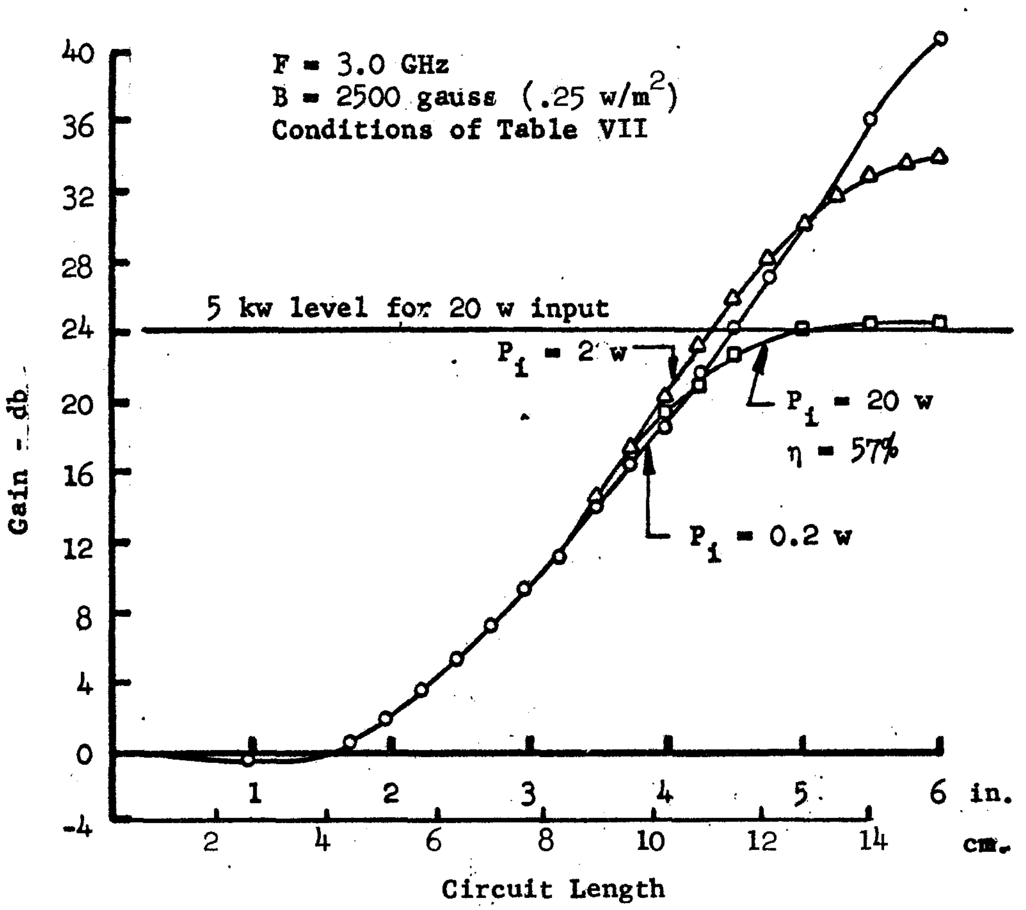

FIGURE 48 COMPUTER CALCULATED GAIN AS A FUNCTION OF LENGTH FOR THE LOW MAGNETIC FIELD CASE

$F = 3.0$ GHz
$P_i = 30$ w
$I_b = 1.25$ a
$B = 3500$ gauss ($.35$ w/m^2)
$V_k = 11433$ v
$V_s = 17721$ v

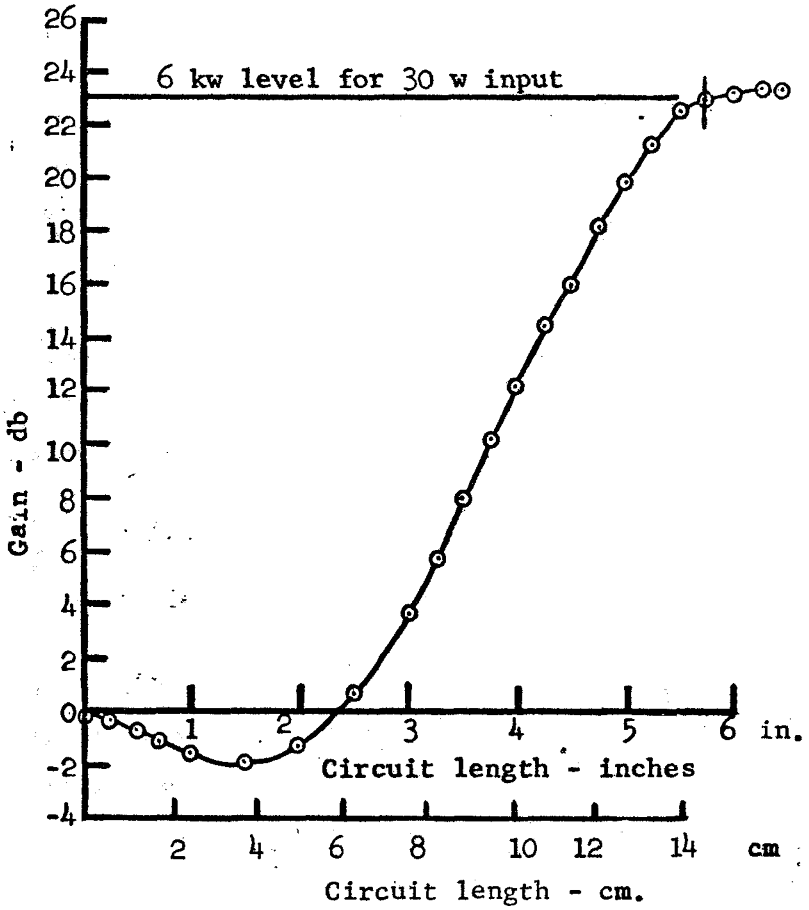

FIGURE 49 COMPUTER CALCULATED GAIN AS A FUNCTION OF LENGTH FOR THE HIGH MAGNETIC FIELD CASE

is thus moved downward in potential by three-fourths of the synchronous voltage. The assumption is then made that the rod is collected at the next highest collector potential. The results of these calculations are summarized in Table VIII.

5.6 Prebunching Electrode Design

In our original plans we had intended to include a "prebunching" electrode along the side of the interaction space opposite the gun as shown in Figure 50. This electrode is operated at or near cathode potential. Electrons on their first transit across the interaction space encounter this electrode which is designed to collect the unfavorably phased electrons which have moved downward from the original beam position and to reflect the favorably phased electrons. Removal of the unfavorably phased electrons at this point, before they have extracted significant energy from the RF wave, can enhance the efficiency of the device. The prebunching element must be stopped before the high power region of the tube is reached because favorably phased electrons exist in this region at potentials below the cathode potential. This occurs because of "tumbling" of the bunch introduced by space charge effects. Computer simulation studies have shown that removal of this favorably phased current decreases the efficiency.

Before assembling the experimental tube we decided not to include the prebunching electrode because of the mechanical complexity involved. However, its introduction at the appropriate stage in the developement of a tube is feasible.

Using the same design techniques as were used for the side reflectors, the prebuncher design of Figure 51 was evolved. Our trajectory tracing studies show that electrons above the zero equipotential level are reflected with very little cycloiding. The phase shift characteristics for this electrode are shown in Figure

TABLE VIII

SUMMARY OF LARGE SIGNAL CALCULATIONS OF POWER OUTPUT AND EFFICIENCY

	Low Field	High Field	Units
B	2500 0.25	3500 0.35	gauss w/m^2
V_K	8,683	11,433	volts
V_S	14,320	17,721	volts
I_K	1.50	1.25	amps
P_{in}	20	30	watts
P_{out}	5634	6000	watts
Efficiency (5 collectors)	58.6	59	percent

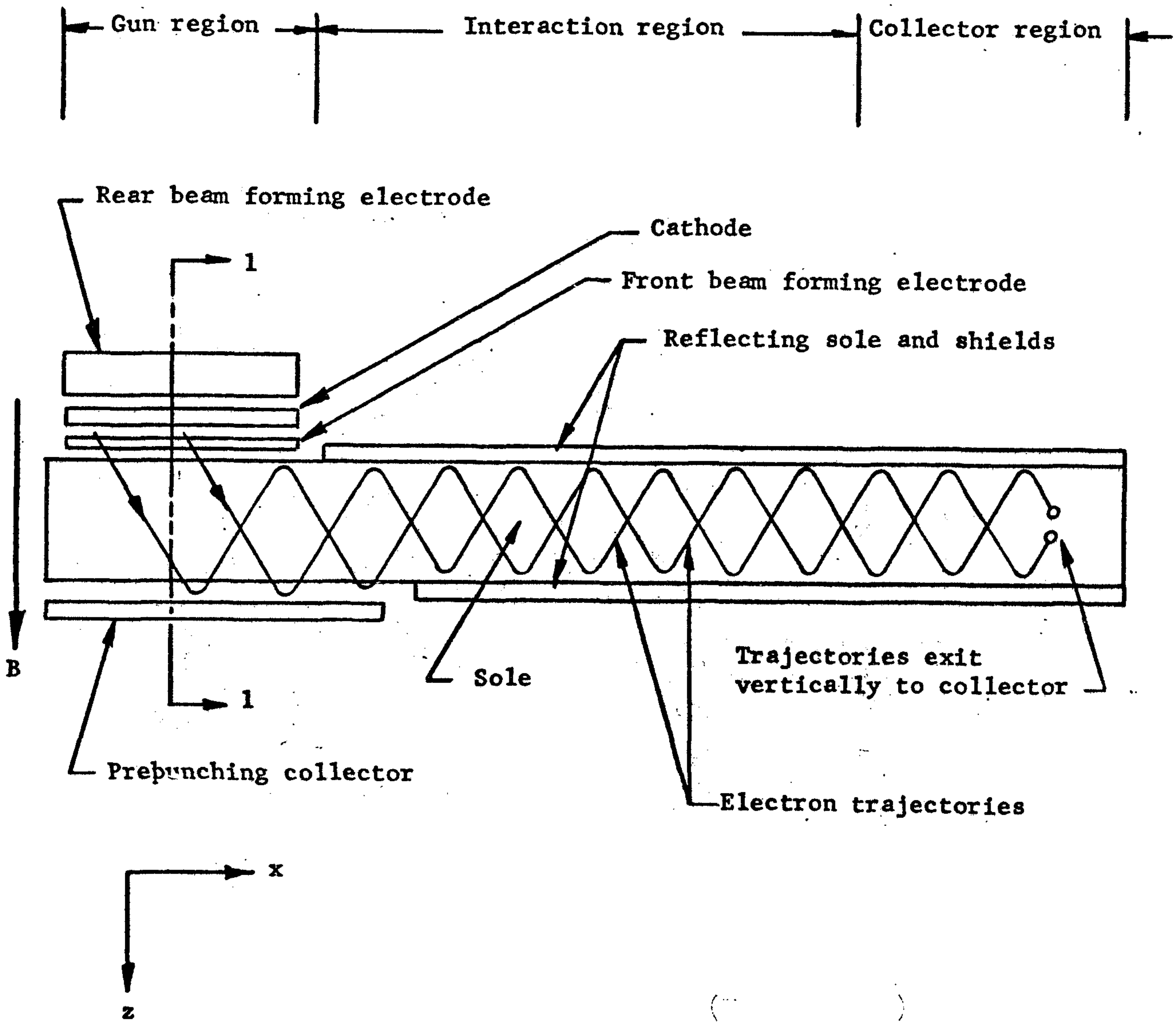

FIGURE 50 SCHEMATIC VIEW LOOKING FROM ANODE TOWARD SOLE SHOWING LOCATION OF PREBUNCHING COLLECTOR. (U)

(U) Drawing is not to scale and in actual tube, velocity in x direction exceeds that in z direction by several times.

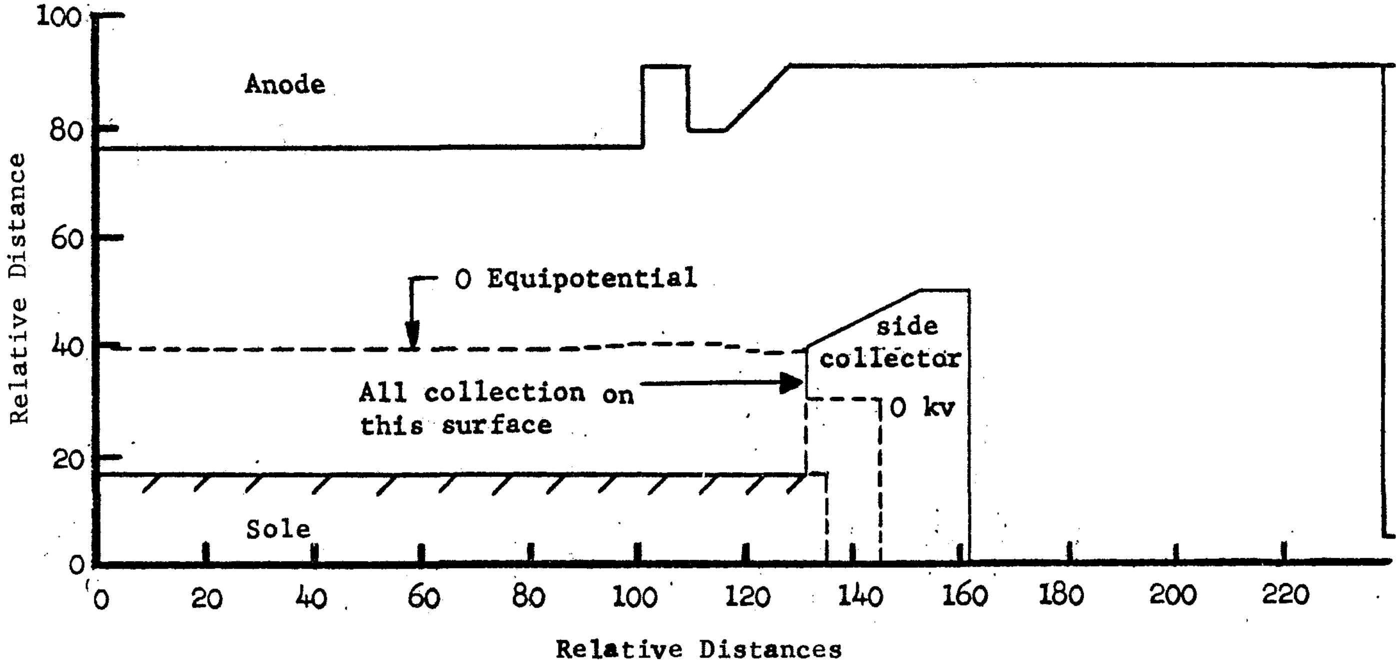

FIGURE 51 PREBUNCHING ELECTRODE DESIGN

The distance scale is in scaled units used in the computer simulation. One scaled unit is equal to 2 mils (2×10^{-3} inches or 5.08×10^{-3} cm.)

52 and are satisfactory. Electrons which are collected on the prebunching electrode are collected in a region in which the dc electric fields inhibit secondary emission. The computations show that the prebunching collector regains both axial and logitudinal kinetic energy from the collected electrons.

A computer simulation of a tube with a prebunching collector was conducted under somewhat different conditions than those of the previous simulations so the results are not directly comparable. They do show, however, that the prebunching collector can be used to increase the efficiency by about ten percentage points. This assumes recovery of half of the kinetic energy associated with both longitudinal and axial motion of the electrons.

5.7 Mechanical Design of the Experimental Vehicle

The experimental vehicle is made in circular format and utilizes many construction techniques developed on other programs.

The delay line is fabricated from a machined meander line which is brazed to individual beryllia ceramic rods which are in turn brazed to a liquid cooled copper base. This anode structure together with the multi-element collector structure, is in turn mounted in a coexpansive stainless steel housing. Figure 53 shows a photograph of the delay line. Figure 54 shows a photograph of the collector assembly and Figure 55 shows a photograph of the combined anode and body assembly.

The gun is fabricated from a clamped up assembly, as shown in Figure 56. This assembly is in turn screwed to one cover plate along with the sole. Figure 57 shows a photograph of a complete sole subassembly.

Final assembly consists of heliarc welding the cover plate sub-assemblies to the body sub-assemblies which are shown in Figure 57.

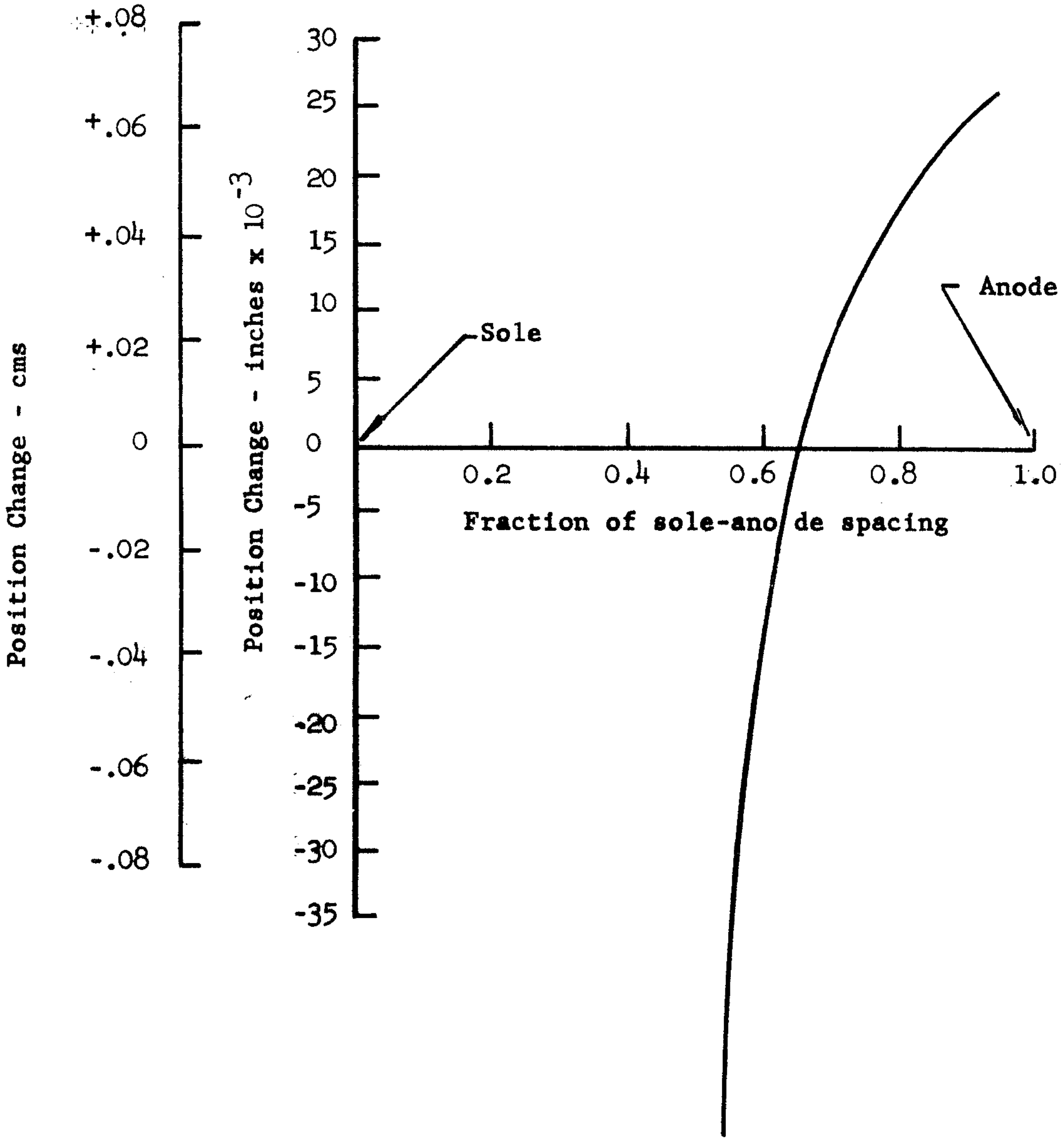

FIGURE 52 PHASE CHARACTERISTICS OF PREBUNCHING ELECTRODE

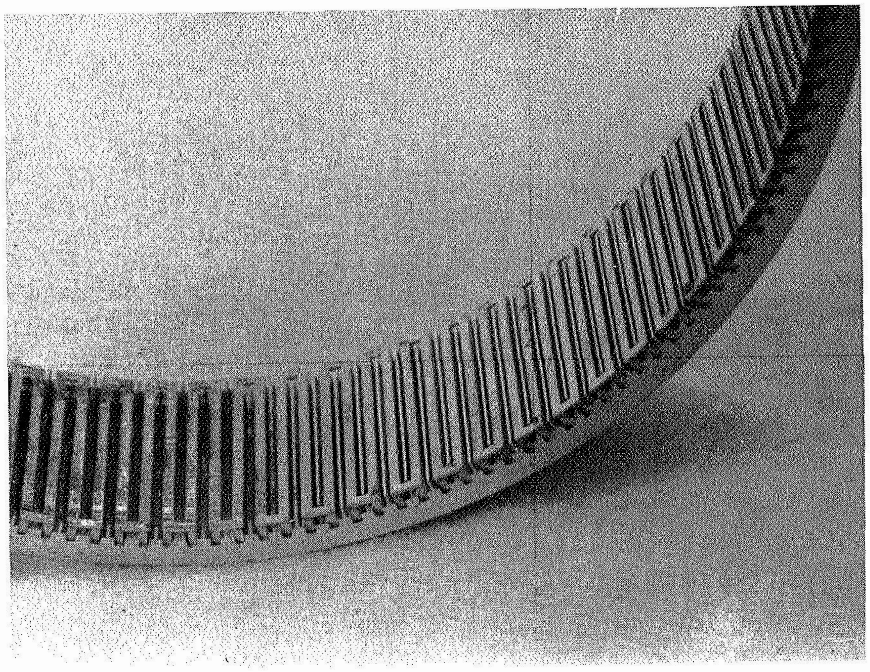

FIGURE 53 THE DELAY LINE

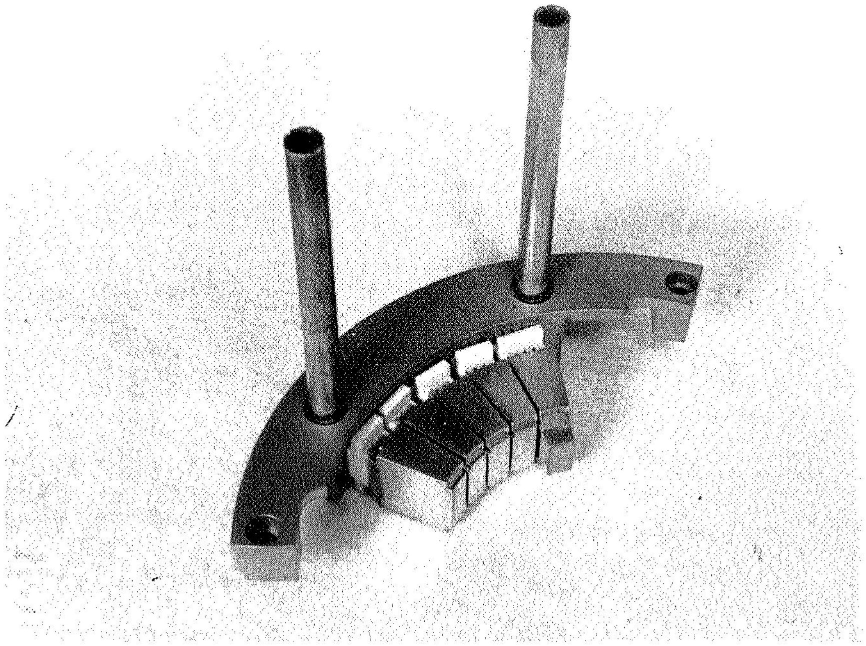

FIGURE 54 THE COLLECTOR ASSEMBLY

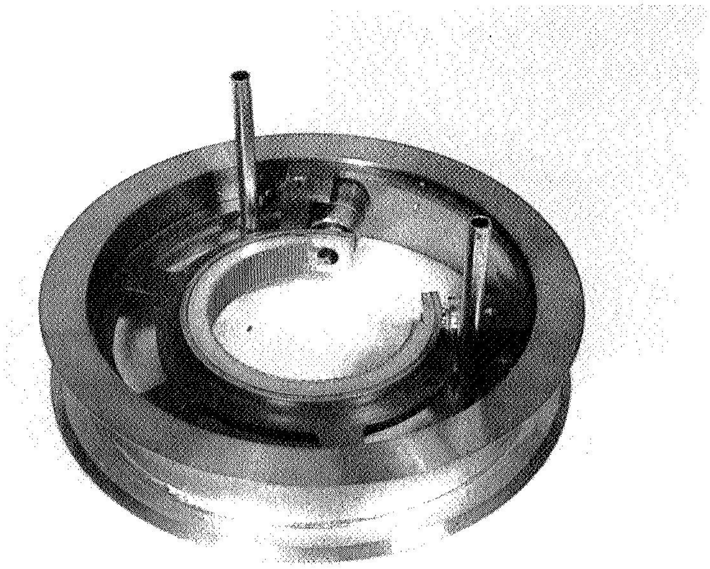

FIGURE 55 COMBINED ANODE AND BODY ASSEMBLY

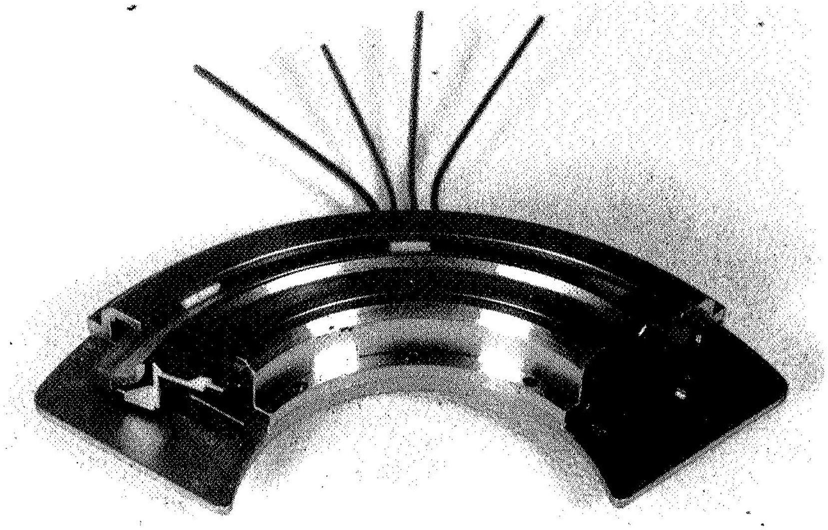

FIGURE 56 CLAMPED-UP GUN ASSEMBLY

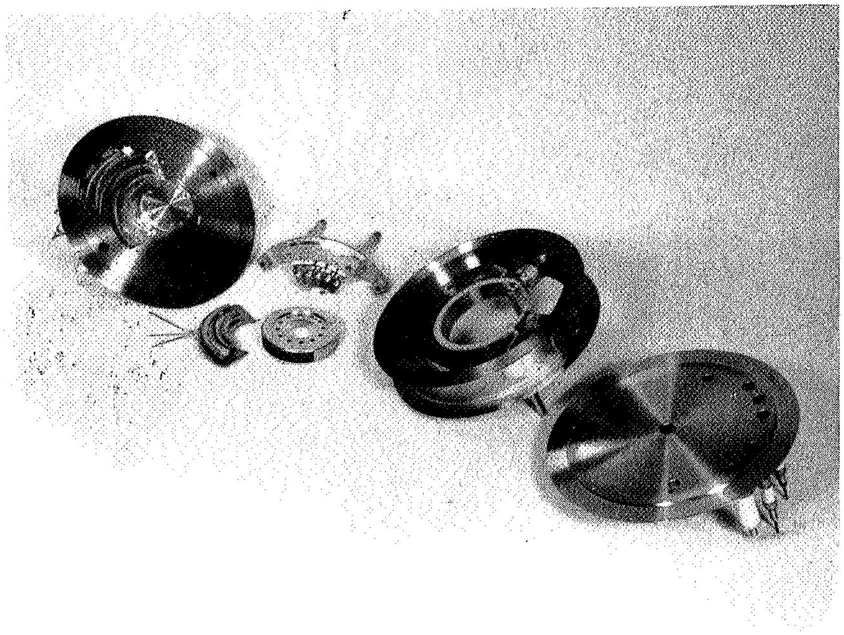

FIGURE 57 SOLE SUBASSEMBLIES

6.0 EXPERIMENTAL RESULTS

One tube, No. K72L was brought to hot test on this program. Problems with beam optics resulting in poor beam transmission and lowered efficiency limited the operating conditions to low duty cycle (0.01) pulsed testing at full (100 watts peak) RF drive. Figure 58 shows the peak power output obtained as a function of cathode current with 100 watts drive, at a frequency of 3.0 GHz. Maximum peak power out was 5.75 KW at 3.0 amps beam current, with a conversion efficiency of 25%.

Subsequent investigations indicated that the low efficiency was the result of poor beam transmission. Under zero drive conditions only 20% of the total cathode current reached the collector system, 35% was intercepted on the delay line and the remaining 45% was apparently escaping from the interaction space and collected on the tube body.

Experience with the Vaxitron amplifier built on the RADC program indicated that under zero drive conditions over 90% of the cathode current was transmitted to the collector system. A detailed comparison was made of the geometry of the two designs with regard to those dimensions critical to beam optics. A minor discrepancy was found in the end hat (reflector) geometry of Tube No. K72L as compared with the RADC tube, and K72L was rebuilt with these dimensions changed to conform more closely to the original design. However, hot test results of rebuilt tube No. K72L-1 showed no significant improvement in beam transmission. A further careful study was then made of the gun geometry. In particular, the geometry was compared with that of a gun of the same two inch circumferential length but without the tapered transition region between the gun and the interaction space. This RADC gun had the cross-sectional geometry shown in Figure 42 whereas the gun employed on this program had the geometry shown in Figure 40. We could find no explanation

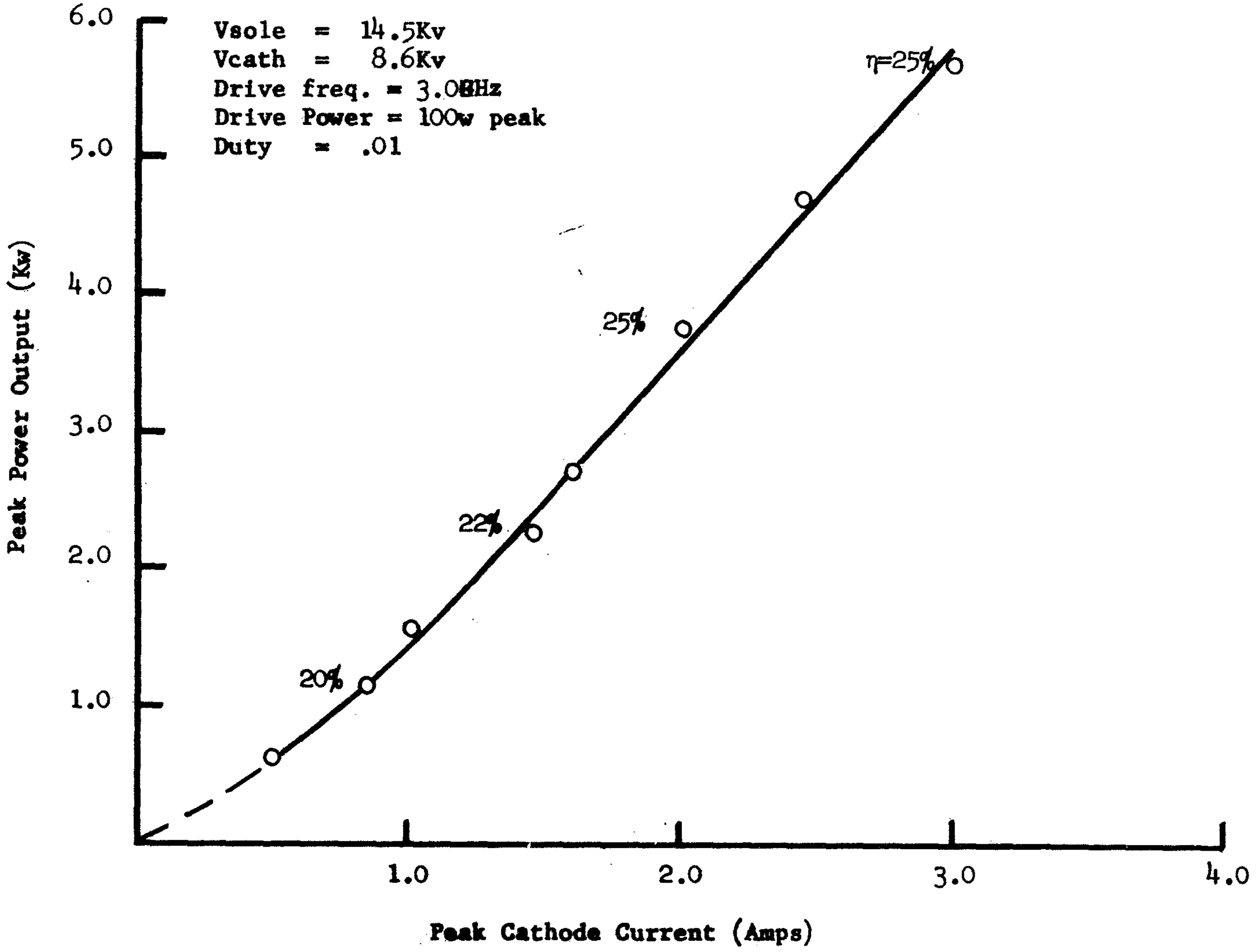

FIGURE 58 PEAK POWER OUTPUT VERSUS CATHODE CURRENT

for the poorer focusing of the NASA gun (which was supposed to produce a better beam) in these cross-section sketches. Then we studied the cross-sections through the transition region between the end of the gun (circumferentially) and the reflector on the gun side of the interaction space. When these cross sections were compared, a probable reason for the poor focusing of the NASA tube emerged. The means of mounting the NASA gun was different from that used for the RADC gun and the geometry of part of the clamping structure was such that it had an effect on the fields in the circumferential transition region between gun and reflector. This transition region extended over a distance of almost one inch over which the reflector was tapered in a complex shape from an axial position to the rear of the cathode to its normal position at the side of the interaction space. The location of the clamp caused the introduction of circumferential electric fields in this region. These fields gave rise to an E/B drift velocity vertically upward from the sole toward the anode. Although this problem existed only along one side of the interaction space, the length of the distorted field region was sufficient so that all the electrons were exposed to this region at least once as a result of their axial motion. The lesson to be learned from this is that the transition region at the circumferential end of the cathode is critical and that its design must be studied as carefully as that of the gun itself.

A new transition region design was then made which appears to avoid the problem with circumferential fields in the transition region. With this revised design we believe that the NASA gun would give the improved focusing predicted by the computer simulations. We were not able to incorporate this revised gun in an operating tube because of lack of further funding.

Although the experimental results on the program were disappointing, the program made two significant contributions to our knowledge of axial injection CFA's. The first of these was an understanding of the importance of designing the transition region to avoid circumferential fields and the second was an understanding of the significance of the phase shift introduced by the reflector. The insight obtained on the reflector design as discussed in Section 5.3 was used to modify the design of the RADC tube. Figure 59 shows the power output vs power input characteristics of this tube with the original reflector design and with the modified reflector design. The data is presented in normalized form because of the classification of the RADC effort. However, Figure 59 shows that a 20 db increase in dynamic range was realized through application of the design techniques discussed in Section 5.3.

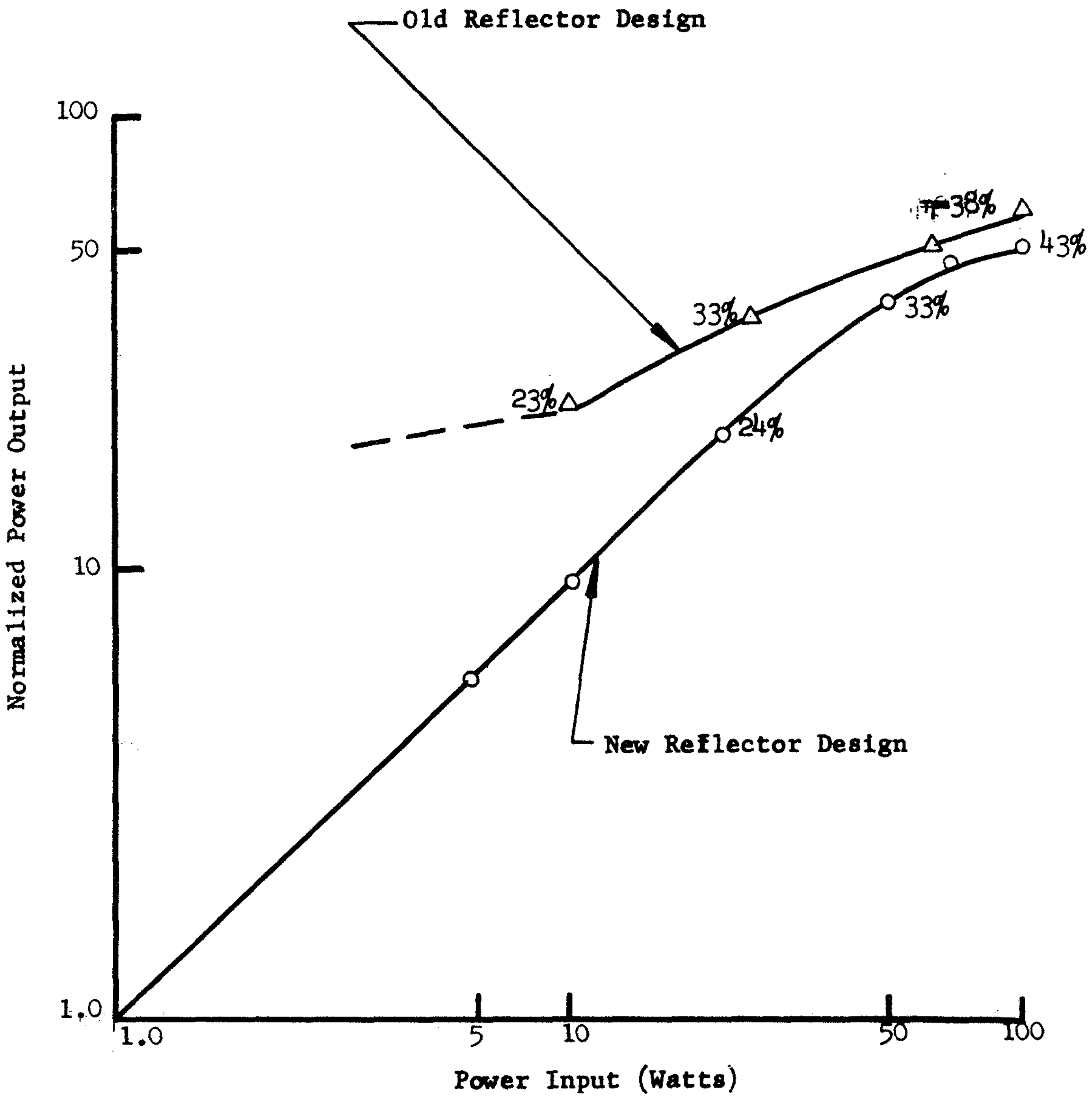

FIGURE 59 POWER OUTPUT VERSUS POWER INPUT BEFORE AND AFTER REFLECTOR DESIGN

7.0 CONCLUSIONS AND RECOMMENDATIONS

Although significant RF data was not obtained from the experimental vehicle, a number of conclusions can be drawn from the analytical studies as well as from the results obtained on the RADC version of the tube. These are:

(1) The original concept of a reentrant axial injection CFA as discussed in the study of NAS3-11516 does not readily lead to a high efficiency design which has a linear regime and is zero signal stable. This approach can be used in an amplifier to be operated at saturation at all times.

(2) The revised approach of a non-reentrant axial injection CFA as described in section 3 is feasible as demonstrated on the RADC program (Ref. 5).

(3) The gun design used on this program was unsatisfactory because of aberrations at the end of the emitting region near the collector. The same gun without the tapered transition region employed here was tested successfully in a beam tester on the RADC program. A shorter version of this gun gave efficiencies in such tubes of up to 49%.

(4) The type of gun used in this study but without the tapered transition region should result in an efficiency of over 50% in an optimized design. Use of the prebunching collector should raise this to over 60% and a satisfactory introduction of the tapered transition should increase the efficiency to close to 70%.

(5) The gun designs which have been tested work at a current density as high as 2.0 amps/cm^2. Calculations indicate that axial injection guns having a current density of 0.5 a/cm^2 are feasible for this application but this has not been demonstrated. Extrapolation of a reduction of current density to 0.5 a/cm^2 is more uncertain than extrapolation of efficiencies of 60%.

(6) With fifteen or more collector elements, the CFA efficiency should be in excess of 50% when it is operated at one-third saturated power output. The CFA thus holds the promise of being an efficient amplifier in the linear regime.

(7) By a combination of an axial injection CFA design for minimum space charge contribution to the gain and by properly designing the reflector electrodes, the CFA can be made to have a linear dynamic range characteristic at the powers and frequencies of this study.

In summary, we believe the approach outlined here is both feasible and attractive for an S-band, 5 KW space borne amplifier for use in the AM mode of operation or at power levels below saturation. It is feasible for use in an FM mode of operation and can probably be more efficient than a TWT. However, the margin of performance over that obtained with a TWT is reduced for FM operation and the development effort required is probably greater than that for a comparable TWT.

We believe that development of this or a similar device should be pursued if interest in AM modes of operation continues to exist. As shown by this study, the area of greatest uncertainty relates to the gun. We recommend that further studies of the beam optics and the reduction of cathode current density take place before a full scale development is undertaken.

APPENDIX

NEW TECHNOLOGY

There are two reportable items of new technology under Contract NAS-3-11528, as follows:

1. Title: Means of Linearizing the Dynamic Range Characteristics of an Axial Injection CFA through Proper Design of the Reflector Electrode.

   Where described: Pages 108-115 of Final Report.

2. Title: Design Techniques for Transition Between Circumferential End of Axial Injection Gun and Adjacent Reflector Electrode.

   Where described: Pages 141-143 of Final Report

The major contribution of this program was in identifying the critical nature of this region and the importance of avoiding circumferential electric fields in this region. The revised design to avoid these fields was not evaluated on the program.

SYMBOL TABLE

a	sole to line spacing
A	beam cross-section area
B	magnetic field
B_o	shunt susceptance in Campbell's equation
c	velocity of light
C_{10}	finger to ground capacity per unit length
C_{12}	finger to finger capacity per unit length
d	distance from sole to bottom of beam
d_+	distance from line to top of beam
D	gain parameter
e	electronic charge
E_y, E_z	y and z components of dc electric field
f	frequency
G	gain
h	width of beam parallel to magnetic field
I	current
J_o	cathode current density
K	ratio of maximum energy on peak of a cycloid to average energy
K	interaction impedance
k	free space phase constant (ω/c) in Campbell's equation
L	cathode length in the x direction
m	mass of an electron
N	number of slow wave wavelengths along the delay line
P	power
S	space charge parameter
t	time, beam thickness
t_o	thickness of Brillouin beam in injected beam CFA
t_k	vertical (parallel to y coordinate) projection of cathode

SYMBOL TABLE

v_x, v_y, v_z	velocity in the x, y, z direction
v_{x+}, v_{y+}, v_{z+}	velocity of top beam edge in the x, y, z direction
v_{x-}, v_{y-}, v_{z-}	velocity of bottom beam edge in the x, y, z direction
v_o	synchronous velocity
V_x, V_y, V_z	voltage equivalent of v_x, v_y, v_z ($= v_x^2/2\ e/m$, etc.)
V_{x+}, V_{y+}, V_{z+}	V_x, V_y, V_z at top edge of beam
V_{x-}, V_{y-}, V_{z-}	V_x, V_y, V_z at bottom edge of beam
V_a	cathode to anode voltage
V_{Ka}	cathode to anode voltage
V_s	sole to anode voltage
V_{sA}	sole to anode voltage
V_{sK}	sole to cathode voltage
V_c	cathode to collector voltage
V_{c1}, V_{c2}, etc.	cathode to collector 1, 2, etc. voltage
w	cathode width (parallel to magnetic field)
X	series reactance in Campbell's equation
x	coordinate direction parallel to RF wave velocity (also called circumferential direction)
Y_o	characteristic admittance
y	coordinate direction from sole to anode parallel to dc electric field (also called radial direction)
y_K	y distance from sole to a point on the cathode
y_{K+}, y_{K-}	y distance from sole to point on cathode where top (+) or bottom (-) trajectory originates - i.e. left or right edge of cathode
Z_o	characteristic impedance
z	coordinate parallel to the magnetic field (called the axial direction)

SYMBOL TABLE

α	attenuation
β	phase constant
βy	sole to beam transit angle
βA	cathode to anode transit angle
Δv_x, Δv_z	differences in the x and z velocities
ΔV_x, ΔV_z	differences in top and bottom x, z voltages
ΔV_{zI}	ΔV_z in the interaction space
ΔV_{zK}	ΔV_z at the exit to the Kino region of the gun
G_o	permittivity of free space
η	efficiency, e/m for an electron
λ	slow wave wavelength
ρ	charge density
θ	phase shift per section of line, cathode tilt angle
θ_g	gap transitangle
ω	radian frequency
ω_c	cyclotron radian frequency

REFERENCES

1. G. Bernstein and W. Sylvernal, "Analytic Design of Spaceborne Axial Injection Crossed-Field Amplifiers," S-F-D laboratories Final Report NASA CR-72393, NASA Lewis Research Center, Contract No. NAS 3-11516, Sept 1968, 254 p

2. G. Bernstein, H. McDowell, T. Schultz, "Feasibility Model of an Advanced Crossed-Field Amplifier for Space Communications Systems," S-F-D laboratories Final Report NASA CR-86334, NASA Electronics Research Center, Cambridge, Mass., Contract No. NAS 12-653, Jan. 1970, 78 p

3. R. Bitzer, J. Hentschel, "Octave Bandwidth S-Band Power Amplifier," S-F-D laboratories Final Report RADC-TR-69-59, Rome Air Development Center, Griffiss Air Force Base, N.Y., Contract F30602-68-C-0030, March 1969, 46 p.

4. T. Schultz, "High Power Crossed-Field Amplifier," S-F-D laboratories/A Varian Division Final Development Report, Naval Ship Systems Command Contract No. N00024-68-C-1069, May 1970, 74 p

5. H.T. Closson, H.L. McDowell, "An Octave Bandwidth S-Band Power Amplifier," S-F-D laboratories Final Technical Report RADC-TR-70-258, Rome Air Development Center, Griffiss Air Force Base, Contract F30602-69-C-0239, Nov 1970, 68 p

6. T. Schultz, "High Power Crossed-Field Amplifier," S-F-D laboratories/A Varian Division Interim Development Report No. 9, Naval Ship Systems Command, Contract No. N00024-68-C-1069, Sept 1970, 38 p

7. H.L. McDowell, E.K. Shaw, N. Eisner, "A Feasibility Study for a Half Octave Bandwidth X-Band Crossed-Field Amplifier," Varian Associates/Eastern Tube Division Final Technical Report RADC-TR-70-145, Rome Air Development Center, Griffiss Air Force Base, N.Y. Contract F30602-69-C-0205, Sept 1970, 323 p

8. G.S. Kino and N.J. Taylor, "The Design and Performance of a Magnetron Injection Gun," IRE Transactions on Electron Devices, Jan 1962

9. A. LeBlond and G. Mourier, Annales de Radioelectricite, V 9, No. 36, April 1954, p 180-192, and V 9, No. 38, Oct 1954, p 311-328

10. J. Arnaud, Thesis a la Faculte des Sciences de l'universite de Paris, "Structures Multiperiodiques Pour Tubes A Propagation D'Onde De Grande Puissance"

11. N.J. Taylor, "Magnetron Injection Guns derived from Theoretical Space Charge Flow Solutions," Proc 4th International Conference on Microwave Tubes - Microwaves, Centrex, Eindhoven, Netherlands, 1963, p 583-587

12. B. Arfin, "Design of a High Perveance Magnetron Injection Gun and Some Applications," Proc 4th International Conference on Microwave Tubes - Microwaves, Centrex, Eindhoven, Netherlands, 1963, p 595-598

13. R. Ho and T. VanDuzer, "The Effect of Space Charge on Shot Noise in Crossed-Field Electron Guns," IEEE Trans Electron Devices, Feb 1968, p 75-84

14. R.P. Wadhwa and M.L. Sisodia, "Noise Reduction in Crossed-Field Guns by Cathode Tilt," Letter in Proc. IEEE, Jan 1968

15. J.E. Boers, Computer Simulation of Space Charge Flows, Technical Report No. RADC-TR-68-175, Rome Air Development Center, Griffiss Air Force Base, New York, April 1968 (AD 832 590)

16. J.F. Hull and G.P. Kooyers, "Experimental and Theoretical Characteristics of Injected Beam Type Crossed-Field Amplifiers," Proc International Conference on Microwave Tubes 1969 - Microwellenrohren, Friedr, Vieweg & Sohn, Brunschweig

DISTRIBUTION LIST

Contract NAS3-11528	Copy Number
National Aeronautics & Space Administration	
Headquarters	
Washington, D.C. 20546	
Attention: SA/L. Jaffe	1
SCC/A.M.G. Andrus	10
SC/R.B. Marsten	1
NASA-Lewis Research Center	
21000 Brookpark Road	
Cleveland, Ohio 44135	
Attention: C.C. Conger (MS 54-1)	1
R.E. Alexovich (MS 54-5)	1
Dr. H.G. Kosmahl (MS 54-5)	1
Technology Utilization Officer (MS 3-19)	1
Rockets & Spacecraft Procurement Section (MS 500-313)	1
Library (MS 60-3)	2
Report Control Office (MS 5-5)	1
N.T. Musial (MS 500-311)	1
G.J. Chomos (MS-54-5)	50
Communication Systems Inc.	
5817 Columbia Pike	
Falls Church, Virginia 22046	
Attention: J. Bisaga	1
Rand Corporation	
1700 Main Street	
Santa Monica, California 90404	
Attention: Dr. J. Holt	1
NASA-George C. Marshall Space Flight Center	
Huntsville, Alabama 35812	
Attention: RASTR-A/E.C. Hamilton	1
Library	1
NASA-Goddard Space Flight Center	
Greenbelt, Maryland 20771	
Attention: 733/R. Pickard	1
Library	1

Contract NAS3-11528

NASA-Ames Research Center
Moffett Field, California 94035

Attention:	OART-MAO/E. Van Vleck (MS 202-6)	1
	Library	1

NASA-Langley Research Center
Langley Station
Hampton, Virginia 23365

Attention:	B. Kendall (MS-173)	1
	Library (MS-185)	1

NASA-Manned Spacecraft Center
Houston, Texas 77001

Attention:	Library	1

Jet Propulsion Laboratory
4800 Oak Grove Drive
Pasadena, California 91103

Attention:	L. Derr	1
	Library	1

NASA Scientific and Technical Information Facility
P.O. Box 33
College Park, Maryland 20740

Attention:	NASA Representative	3

TRW Systems
One Space Park
Redondo Beach, California 90278

Attention:	W.A. Finley/Space Vehicle Division	1

General Dynamics, Convair Division
P.O. Box 1128
San Diego, California 92112

Attention:	F.J. Dore/Advanced Programs Laboratory	1

Hughes Aircraft Co.
Space Systems Division
1194 W. Jefferson Boulevard
Calver City, California 90230

Attention:	H.A. Rosen/Satellite Systems Laboratory	1

Contract NAS3-11528
General Electric Co.
Missile and Space Division
Valley Forge Space Technology Center
P.O. Box 8555
Philadelphia, Pennsylvania 19101
Attention: H. Collins 1
P. Nadler 1

Federal Communications Commission
521 12th Street
Washington, D.C. 20554
Attention: H. Fine 1

U. S. Information Agency
25M St. S.W.
Washington, D.S. 20547
Attention: IBS/EF/G. Jacobs 1

General Electric Co.
Tube Department
Microwave Tube Operation
Schenectady, New York
Attention: R. Dehn 1
Dr. T. Mihran 1
Dr. C. Branch 1
W. Neugebauer 1

Litton Industries
Electron Tube Division
960 Industrial Road
San Carlos, California 94070
Attention: Dr. G. Pokorney 1
J. Orr 1
W. Day 1
Dr. O. Sauseng 1

Varian
Eastern Tube Division
Salem Road
Beverly, Massachusetts 01915
Attention: Dr. G. Farney 1

Contract NAS3-11528
Hughes Aircraft Company
Electron Dynamics Division
P.O. Box 2999
Torrance, California 90509
Attention: Dr. J. Mendel 1
Dr. I Tammaru 1

Watkins Johnson Company
333 Hillview Avenue
Palo Alto, California 94304
Attention: Dr. D. Watkins 1

Varian Associates
611 Hansen Way
Palo Alto, California 94303
Attention: Dr. G. Caryotakis 1
Dr. J. Reutz 1

R.C.A.
Industrial Tube Division
Lancaster, Pennsylvania
Attention: W.P. Bennett 1

Raytheon Company
Research Division
28 Seyon Street
Waltham, Massachusetts
Attention: W. Teich 1
Dr. J.M. Osepchuk 1

Mr. Lawrence Gasch 1
Aerospace Radar Branch
U.S. NRL
Washington, D.C. 20390

Mr. Robert Richardson 1
Mail No. 1620
Martin-Marietta Corp.
Denver Division
P.O. Box 179
Denver, Colorado 90201

Contract NAS3-11528
Mr. William E. Waters 1
Sr. Engr Staff Specialist
3939 Fabian Way
M.S. C-70
Palo Alto, California 94303

Mr. George Orr 1
Code 733
Goddard Space Flight Center
Greenbelt, Maryland 20771

Sperry
Electronic Tube Division
Gainsville, Florida 32601
Attention: H.H. Conners 1

Lt. Commander L. Wardel 1
Naval Electronic Systems Command
PME 116
Washington, D. C. 20360

Commanding Officer
Navy Space Systems Activity
Air Force Unit Post Office
Los Angeles, California 90045
Attention: Code 50 1

U.S. Air Force Liason Officer (MS 501-3) 1
c/o NASA-Lewis Research Center
21000 Brookpark Road
Cleveland, Ohio 44135